Investigation of Advanced Dose Verification Techniques for External Beam Radiation Treatment

by

Ganiyu Adeniyi Asuni

A Thesis submitted to the Faculty of Graduate Studies of

The University of Manitoba

In Partial Fulfillment of the Requirements

For the Degree of

DOCTOR OF PHILOSOPHY

Department of Physics and Astronomy

University of Manitoba

Winnipeg, Manitoba, Canada

© Ganiyu A. Asuni 2013

Abstract

Intensity modulated radiation therapy (IMRT) and volumetric modulated arc therapy (VMAT) have been introduced in radiation therapy to achieve highly conformal dose distributions around the tumour while minimizing dose to surrounding normal tissues. These techniques have increased the need for comprehensive quality assurance tests, to verify that customized patient treatment plans are accurately delivered during treatment. *In vivo* dose verification, performed during treatment delivery, confirms that the actual dose delivered is the same as the prescribed dose, helping to reduce treatment delivery errors. *In vivo* measurements may be accomplished using entrance or exit detectors. The objective of this project is to investigate a novel entrance detector designed for *in vivo* dose verification.

This thesis is separated into three main investigations, focusing on a prototype entrance transmission detector (TRD) developed by IBA Dosimetry, Germany. First contaminant electrons generated by the TRD in a 6 MV photon beam were investigated using Monte Carlo (MC) simulation. This study demonstrates that modification of the contaminant electron model in the treatment planning system is required for accurate patient dose calculation in buildup regions when using the device. Second, the ability of the TRD to accurately measure dose from IMRT and VMAT was investigated by characterising the spatial resolution of the device. This was accomplished by measuring the point spread function with further validation provided by MC simulation. Comparisons of measured and calculated doses show that the spatial resolution of the TRD allows for measurement of clinical IMRT fields within acceptable tolerance. Finally, a new general research tool

was developed to perform MC simulations for VMAT and IMRT treatments, simultaneously tracking dose deposition in both the patient CT geometry and an arbitrary planar detector system, generalized to handle either entrance or exit orientations. It was demonstrated that the tool accurately simulates dose to the patient CT and planar detector geometries. The tool has been made freely available to the medical physics research community to help advance the development of *in vivo* planar detectors.

In conclusion, this thesis presents several investigations that improve the understanding of a novel entrance detector designed for patient *in vivo* dosimetry.

Acknowledgements

I would like to use this opportunity to express my sincere gratitude to a number of people who have supported me and contributed to this project in many unique ways.

I would like to thank my supervisor and mentor, Dr. Boyd McCurdy for taking me on as a student and for his generous support as well as his never-ending patience during my years of graduate studies at the University of Manitoba. From the beginning of my journey, he provided me with the research skills required for good scientific reasoning and skills for communicating scientific results effectively. It was a great pleasure working with him and I look forward to our continued collaboration in future where I hope to continue to benefit from his clinical skills.

I would like to thank members of my thesis committee: Dr. Jeff Bews, Dr. Sankar Venkataraman, Dr. Michael Gericke, and Dr. Gabriel Thomas for their advice throughout my Ph.D. Special thanks go to Dr. Jeff Bews for his mentoring during the program and for his valuable advice in the development of my project. I would also like to thank my external examiner Dr. Andrew Jirasek from University of Victoria, British Colombia for his contributions and suggestions on improving this thesis.

I am very grateful to Dr. Stephen Pistorius, the academic director of the Medical Physics graduate program at University of Manitoba and CancerCare Manitoba, for his valuable advice and suggestions on improving my research work.

I would like to thank the following people for their invaluable assistance during manuscript preparation, Dr. Daniel Rickey, Martin Jensen, Dr. Sankar Venkenteraman, Timothy van Beek, and Dr. Antoniu Popescu of British Colombia Cancer Agency, Vancouver Centre.

I would also like to thank current and past students as well as staffs at CancerCare Manitoba for their friendship and support – Tamar Chighvinadze, Troy Teo, Heather Champion, Peter McCowan, Jenna King, Mike Hebb, Bryan McIntosh, Hongyan Sun, Huanjin Wu, Dr. Fazal Ur-rehman, Dr. Peter Potrebko, Dr. Niranjan Venugopal, Dr. Krista Chytyk, Dr. Jorge Alpuche, Dr. Eric Van Uytven, Dr. Ryan Rivest, Dr. Anita Berndt, Dr. John Lewis, Dr. Harry Ingleby, Dr. Idris Elbakri, and Dr. Daniel Flores-Tapia.

I would like to gratefully acknowledge financial support for this project provided by the University of Manitoba, CancerCare Manitoba, and Manitoba Health Research Council.

I am truly indebted to my wonderful mother Al-Hajja Khadijat Asuni, my loving father Al-Hajj Tajudeen Asuni, my brothers and sisters as well as their family members too numerous to be mentioned here for their constant support, encouragement, and continuous prayers. Also, I am very grateful to my in-laws Mrs. Rashidat Alimi and late Al-Hajj Abdul-Rasheed Alimi as well as their children for their understanding and support.

Finally, I would like to express my sincere appreciation to my wife Taibat for her incredible support and never ending patience throughout this long journey. It is difficult for me to describe the sacrifices she has made for me (and the kids) in our decade-old relationship, so for these and other reasons I will forever be thankful to her. The boys – Abdullah, Abdul-Aziz, and Anees have been great gifts from Allaah and their presence in our lives has been source of joy to us as well as strengthened our relationship. I cannot wait to see them grow up and continue to put smiles on our faces as they do now.

Dedication

To my parents, my wife and my children

Table of Contents

Title Page ii

Abstract ii
Acknowledgements iv
Dedication vi
Table of Contents vii
List of Tables x
List of Figures and Illustrations xii
List of Abbreviations xvii
List of Abbreviations xvii

CHAPTER ONE: RATIONALE AND OBJECTIVE 1
1.1 Biological Effect of Radiation Therapy 1
1.2 Accuracy Required in Dose Delivery 4
1.3 Dose Verification Processes in Radiation Therapy 6
1.4 Thesis Overview 8
1.4.1 Summary of Chapter Three: A Monte Carlo investigation of the contaminant electrons due to a novel in vivo transmission detector 10
1.4.2 Summary of Chapter Four: Investigation of the spatial resolution of an online dose verification device 11
1.4.3 Summary of Chapter Five: A Monte Carlo tool for evaluating VMAT and DIMRT treatment delivery including planar detectors 13
1.5 Bibliography 15

CHAPTER TWO: INTRODUCTION 17
2.1 Radiation Therapy for Cancer Patients 17
2.2 Methods of Dose Verification in Radiation Therapy 22
2.3 Dosimetry Systems for Dose Verification 25
2.3.1 Zero -Dimensional (Point) Detectors 26
2.3.2 Two Dimensional (Planar) Detectors 27
2.4 Physics of Ionization Chambers 31
2.5 The COMPASS System 34
2.6 Electronic Portal Imaging Devices 40
2.7 Sampling Theory and Application to Radiation Therapy Detectors 43
2.7.1 Sampling frequency and Nyquist frequency 43
2.7.2 Spatial Resolution and Application to Radiation Therapy Detectors 47
2.8 Use of Monte Carlo Technique in Radiation Therapy 55
2.8.1 The EGSnrc Monte Carlo System 56
2.8.1.1 Simulation of particle transport in EGSnrc Monte Carlo code 61
2.8.1.2 Accuracy of EGSnrc Monte Carlo code 62
2.8.1.3 BEAMnrc user code 64
2.8.1.4 DOSXYZnrc user code 65
2.9 Monte Carlo Dose Calculation Methods for Complex Treatment Delivery Techniques 66
2.10 Dosimetric Evaluation of Measured and Calculated Dose Distributions 69

2.11 Bibliography 76

CHAPTER THREE: A MONTE CARLO INVESTIGATION OF CONTAMINANT ELECTRONS DUE TO A NOVEL *IN VIVO* TRANSMISSION DETECTOR 87
3.1 Introduction 87
3.2 Materials and methods 92
3.2.1 Monte Carlo simulations of beam characteristics 92
3.2.2 Calculations and Measurements of Surface Dose 94
3.2.3 Effect of the TRD on TPS modeling of electron contamination 96
3.3 Results and Discussion 99
3.3.1 Validation of the Monte Carlo model 99
3.3.2 Beam characteristics from phase-space analysis 99
3.3.2.1 Electron fluence 99
3.3.2.2 Energy spectra, mean energy, and angular distribution 102
3.3.2.3 Sources of scored particles 107
3.3.3 Comparison of Calculated and Measured surface Dose 110
3.3.4 Electron contamination model parameters with and without TRD 113
3.4 Conclusions 116
3.5 Bibliography 118

CHAPTER FOUR: INVESTIGATION OF THE SPATIAL RESOLUTION OF AN ONLINE DOSE VERIFICATION DEVICE 121
4.1 INTRODUCTION 121
4.2 MATERIALS AND METHODS 124
4.2.1 Experimental setup for LSF Measurement 124
4.2.2 Monte Carlo simulation and calculation of LSF 128
4.2.2.1 Calculation of the film response function 128
4.2.2.2 Calculation of the TRD line spread function 130
4.2.2.3 Calculation of the LSF for an ideal circular detector 131
4.2.3 Validation of the measured LSF and detector response function 131
4.3 Results and Discussion 135
4.3.1 Measured and calculated response function 135
4.3.2 Effect of the detector response function 140
4.4 Conclusions 145
4.5 Bibliography 146

CHAPTER FIVE: A MONTE CARLO TOOL FOR EVALUATING VMAT AND DIMRT TREATMENT DELIVERIES INCLUDING PLANAR DETECTORS 150
5.1 Introduction 150
5.2 Materials and Methods 153
5.2.1 Monte Carlo simulation tool for VMAT 153
5.2.1.1 BEAMnrc simulation of the linac head 154
5.2.1.2 Dose calculation of VMAT delivery for each control point 155
5.2.2 Validation of the VMAT Monte Carlo tool with an entrance and an exit detector 160
5.2.2.1 EPID and portal image acquisition of VMAT delivery 161
5.2.2.2 Entrance fluence measurement of DIMRT delivery 162

5.2.3 Evaluation of simulated 2D planar doses and simulated 3D doses 163
5.3 Results 165
5.3.1 Validation of phantom or patient dose 165
5.3.2 Validation of planar dose 168
5.4 Discussion and Conclusions 173
5.5 Bibliography 178

CHAPTER SIX: SUMMARY 183
6.1 Conclusions 183
6.2 Future work 189
6.3 Bibliography 191

APPENDIX A: THE INFLUENCE OF A NOVEL TRANSMISSION DETECTOR ON 6 MV X-RAY BEAM CHARACTERISTICS 193
A.1. Introduction 193
A.2. Methods and materials 194
Description of a COMPASS detector 194
A.2.1. Measurement techniques 195
A.2.2. The influence of the transmission detector on the surface dose and in the build-up region 198
A.2.3. The influence of the transmission detector on dose beyond dmax 199
A.2.4. Comparison of the transmission detector to a block tray 200
A.3. Results 200
A.3.1. The influence of the transmission detector on the surface dose and dose within the buildup region 200
A.3.2. The influence of the transmission detector on dose beyond dmax 203
A.3.3. Comparison of the transmission detector to a block tray 205
A.4. Discussions 206
A.5. Conclusions 208
A.6. Bibliography 209

APPENDIX B: INSTRUCTIONS ON HOW TO USE THE MONTE CARLO RESEARCH TOOL FOR EVALUATING VMAT TREATMENT DELIVERY INCLUDING PLANAR DETECTORS 212
B.1. Pre-simulation stage 213
B.2. Simulation stage 214
B.3. Post Simulation stage 215

APPENDIX C: GLOSSARY OF TERMS‡ 216

List of Tables

Table 2-1: Multi-leaf collimator (MLC) component modules developed in BEAMnrc .. 68

Table 3-1. Mean energy of contaminant electrons for open and non-open 10x10 cm^2 fields scored at 70 cm and 100 cm SSD in the 30 x 30 cm^2 phase-space file..... 104

Table 3-2: Contaminant electrons scored in the phase-space at 70 cm SSD from different component modules in the linear accelerator model. Raw particle counts are shown, with the percentage of total fluence given in parentheses..... 108

Table 3-3: Contaminant electrons scored in the phase-space at 100 cm SSD from different component modules in the linear accelerator model. Raw particle counts are shown, with the percentage of total fluence given in parentheses..... 109

Table 3-4: Calculated and measured percentage surface dose relative to maximum dose in a 10 x 10 cm^2 field for open and non-open fields..... 111

Table 3-5: Contaminant electron surface dose (ESD) relative to maximum dose and additional electron contamination contribution to dose at the surface (compared to open field) in a 10 x 10 cm^2 field for both TRD and block tray. 112

Table 3-6: The optimized electron contamination parameters (i.e. average for 5 x 5, 10 x 10, and 20 x 20 cm^2 field sizes) for the Eclipse AAA dose algorithm (equation 3.1): Gaussian widths s1 and s2 and c the relative weight of the first Gaussian for open and TRD fields. 114

Table 3-7: The depth dose and off-axis effect electron contamination parameters in Pinnacle[3] dose calculation algorithm (equation 3.2 and 3.3): the scale fraction (SF), depth coefficient (K), off-axis coefficient (OAC) and for open and TRD fields. 116

Table 3-8: The relative output effect (i.e. average for 5 x 5, 10 x 10, and 20 x 20 cm^2 field sizes) in Pinnacle[3] dose calculation algorithm (equation 3.4) for open and TRD field 116

Table 5-1: Percentage of voxels with $\gamma<1$ ($PP_{\gamma<1}$) and average gamma (γ_{AVG}) using 3% DD and 3 mm DTA for the verification plans. 168

Table 5-2: Range of percentage of pixels ($PP_{\gamma<1}$) with $\gamma<1$, range of average gamma (γ_{AVG}) and range of maximum gamma (γ_{MAX}) using 3% DD and 3 mm DTA for all the control points in both the clockwise (CW) and counterclockwise (CCW) arcs. Number of control point images with less than 90% of voxels with $\gamma<1$ (last column) 170

Table A-1: The difference between the surface doses in open and COMPASS field. Differences are expressed as a percentage of the dose at 1.4 cm depth, i.e. *S* (COMPASS field) − *S* (open field). The measured surface doses in the open

fields (percentage of the dose at 1.4 cm depth) are shown in parentheses for reference..... 201

List of Figures and Illustrations

Figure 1-1: A medical linear accelerator used for production of high energy photon beams for treatment of cancer 2

Figure 1-3: Example of a dose response curve for tumour control probability (TCP) and normal tissue complication probability (NTCP). An acceptable treatment is designed to have the curves far from each other. 5

Figure 2-1: Description of the different components in a medical linear accelerator. 18

Figure 2-2 A multi-leaf collimator (MLC) used to create simple and complex fields. 19

Figure 2-3: Two different approaches for using portal imaging for *in vivo* dosimetry. In the forward approach, predicted and measured transmission doses are compared while in the backward approach, predicted and reconstructed patient dose from measured transmission dose are compared. 31

Figure 2-4: (a) A Farmer-type ionization chamber (b) Plane-parallel ionization chamber 34

Figure 2-5: (a) Photo of the transmission detector (not inserted into the treatment unit) and (b) cross section of transmission detector modeled as three layers. 35

Figure 2-6: A schematic of dose reconstruction method in the COMPASS system. The RT plan from the TPS is exported to the software. Measurement of the plan with the TRD (R_{meas}) is used to reconstruct the fluence and to reconstruct the dose in the patient/phantom CT (D_{RC}). 38

Figure 2-7: (a) Varian aS500/aS1000 imager design. (b) Pixel details including example interactions. 42

Figure 2-8: Example of aliasing (a) 20 kHz sinusoidal signal to be sampled by a digital system (b) sampling at 7.5 kHz frequency (c) sampling at 40 kHz (Nyquist) frequency (d) sampling of signal with no aliasing at 90 kHz frequency. . 46

Figure 2-9: Example of effect of finite spacing between detectors on sampled signal. Large sampling distance will result in overlap of high and low frequency contents of sampled signal. 47

Figure 2-10: The image of a point source by non-ideal systems produces an un-sharp image. 49

Figure 2-11: The line spread function (LSF) is the image of a line source. 51

Figure 2-12: The modulation transfer function (MTF) is the modulus of the Fourier

transform of the LSF. It is used to characterize the spatial resolution of an imaging system. 53

Figure 2-13: Illustration of the Linac head simulation in BEAMnrc and dose calculation in DOXYZnrc. 58

Figure 2-14: Example of gamma test for a 10 x 10 cm^2 field showing (a) reference distribution (b) modified evaluated distribution (c) dose difference analysis shows differences in dose between both distributions (d) distance to agreement analysis shows differences in DTA between the quadrants of both distributions (e) composite distribution shows regions that passed either or both the DD or DTA (f) gamma distribution for 3% and 3 mm criteria. 71

Figure 2-15: Acceptance tube defining the dose gradient of the reference dataset around the reference points for comparison of both dose distributions. 75

Figure 3-1 (a) TRD mounted on the gantry of the linear accelerator. (b) The TRD modeled as a three layer device in a BEAMnrc simulation 91

Figure 3-2: Planar fluence profiles of contaminant electrons for open and non-open 10x10 cm^2 fields scored in the phase-space at (a) 70 cm SSD and (b) 100 cm SSD 100

Figure 3-3: Planar fluence profiles of contaminant electrons scored in the phase-space at 100 cm SSD for different field sizes in open and non - open fields: TRD (●) and Tray (—). 102

Figure 3-4: Energy spectra of contaminant electrons for open and non-open 10x10 cm^2 fields scored in the phase-space at (a) 70 cm SSD and (b) 100 cm SSD. The absolute counts/MeV/incident electrons are normalized to the maximum value for the 10 x10 cm^2 open field at 100 cm SSD. 104

Figure 3-5: Angular distributions of contaminant electrons for open and non-open 10x10 cm2 fields scored in the phase-space at (a) 70 cm SSD and (b) 100 cm SSD. The absolute counts/per degree are normalized to the maximum value for the open field scored at 100 cm SSD. 106

Figure 3-6: The angular distribution of open and non-open fields for field sizes (a) 5 x 5 cm^2 and (b) 20 x 20 cm^2, at 100 cm SSD. The absolute counts/per degree are normalized to the maximum value for the open field. 107

Figure 3-7: Extra contribution of contaminant electrons to surface dose for different field sizes for TRD and block tray. The extra contaminant electron dose is the difference between the calculated ePDDs for non-open fields and open fields, as described in section 3.2.2. 113

Figure 4-1: The experimental set up used for measuring the LSF of the transmission detector. The slit collimator with an opening of 0.25 x 10 x 152 mm^3 was

suspended underneath the couch and held stationary above the TRD. The three threaded rods allowed adjustment of the slit collimator angle. 125

Figure 4-2: Schematic representation of the linear accelerator head geometry used for simulating the detector response function in BEAMnrc. Phase space files were obtained at two different scoring regions, i.e., the entrance and exit surfaces of the slit collimator at 175.8 and 191.0 cm SSD, respectively. 129

Figure 4-3: An overview of the method of comparing measured and calculated dose distributions of the IMRT fields. The calculated dose is a convolution of the Monte Carlo generated incident fluence and the measured 2D detector response . 135

Figure 4-4: The width of the collimated photon beam as measured by Gafchromic EBT2 film and predicted by MC simulation..... 136

Figure 4-5: The LSF for three adjacent chambers in the transmission detector. The chambers are in row 21 of the TRD. 138

Figure 4-6: The LSFs of two adjacent chambers in the transmission detector are overlaid. 139

Figure 4-7: Plot showing the measured LSF of one chamber of the TRD, the MC calculated response function, and the ideal response of a cylindrical detector of 3.8 mm diameter. 139

Figure 4-8: The measured, MC calculated and ideal pre-sampling modulation transfer functions (MTF) for a single chamber in the transmission detector. 140

Figure 4-9: The detector response function (DRF) normalized to unit area of a single chamber in the transmission detector. The LSF is shown for reference. 141

Figure 4-10: The in–plane (left) and cross–plane (right) profiles through the central axis of the measured and directly calculated dose in DOSXYZnrc for IMRT field 1..... 142

Figure 4-11: Image (left) showing a χ -comparison result between the measured and calculated dose distributions. A histogram plot (right) of in-field χ -comparison result for IMRT field 1..... 143

Figure 4-12: Measured (M) and calculated (C) dose for a head and neck, sliding window, IMRT field 1 with 119 control points (top panels). The histogram plot of in-field χ- comparison result (bottom left panel) and the horizontal profiles of measured and calculated dose (bottom right panel). 144

Figure 5-1: An overview of the MC simulation tool for calculating dose simultaneously in the patient/phantom geometry and the planar detector geometry, for individual control points of a VMAT delivery..... 154

Figure 5-2: Illustration of the process to obtain MC phantom files. In panel A, we have the phantom only, then the planar detector model is added in panel B (an EPID for illustration) and panel C demonstrates how we rotate the phantom only (and in the opposite direction to the TPS indicated gantry rotation) in order to orient it correctly to the linac and planar detector geometry. Note the EPID layer thicknesses are not drawn to scale. 158

Figure 5-3: Monte Carlo setup used for verification of individual control points of a VMAT delivery measured by EPID. Simulations of MLC leaf positions for individual control points were performed using *particleDMLC* code complied as a shared library in DOSXYZnrc. Lower (X) jaws are not shown here..... 159

Figure 5-4: Monte Carlo calculated absolute dose for a VMAT prostate plan illustrated in transverse (top panel), sagittal (middle panel), and coronal (bottom panel) planes. Their respective Gamma maps (i.e. quantitative evaluation between MC and TPS dose distributions) and dose profiles are also shown here.. 167

Figure 5-5: Monte Carlo calculated EPID dose (left panel) and measured EPID dose (right panel) for three randomly selected different control points 68, 93, and 28 in the VMAT prostate plan. 171

Figure 5-6: Histogram of $PP_{\gamma<1}$ and γ_{AVG} as a function of control points for arc 1 – VMAT prostate plan (top row), arc 1 - VMAT head-and-neck (middle row), and beam 1 DIMRT head-and-neck (bottom row). 172

Figure 5-7: Monte Carlo calculated and measured EPID doses for one of the control points in the VMAT prostate plan showing the banding artifact in measured data.173

Figure A-1: (a) COMPASS detector (b) COMPASS mounted on the gantry of a linear accelerator 194

Figure A-2: Comparison of the dose in the buildup region measured in solid water with a Markus chamber and EBT film, and the calculated dose from Monte Carlo simulation for an open field of 10 × 10 cm^2 and an SSD of 90 cm..... 201

Figure A-3: The dose in the buildup region at SSDs of (a) 90 cm, (b) 80 cm and (c) 70 cm. The lines indicate measured doses in the open field, whereas the symbols represent doses measured with the transmission detector in the beam. All the measurements were performed with the Markus chamber in solid water..... 203

Figure A-4: The surface dose profile at SSDs of (a) 70 cm and (b) 90 cm for 20 × 20 cm^2 field size. The lines indicate measured doses in the open field, whereas the symbols represent doses measured with the transmission detector in the beam. Measurements were taken with the Markus chamber in solid water; (c) shows the difference between the surface dose profile with and without the transmission detector in the beam expressed as a percentage of the open field dose on the central axis. Data for the three SSDs show the reduction in surface dose in-field

and increase in surface dose out-of-field as the SSD increases, due to the lateral divergence of the electrons produced in the transmission detector 204

Figure A-5: PDDs beyond d_{max} for 5 × 5cm^2 (lower curve) and 20 × 20 cm^2 fields at an SSD of 80 cm. The first measurement point is at d_{max} in the figure. Measurements were taken with the Markus chamber in the water phantom. Similar results were obtained at 70 cm and 90 cm SSDs..... 206

Figure A-6: Profiles at 1.4 cm and 10 cm depths for 5 × 5cm^2 and 20 × 20 cm^2 fields at an SSD of 90 cm. Measurements were taken with the diode in the water phantom..... 206

List of Abbreviations

3D-CRT	**Three Dimensional Conformal Radiation Therapy**
CF	**Calibration Factor**
CHT	**Condensed History Technique**
CP	**Control Point**
CT	**Computed Tomography**
DD	**Dose Difference**
DICOM	**Digital Imaging and Communications in Medicine**
DMLC	**Dynamic Multi-leaf Collimator**
DNA	**Deoxyribonucleic Acid**
DRF	**Detector Response Function**
DTA	**Distance-to-Agreement**
DVH	**Dose Volume Histogram**
ECUT	**Electron Energy Cutoff**
EPID	**Electronic portal Imaging Device**
FWHM	**Full Width Half Maximum**
IMRT	**Intensity Modulated Radiation Therapy**
LINAC	**Linear Accelerator**
LSF	**Line Spread Function**
MC	**Monte Carlo**
MLC	**Multi-leaf Collimator**
MTF	**Modulation Transfer Function**

MU	**Monitor Unit**
NTCP	**Normal Tissue Complication Probability**
OAR	**Organ at Risk**
OTF	**Optical Transfer Function**
PCUT	**Photon Energy Cutoff**
PDD	**Percentage Depth Dose**
PSF	**Point Spread Function**
PTV	**Planning Target Volume**
QA	**Quality Assurance**
SDD	**Source-to-Detector Distance**
SSD	**Source-to-Surface Distance**
TCP	**Tumour Control Probability**
TERMA	**Total Energy Released Per Unit Mass**
TPS	**Treatment Planning System**
TRAY	**Plastic Block Tray**
TRD	**Transmission Detector**
VMAT	**Volumetric Modulated Arc Therapy**

CHAPTER ONE: RATIONALE AND OBJECTIVE

1.1 Biological Effect of Radiation Therapy

Cancer is a common term for collection of different diseases that involves malignant tumour or growth caused when cells divide or multiply without control destroying healthy tissues. The World Health Organization (W.H.O) statistics show that cancer, the leading cause of deaths worldwide, accounted for 7.6 million deaths in 2008 and predicted about 60% increase by 2030 [1]. Radiation therapy is one of the modalities used in the treatment of cancer patients. The other main modalities are surgery and chemotherapy, and a combination of these modalities to achieve positive treatment outcomes is very common. Radiation therapy is used to eradicate or reduce tumours in patients and may be delivered to tumour sites from an external ionizing radiation source using high energy photon beams generated by medical linear accelerators (Figure 1.1). This is referred to as external beam radiation therapy. Alternatively, treatments can be delivered by bringing radioactive materials into close proximity to the disease, a method referred to as brachytherapy. Ionizing radiation damages both cancerous cells and healthy cells. The common outcomes of irradiation of the human cell include chromosome breakage, apoptosis (programmed cell death), reproductive failure, cell mutation, cell transformation as well as adaptive responses and acute radiation sickness [2]. The biological effects of ionizing radiation primarily result from damage to deoxyribonucleic acid (DNA), the most critical target in the nucleus of a cell [3]. Damage to DNA may be classified as occurring through either direct or indirect action [2]. The direct action occurs

when radiation interacts directly with the DNA molecule. In this process, ionization or excitation of the atoms of the target may occur, causing a break in one or both strands of the molecule, which if unrepaired or incorrectly repaired, will cause the cell to lose its ability to reproduce via mitosis. For indirect action, radiation interacts in the surrounding medium (i.e. water) as opposed to the DNA molecule and results in the production of 'free radicals'. The ionization of water molecules produces a very important and extremely reactive free radical, hydroxyl (OH^-) and a water ion (H_2O^+). When encountering a broken DNA strand, a free radical will bind to the end of the broken strand, thereby interfering with the natural repair mechanisms. This effectively 'sets' the damage to the DNA and this type of action also plays a significant role in preventing the cell from reproducing.



Figure 1-1: A medical linear accelerator used for production of high energy photon beams for treatment of cancer

The damage due to irradiation of cells is classified into lethal damage, sublethal damage and potentially lethal damage. Lethal damage is irreversible and irreparable and will ultimately lead to cell death. This type of damage is expected for cancerous cells in order to produce a positive treatment outcome. In sublethal damage, the cells can be repaired in hours if additional sublethal damage is not added. In potentially lethal damage, the cells can be repaired under certain post-irradiation environmental conditions and at specific cell cycle arrest [3]. In radiation therapy, treatments are typically delivered once daily for up to eight weeks using multiple small dose fractions (i.e. fractionation) allowing for the repair of sublethal damage between fractions and cellular repopulation of normal tissues while cancer cells are less likely to repair. In addition, fractionation increases damage to the tumor due to reoxygenation and reassortment of cells into radiosensitive phases of cell cycle between dose fractions.

Due to the possibility of damage to normal tissues, the use of external beam radiation therapy should involve careful and precise planning to achieve the goal of maximizing dose to the target volumes (cancerous cells) while minimizing the dose to normal tissue structures and organs at risk (OAR). Advanced radiation therapy treatment techniques (additional explanations are provided in chapter 2) such as Intensity Modulated Radiation Therapy (IMRT) and Volumetric Modulated Arc Therapy (VMAT) have been developed to reach this goal by delivering highly conformal dose to the tumour with rapid dose fall off around critical tissue structures [4, 5]. Due to the complexities of these techniques they have increased the need for comprehensive quality assurance tests, ensuring that the customized patient treatment plan is accurately delivered during

treatment [6, 7].

1.2 Accuracy Required in Dose Delivery

The required accuracy in absolute dose delivery strongly depends on two important dose relationships: 1) the relationship between dose and tumour control and 2) the relationship between dose and normal tissue complications. These relationships are illustrated in the dose response curves for tumour control probability (TCP) and normal tissue complication probability (NTCP). TCP is the probability of controlling tumor growth after radiation dose while NTCP is the probability of normal tissue complications after radiation dose. As shown in Figure 1-2, increasing the dose delivered to the tumour increases the probability to control the tumour at the cost of increased normal tissue complications. This is a major concern in patient treatment because it could lead to detrimental effects in normal tissues and organs (potentially causing serious functional issues or even patient death) and introduce radiation-induced secondary cancer in patients after treatments as reported in the literature [8-10]. The steepness of the dose response curves indicates that a 5% variation in the delivered dose can make a noticeable difference in the patient treatment outcome [11, 12]. Brahme (1984) has shown that for a typical tumour control probability, an underdosage of the tumour by 5% will reduce the control of the tumour by 15% and an increase in 5% dose to surrounding healthy tissue of certain organs at risk (OAR) may lead to intolerable side effects [11]. The goal of radiation treatment is to maximize control of the tumour while at the same time reducing normal tissue complications to an acceptable level. This requires that the TCP and NTCP

response curves be pushed as far apart as possible.

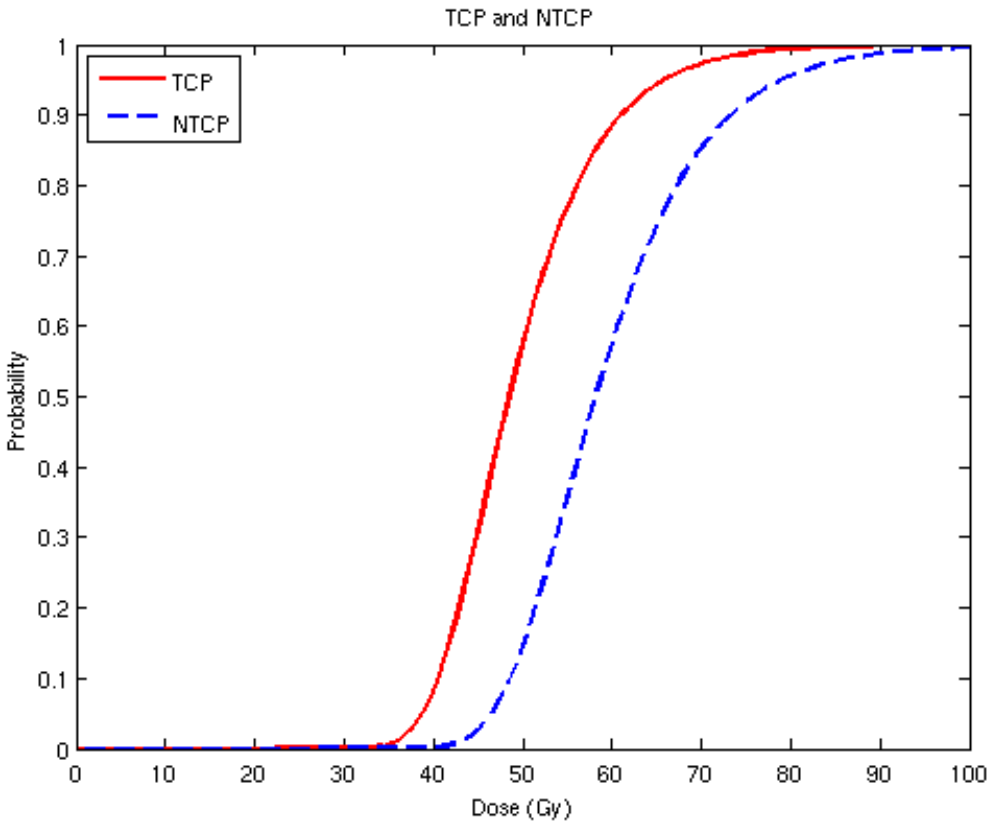


Figure 1-3: Example of a dose response curve for tumour control probability (TCP) and normal tissue complication probability (NTCP). An acceptable treatment is designed to have the curves far from each other.

Based on the steepness of the dose-response curves from limited routine clinical data available, the International Commission on Radiation Units and Measurements (ICRU) in 1976 recommended that ± 5% accuracy is required in the delivery of absorbed dose to the target volume and may require ± 2% accuracy in critical conditions [12] such

as stereotactic radiosurgery. Other researchers recommend a dose delivery accuracy of 3.5% and 3% to achieve suitable patient outcome [13, 14]. Furthermore, it has been shown that for reasonable tumour control to be achieved without severe tissue complications, dosimetric uncertainties during delivery need to be very small [15]. To reduce dosimetric uncertainties during delivery, the comprehensive verification of the treatment plan and quality assurance procedures of delivery techniques are required, before the treatment is delivered to the patient. These processes will help reduce uncertainties and ultimately improve the quality of treatment delivered to patients.

1.3 Dose Verification Processes in Radiation Therapy

While complex treatment techniques such as IMRT and VMAT allow highly conformal dose distributions to be delivered to the tumour with reduced dose to surrounding normal tissue structures, they also introduced great challenges in ensuring that the delivered dose distributions correspond closely to those planned (i.e. within acceptable tolerances). Patient-specific dose verification is commonly performed before patient treatment *without the patient present* (known as 'pre-treatment verification') to verify the ability of the treatment planning system (TPS) to calculate dose accurately, to detect data transfer errors from TPS to treatment machine, and the ability of the machine to deliver dose accurately. It may only detect machine-dependent errors at the time of verification and is not capable of detecting errors arising after the pre-treatment QA (i.e. during the delivery of the treatment course to the patient). Nevertheless, this process is crucial because these treatment techniques involve the movement of different beam

collimating devices (i.e. multi-leaf collimator or secondary jaws), the gantry (head of the linear accelerator), the treatment couch, and the real-time modulation of dose-rate. Machine related errors such as incorrect multi-leaf collimator (MLC) leaf positions, incorrect monitor units, or incorrect flatness/symmetry may occur during treatment delivery of IMRT and VMAT. To ensure that the customized treatment plan is accurately delivered, patient-specific dose verification is generally recommended [5] and performed in most cancer centres.

Typical patient-specific dose verification is achieved by calculating the dose to the computed tomography (CT) data set of a phantom [7] if the patient's treatment were applied to that phantom, and then confirming the dose delivered to the phantom via a measurement. The measurement usually includes a point dose check performed using an ionization chamber placed in the phantom. A point dose check allows for a validation of absolute dose of the treatment plan at a single point. In addition to this, commonly one or several sheets of radiographic or radiochromic film are inserted in the phantom in a plane orthogonal or parallel to the beam direction, providing additional information on relative dose distributions. The planned beams are delivered using static gantry angle but keeping other beam parameters (such as MLC leaf positions, MU, dose-rate, and collimator angles) the same. Other devices such as arrays of diodes or ionization chambers either placed on the treatment couch or attached to the head of the gantry may be used. Similarly, the electronic portal imaging devices (EPIDs) attached to the linear accelerator are used for planar dose measurement with or without the patient present. The measured dose is compared to the dose calculated by the treatment planning system and deviations

greater than 3% may require a re-evaluation of the treatment plan or/ and the measurement setup. The choice of 3% as a tolerance is based somewhat on the dosimetric accuracy needs outlined in section 1.2, but a rigorous justification does not exist [16, 17]. The software that accompanies these dosimeters provide additional quantitative evaluation tools such as dose images, dose volume histogram (DVH) and gamma analysis tests [18]. Planar dose verification can be performed for the individual fields or for the sum of all fields. Other dose verification methods include use of independent MU check, independent dose calculation engine and Monte Carlo technique. Detailed description of the different devices and dose verification processes will be discussed in Chapter 2 of this thesis.

Generally, performing patient specific dose verification of the complex treatment plan using either the point or planar dose measurement technique will help reduce or eradicate treatment delivery errors. This will ultimately result in improved patient care and better outcomes of cancer patients receiving radiation therapy.

1.4 Thesis Overview

The work presented in this thesis describes an investigation of *in vivo* patient dose verification techniques that verify actual treatment delivered to patients. In the radiotherapy field, the term *in vivo* patient dosimetry means the patient dose (at a point or at many points) is estimated via a measurement performed during treatment delivery. Specifically, this work mainly focuses on an entrance dosimetry approach using a novel

2D transmission detector (IBA Dosimetry, Germany), although some work in a later chapter has been generalized and includes exit dosimetry via EPIDs. The major challenges faced in radiation therapy dose verification, summary of the research field and the motivation for this research work are presented in Chapter 2. The research work is separated into three primary investigations representing the three main chapters in this thesis. In Chapter 3, a detailed study of the effect of the contaminant electrons, generated by the entrance transmission detector, on the clinical photon beam was investigated using EGSnrc user codes BEAMnrc and DOSXYZnrc. In Chapter 4, the ability of the entrance transmission detector to accurately measure dose from IMRT and VMAT was investigated by characterising the spatial resolution of the system (via measuring the point spread function), with additional validation provided by Monte Carlo simulation. Finally, a new general research tool that performs Monte Carlo simulations for VMAT treatments, simultaneously tracking dose deposition in both the patient CT data set and an arbitrary planar detector system was developed in Chapter 5. The tool can handle modeling of any type of planar detector system, and positioned as either an entrance or an exit detector. The tool has been made freely available to the medical physics research community to advance the development of planar detectors for use in *in vivo* patient dosimetry applications. These investigations are summarized in more detail in the next three subsections, which are essentially abstracts of these works. The goal of this thesis is to improve the understanding of a novel entrance detector proposed for routine radiation therapy quality assurance. Chapter 6 presents a more detailed summary of the thesis, including a description of possible future work.

1.4.1 Summary of Chapter Three: A Monte Carlo investigation of the contaminant electrons due to a novel in vivo transmission detector

A novel transmission detector, developed as an IMRT quality assurance tool and intended for *in vivo* patient dose measurements, is studied here. The goal of this investigation is to use Monte Carlo techniques to characterize treatment beam parameters in the presence of the detector and to compare to those of a plastic block tray (a frequently used clinical treatment device). Particular attention is paid to the impact of the detector on electron contamination model parameters of two commercial dose calculation algorithms.

The linac head together with the COMPASS transmission detector (TRD) was modeled using BEAMnrc code. To understand the effect of the TRD on treatment beams, the contaminant electron fluence, energy spectra, and angular distributions at different SSDs were analyzed for open and non-open (i.e. TRD and block tray) fields. Contaminant electrons in the BEAMnrc simulations were separated according to where they were created. Calculation of surface dose and the evaluation of contributions from contaminant electrons were performed using the DOSXYZnrc user code. The effect of the TRD on contaminant electrons model parameters in the Eclipse AAA (Varian Medical Systems, Palo Alto, CA) and Pinnacle^3 (Philips Radiation Oncology Systems, Andover, MA) dose calculation algorithms was investigated.

Comparisons of the fluence of contaminant electrons produced in the non-open

fields versus open fields show that electrons created in the non-open fields increase at shorter SSD, but most of the electrons are low energy with large angular spread. These electrons are out-scattered or absorbed in air and contribute less to surface dose at larger SSD. Calculated surface doses with the block tray are higher than those with the TRD. Contribution of contaminant electrons to dose in the buildup region increases with increasing field size for TRD and block tray. The introduction of the TRD results in a 12% and 15% increase in the Gaussian widths used in the contaminant electron source model of the Eclipse AAA dose algorithm. The off-axis coefficient in the Pinnacle^3 dose calculation algorithm decreases in the presence of TRD compared to without the device.

The electron model parameters were modified to reflect the increase in electron contamination with the TRD, a necessary step for accurate beam modeling when using the device. This work is described in detail in Chapter 3.

1.4.2 Summary of Chapter Four: Investigation of the spatial resolution of an online dose verification device

The aim of this work is to characterize a new *in vivo* dose verification device, the COMPASS transmission detector (TRD). The array is composed of 1600 cylindrical ionization chambers of 3.8 mm diameter, separated by 6.5 mm centre-to-centre spacing, in a 40x40 arrangement.

The line spread function (LSF) of a single ion chamber in the detector was

measured with a narrow slit collimator for a 6 MV photon beam. The 0.25x10 mm^2 slit was formed by two machined lead blocks. The LSF was obtained by laterally translating the detector in 0.25 mm steps underneath the slit over a range of 24 mm and taking a measurement at each step. This measurement was validated with Monte Carlo simulation using BEAMnrc and DOSXYZnrc. The pre-sampling modulation transfer function (MTF), defined as the Fourier transform of the line spread function, was determined and compared to calculated MTFs obtained via both Monte Carlo and analytical methods. Two clinical head-and-neck IMRT fields were measured using the device and were used to validate the LSF measurement. These fields were simulated with the BEAMnrc Monte Carlo model and the Monte Carlo generated incident fluence was then convolved with the measured 2D detector response function (i.e. derived from the measured LSF) to obtain calculated dose in the TRD. The measured and calculated dose distributions were then quantitatively compared using χ comparison criteria of 3% dose difference and 3 mm distance-to-agreement for 'in-field' points (defined as those above the 10% maximum dose threshold).

The FWHM of the measured detector response for a single chamber is 4.3 mm, which is comparable to the chamber diameter of 3.8 mm. The measured MTF was calculated and the resolution of one chamber was estimated as 0.25 lp/mm from the first zero crossing. For both examined clinical IMRT fields, the χ comparison between measured and calculated dose showed good agreement with 95.1% and 96.3% of in-field points demonstrating $\chi<1.0$ for field 1 and 2 respectively (with an average χ of 0.29 for IMRT field 1 and 0.24 for IMRT field 2).

The LSF for a new novel entrance detector has been measured at 6 MV using a narrow slit technique and this measurement has been validated by Monte Carlo simulation. The detector response function derived from line spread function has been applied to reproduce measured IMRT fields. This work is described in Chapter 4.

1.4.3 Summary of Chapter Five: A Monte Carlo tool for evaluating VMAT and DIMRT treatment delivery including planar detectors

The aim of this work is to describe and validate a new general research tool that performs Monte Carlo (MC) simulations for volumetric modulated arc therapy (VMAT) and dynamic intensity modulated radiation therapy (DIMRT), simultaneously tracking dose deposition in both the patient CT geometry and an arbitrary planar detector system. The tool is generalized to handle either entrance or exit detectors and provides the simulated dose for the individual control-points of the time-dependent VMAT and DIMRT deliveries.

The MC simulation tool was developed with the EGSnrc radiation transport. For the individual control point simulation, we rotate the patient/phantom volume only (i.e. independent of the gantry and planar detector geometries) using the gantry angle in the treatment planning system (TPS) DICOM RP file such that each control point has its own unique phantom file. After MC simulation, we obtained the total dose to the phantom by summing dose contributions for all control points. Scored dose to the sensitive layer of

the planar detector is available for each control point.

To validate the tool, three clinical treatment plans were used including VMAT plans for a prostate case and a head-and-neck case, and a DIMRT plan for a head-and-neck case. An electronic portal imaging device (EPID) operated in 'movie' mode was used with the VMAT plans delivered to cylindrical and anthropomorphic phantoms to validate the code using an exit detector. The DIMRT plan was delivered to a novel transmission detector, to validate the code using an entrance detector. The total MC 3D absolute doses in patient/phantom were compared with the TPS doses, while 2D MC doses were compared with planar detector doses for all individual control points, using the gamma evaluation test with 3%/3mm criteria.

The MC 3D absolute doses demonstrated excellent agreement with the TPS doses for all the tested plans, with about 95% of voxels having $\gamma<1$ for the plans. For planar dosimetry image comparisons, we defined an acceptable pass rate of >90% of percentage pixels with $\gamma<1$. We found that over 90% of control points in the plans passed this criterion. In general, our results indicate that the simulation tool is suitable for accurately calculating both patient/phantom doses and planar doses for VMAT dose delivery. The tool will be valuable to check performance and advance the development of *in vivo* planar detectors for use in measurement-based VMAT dose verification. In addition, the tool can be useful as an independent research tool for VMAT commissioning of the TPS and delivery system. This work is described in Chapter 5.

1.5 Bibliography

1. Organization, W.H., *Cancer Mortality and Morbidity*. 2012.
2. Podgorsak, E.B., Radiation Oncology Physics: A Handbook for Teachers and Students. International Atomic Energy Agency, 2005.
3. Hall, E.J. and A.J. Giaccia, *Radiobiology for the Radiologist*. 2006: Lippincott Williams & Wilkins.
4. Otto, K., Volumetric modulated arc therapy: IMRT in a single gantry arc. Medical Physics, 2008. **35**: p. 310.
5. Ezzell, G.A., et al., Guidance document on delivery, treatment planning, and clinical implementation of IMRT: Report of the IMRT subcommittee of the AAPM radiation therapy committee. Medical Physics, 2003. **30**: p. 2089.
6. Mijnheer, B. and D. Georg, *Guidelines for the verification of IMRT.* Estro booklet No, 2008. **9**.
7. Low, D.A., et al., *Dosimetry tools and techniques for IMRT.* Med Phys, 2011. **38**(3): p. 1313-1338.
8. Schneider, U., et al., Estimation of radiation-induced cancer from three-dimensional dose distributions: Concept of organ equivalent dose. International Journal of Radiation Oncology Biology Physics, 2005. **61**(5): p. 1510-1515.
9. Schneider, U., et al., *The impact of IMRT and proton radiotherapy on secondary cancer incidence.* Strahlentherapie und Onkologie, 2006. **182**(11): p. 647-652.
10. Nishio, S., et al., Radiation-induced brain tumours: potential late complications of radiation therapy for brain tumours. Acta neurochirurgica, 1998. **140**(8): p. 763-

770.

11. Brahme, A., *Dosimetric precision requirements in radiation therapy.* Acta Oncologica, 1984. **23**(5): p. 379-391.
12. ICRU, Determination of absorbed dose in a patient irradiated by beams of X or gamma rays in radiotherapy procedures. ICRU Report 24. 1976, Bethesda, Maryland.
13. Mijnheer, B., J. Battermann, and A. Wambersie, *What degree of accuracy is required and can be achieved in photon and neutron therapy?* Radiotherapy and Oncology, 1987. **8**(3): p. 237-252.
14. Ahnesjö, A. and M.M. Aspradakis, *Dose calculations for external photon beams in radiotherapy.* Physics in medicine and biology, 1999. **44**: p. R99.
15. Brahme, A., Accuracy requirements and quality assurance of external beam therapy with photons and electrons. Acta Oncologica, 1988. **15 (Suppl.1)**: p. 1-76
16. Kruse, J.J., On the insensitivity of single field planar dosimetry to IMRT inaccuracies. Medical Physics, 2010. **37**: p. 2516.
17. Nelms, B.E., H. Zhen, and W.A. Tomé, Per-beam, planar IMRT QA passing rates do not predict clinically relevant patient dose errors. Medical Physics, 2011. **38**(1037).
18. COMPASS User's Guide version P-05-008-510-001 03. (IBA Dosimetry, Schwarzenbruck, Germany).

CHAPTER TWO: INTRODUCTION

2.1 Radiation Therapy for Cancer Patients

Radiation therapy is the treatment of cancer patients with the use of high-energy radiation such as x-rays, gamma rays, electrons, protons, and others. The majority of cancer patients receive radiation treatments using a medical linear accelerator (linac). The linac head shown in figure 2.1 consists of many components that contribute to forming and shaping the radiation beam delivered to a patient [1-3]. Most treatments are achieved using photons (x-rays) that are produced when fast electrons generated in the linac are incident on a target of high atomic number, such as tungsten. The photon beam produced is collimated by the primary collimator positioned immediately below the target. The forward directed collimated beam then typically passes through a flattening filter, which creates a beam of uniform intensity across the field. The flattening filter is typically made of a medium range atomic number material, such as steel or copper. The flattened beam then passes through an ion chamber that monitors dose rate, integrated dose, and field symmetry of the beam. The secondary collimator (jaws) located after the ion chamber are used to further collimate the beam. The secondary collimator consists of two pairs of jaws (in-plane and cross-plane), typically made of tungsten. The jaws are independently positioned, allowing the creation of rectangular fields from 0 x 0 cm^2 to a maximum field size of 40 x 40 cm^2, projected to a standard distance of 100 cm from the target (i.e. projected to the isocenter of the beam).

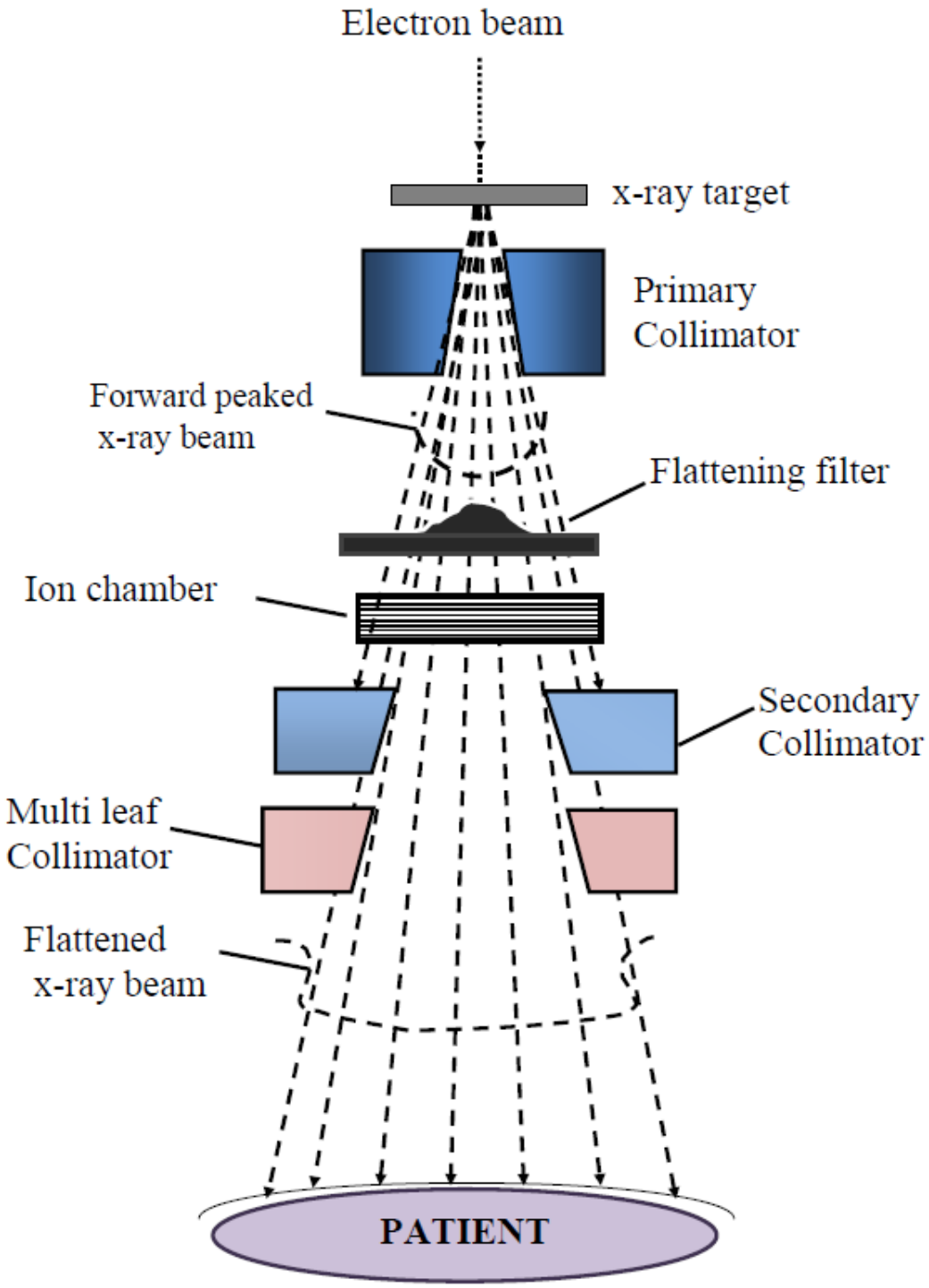


Figure 2-1: Description of the different components in a medical linear accelerator.

Another important component in the linac head is the multi-leaf collimator (MLC) which was originally developed to collimate the treatment beam to the shape of the target in the patient. The MLC (Figure 2.2) consists of large number of collimating leaves (typically 80 to 160), each under individual motorized computer control. The leaves are made of tungsten alloy and individual leaf widths are typically 0.5 to 1.0 cm, as projected to isocenter [1-3].



Figure 2-2 A multi-leaf collimator (MLC) used to create simple and complex fields.

Modern treatment techniques employed in the clinic are generally classified as three-dimensional conformal radiation therapy (3D-CRT) or intensity modulated radiation therapy (IMRT). 3D-CRT is a form of external beam radiation therapy that uses computer software to create a three-dimensional (3-D) image of the tumour so that multiple radiation beams from different directions can be shaped to closely match the projected outline of the treatment volume (i.e. 'conformal'). In this technique, radiation

beams that are of uniform intensity across the field are delivered to the patients. Also, external devices such as wedges or compensators may be used to alter the two-dimensional shape of the beam intensity to account for contour irregularities or to generate more uniform dose distributions in three dimensions [1-3]. Intensity modulated radiation therapy (IMRT) is an advanced form of conformal radiation therapy that uses computer algorithms to inversely design (i.e. based on the geometry of the tumour and the nearby organs) the fluence patterns of the treatment beams required to deliver an 'optimal' treatment. The optimal treatment is defined by a human operator as a series of dose objectives that the inverse planning algorithm tries to satisfy, such as a uniform high dose within the target volume, and reduced dose to the organs at risk (OARs). The linac is able to deliver these often complex fluence patterns by using the multileaf collimator to modulate the fluence by methods described below. The subsequent dose distributions from IMRT are highly conformal and result in steep dose gradients between planning target volumes and organs at risk.

Common IMRT delivery methods used in the clinic are based on the multi-leaf collimator (MLC) and are divided into three categories [1, 3] – (i) the segmented (or static) MLC technique, often referred to as the 'step and shoot' method, (ii) the dynamic MLC (DMLC) technique, referred to as the sliding window method, and (iii) Volumetric modulated arc therapy. In the step and shoot mode the radiation beam is only turned on when the MLC leaves are stationary in each of the prescribed subfield positions during delivery. In the DMLC mode (dynamic IMRT) the delivery of the intensity modulated fields are carried out while the leaves of the MLC are moving continuously during patient

treatment. The treatment time using DMLC is much less than the segmented MLC technique, with a typical delivery time of 14 minutes for a five-field prostate treatment versus 30 minutes using the step and shoot method [4]. Volumetric modulated arc therapy (VMAT) delivery method uses the sliding window approach while the gantry rotates around the patient, with the beam on continuously. In addition to the dynamic MLC motions [5], this treatment delivery may also involve variable gantry rotation speed, variable dose rate, and theoretically could include collimator and couch rotations. Studies have shown that VMAT dose distributions for prostate and cervical cancer have better sparing of OARs than 3DCRT and even static field IMRT [6, 7]. It offers the ability of generating highly conformal dose distributions at reduced time (less than 5 minutes).

Before patient treatment, a customized radiation therapy treatment plan is designed using a commercial treatment planning system (TPS) which simulates the radiation beam incident on a computer model of the patient (usually a computed tomography, or CT, data set). The IMRT treatment planning system uses inverse iterative planning in which several treatment plans are generated and evaluated before selecting a plan for delivery. For each plan, a cost function based on the dose objectives (i.e. constraints, penalties, targets, etc.) specified for the planning target volume (PTV) and critical organs is assessed. The inverse planning process attempts to reduce the cost function for each iteration, and a minimum cost function is achieved after many attempts. The segmentation of the MLC leaves is carried out and the final dose calculation is evaluated by viewing the dose volume histograms (DVHs) and isodose curves in

orthogonal planes, individual slices, and/or 3-D volume surfaces. Due to the complexity involved in radiation therapy treatment, especially IMRT techniques, comprehensive dose verification of the customized patient treatment plan and quality assurance procedures of delivery techniques and equipment are recommended before the delivery of treatment to the patient [8].

2.2 Methods of Dose Verification in Radiation Therapy

The use of IMRT and VMAT treatment techniques for the treatment of different tumour sites has increased dramatically in recent years [5, 9, 10]. As described in section 2.1, these techniques do not only result in the delivery of highly conformal dose to the tumour but also result in steeper dose gradients which helps reduce dose to surrounding normal tissue structures. The benefit of these advanced procedures is an adequate or improved tumour control with reduced normal tissue complications. However, this goal may not always be achieved in practice due to several limiting factors such as: 1) inaccuracy of the TPS dose calculation algorithm 2), errors in treatment plan data transfer to the treatment machine, 3) machine-related delivery errors (for example, incorrect leaf positions or incorrect monitor units (MUs)) and, 4) patient-related errors, both inter-fractional and intra-factional. Inter-fractional errors are changes in patient anatomy position and shape between the time of CT simulation and each fraction of the treatment delivery occurring daily over 4-8 weeks. Common sources of inter-fractional errors are differences in patient position, organ filling (shape and volume change), patient weight gain/loss, and tumour shape and/or size (due to growth or shrinkage). Intra-fractional

errors are changes in patient anatomy *during* treatment delivery, and are mostly caused by variable organ motion and involuntary movement, such as respiration-induced organ motion, cardiac motion, bladder filling, rectal filling, e.t.c. For example, typical uncertainties for inter-fractional and intra-factional setup errors of head and neck cancer are 2.0 mm and 1.1 mm respectively [11]. These factors will typically have a limited precision that will contribute to the overall uncertainty in the dose delivery process. To reduce or eliminate errors that are not patient-related, dose verification of the customized treatment plan is recommended to ensure that the intended dose is delivered accurately during patient treatment [8, 12, 13]. Verification of the TPS calculated dose may involve the measurement of the delivered dose, an independent dose calculation of the treatment plan, or a combination of both methods.

Several measurement-based dose verification methods have been reported in the literature [14-21], typically involving the comparison of a pre-calculated radiation dose from the TPS to a measurement of the actual delivered radiation dose using one or multiple detectors. Commonly this measurement is made sometime before the patient's first treatment, and without the patient actually present. This approach is known as 'pre-treatment verification'. Pre-treatment dose verification measurements can be made in different configurations, commonly at one or more points or a plane inside a simple geometric phantom or anthropomorphic phantom [16, 17]. The type of detector used determines the dimensionality of the measurement; for example ionization chambers, diodes, or TLD's will provide dose data at single measurement points, while film and arrays of diodes or ionization chambers will provide two dimensional (i.e. 2D) planes of

dose measurement. Gel dosimeters have the ability to measure dose deposited in three dimensions (i.e. 3D). The goal of pre-treatment dose verification is to effectively and independently verify that the customized patient treatment plan is reproduced (to within a specified tolerance) by the treatment unit. However, pre-treatment dose verification has the disadvantage of being performed without the patient present, while a more comprehensive approach would be *to verify the dose that is actually delivered to the patient at the time of treatment.* This is generally described with the terminology of *in vivo* dosimetry. *In vivo* dosimetry is not commonly performed in North American clinics, but several international organizations (AAPM, ICRU, NACP, and UK Department of Health) have recommended its used [22-25]. Depending on the specific measurement method, it can detect patient-related errors in addition to machine-dependent errors, and dose calculation as well as data transfer errors that could be missed if only a pre-treatment verification was performed. In addition it documents that the planned dose is accurately delivered to individual patients for each treatment, within well-defined action limits. *In vivo* dose measurements can be carried out either invasively, by inserting a detector into the patient, or non-invasively by measuring the surface dose (on the patient) at a beam entrance point [18-20] or exit point [15, 26-28]. If one replaces the point detectors with a 2D array of detectors, the signal due to the entire delivered beam fluence may be captured instead of that due to just a single point. Measured entrance dose by these detectors is either directly reported or may be translated into fluence and forward projected into a virtual phantom or patient CT data set to calculate dose, which can then be compared to the desired dose from the TPS. Measured exit dose can also be converted to fluence, backprojected to a desired plane and also then converted into a calculated

patient dose for comparison to the TPS dose. The main difference between entrance and exit dose measurements is that the patient modulates the beam measured by exit detectors and takes into account patient position, while the entrance detectors only measure the radiation beam emanating from the linac head. Entrance dose measurements may be used to check beam characteristics and/or performance of a treatment device, leaf positioning, and the calculation of the number of monitor units. Exit dose measurements may be performed to check the relative dose calculation algorithm and to determine the effect of shape, size, and density variations of the patient on the dose calculation process [21, 29, 30].

2.3 Dosimetry Systems for Dose Verification

To accurately and reliably measure deposited dose in the context of radiation therapy, the detectors need to possess several characteristics. Use of a detector composed of tissue-equivalent material, i.e. exhibiting similar radiation interaction properties, is desirable [31]. However, this is not always possible due to design limitations, so sometimes detectors used for dose verification require corrections to be applied to their readings. Aside from this, desirable characteristics for detectors include: high spatial resolution (when measuring steep dose gradients), dose and dose-rate linearity, excellent reproducibility, energy independence, and directional independence [13, 31]. Detectors with high spatial resolution are desired for dose verification of highly modulated beams such as those encountered in IMRT and VMAT that deliver steep dose gradients to the patient, in order to reduce the volume averaging effect. Volume averaging effect occurs

when the measured detector signal is averaged over the active volume of a detector. It occurs when an ion chamber is placed in a region with a steep dose gradient, such as a penumbra region [13]). The detector should be able to produce the same results under similar conditions (i.e. have good reproducibility). Since detectors are calibrated for a certain energy or energy spectrum but are often used over a wider energy range, the energy dependence could vary with radiation quality and therefore require a correction. Therefore, the ideal detector would be independent of energy and could be used without the need for this correction. Directional dependence of detectors is most commonly encountered with diode detectors due to the asymmetry inherent in the silicon chip with the depletion layer closer to the surface of the diode. It can be a significant effect, up to 3% of the measured dose [14, 31, 32].

As mentioned in the previous section, dose measurements of complex treatment techniques may be carried out using a variety of detectors or detector systems with different geometries – single-point (0D), linear (1D), planar (2D), and volumetric (3D) geometries. Gel dosimeters, the only available true 3D detector, are not widely used for routine patient-specific dose verification because of cost and practical limitations which includes additional equipment for readout of dose and requirement of additional personnel to establish gel dosimetry in cancer centers [14].

2.3.1 Zero -Dimensional (Point) Detectors

Point detectors such as ionization chambers, metal oxide semiconductor field

effect transistors (MOSFETs), and diodes, placed inside a phantom can be used for verification of dose at a single point, usually inside the target volume. These detectors have been used for *in vivo* entrance and exit dose measurements especially when a critical organ is in close proximity [14, 19, 20]. In general, point detectors are fast and simple to use and are suitable for absolute dose measurement. However, they have a number of limitations which must be considered including: they may not be reusable (MOSFETs), they may have limited spatial resolution (ion chambers), they may be non-tissue equivalent (diodes), and observed differences between calculated dose and measured dose may be difficult to relate to target volume coverage or dose to normal tissue [14].

2.3.2 Two Dimensional (Planar) Detectors

Unlike point dose measurements, planar dose measurements provide a 2D distribution of measured dose, and can be oriented in a plane in front of, inside, or behind a phantom. The measured dose distribution can be compared to a 2D dose calculated with a TPS, for the same location and phantom configuration. Differences between measured and calculated doses in the target structures and in the normal tissue structures can be visualized or quantified. Commonly used planar dosimeters for verification of complex treatment plans include film (e.g. radiographic or radiochromic), diode arrays, ionization chambers arrays, and electronic portal imaging devices (EPIDs). Radiographic film has been widely used for relative dose measurements but requires chemical processing and over-responds to low energy photons [33]. In recent years, the use of radiochromic film for dose verification has increased because of its near tissue-equivalence and its self-

developing properties [34]. However radiochromic films exhibit post-irradiation instability [14], which inconveniently requires waiting for several hours for the film image to 'set' after irradiation. In general, the spatial resolution of film is superior to most other dosimeters, which makes it a useful tool in measuring planar dose distributions in high dose gradient regions [34]. To achieve optimal results, careful handling, processing, and digitizing are required [35]. Thus film dosimetry is time consuming and labour intensive.

Planar dose measurements are also possible with an array of diode or ionization chamber dosimeters. It has been shown that a 2D diode array is an effective tool for the verification of calculated doses of complex techniques [36]. Letourneau *et al* performed a dosimetric characterization and evaluation of MapCheck (developed by Sun Nuclear Corporation, Melbourne, Florida), a commercial 2D diode array, for dose verification of IMRT fields [37]. They found that the device is linear with dose up to 295 cGy, has a temperature dependence of about 0.57%/^{0}C and recommended that this should be corrected for when performing absolute dose measurements. Comparing MapCheck measured IMRT fields with films using gamma index criteria of 3%/2mm they found 99.6% of the diodes agree with film measurements but using tighter distance-to-agreement tolerances of 5%/1mm and 3%/1mm the percentage diode agreement reduced to 99.0% and 95.6% respectively. They concluded that the device provides the necessary characteristics for performing dosimetric verification of IMRT and would be a useful IMRT QA device in the clinic [37]. Since the publication of this study in 2003 several others studies showing clinical implementation of the device have been performed and

reported in the literature [38-40]. Some of the characteristics of diodes include: high spatial resolution, immediate availability of the measured dose, high sensitivity, and high reproducibility [14, 20, 35]. However, diodes have several limitations including; non tissue-equivalence, variation in dose response with temperature, and angular dependence to the incident radiation beam [14, 35]. Various 2D arrays of ionization chambers with typical spatial resolution of between 3.8 mm and 5 mm have been developed and evaluated [41-43] for dose verification of complex delivery techniques. Stasi *et.al* used PiXel-segmented ion chambers (PXC/MatriXX) consisting of 1024 chambers, in the verification of 19 fields of dynamic IMRT. Measured dose distributions obtained via MatriXX were compared with film and with TPS-calculated dose distributions. Using gamma index criteria of 3%/3mm, they found 97.7% and 97.6% of MatriXX pixels agreed with film and TPS respectively [42]. In a different study, a 2D array of ionization chambers (PTW Type10024) was shown to obey the Nyquist sampling theorem and suitable for IMRT dose verification [41]. In general, ionization chambers provide real-time measurements, are relatively sensitive except when designing with small volume chambers, are highly reproducible, and can be used as a reference dosimeter. However, ionization chambers have inferior spatial resolution compared to film and diodes. In addition, the leakage effect, which may occur as a result of the irradiation of insulators and chamber parts, can affect dose measurements using ionization chamber and they may require several correction factors to remove this perturbation [13, 14].

Another important radiation dosimeter for planar dosimetric verification of complex techniques is the electronic portal imaging device (EPID). The 2D geometry,

digital and real-time nature, and convenience of EPIDs (they are commonly mounted directly on the linear accelerator) have made them attractive in IMRT patient dose verification. Currently, the flat panel, amorphous silicon (aSi) detector is the most common EPID available clinically. Although EPIDs were originally designed for geometric verification of patient positioning, recently they have been investigated for dosimetric verification [44]. The dosimetric characteristics of EPIDs have been studied by several investigators [45-47], revealing a strong potential for patient dose verification. EPIDs offer the advantage of high spatial resolution, minimum setup time for dose measurements, and the potential for *in vivo* dose verification [44]. However, a-Si EPIDs over-respond to low energy photons and show a field–size dependent response [48, 49]. Several correction methods to overcome these problems have been suggested in the literature [48, 49]. Conceptually, the two main scenarios for *in vivo* EPID dosimetry involve either forward projection to calculate an exit image, or backward projection to calculate patient dose (Figure 2.3). In the forward approach, 2D measured transmission dose in the EPID is compared to a predicted 2D transmission dose image, while in the backward approach the measured EPID dose is converted to fluence and used to reconstruct dose in the patient 3D model and compared to desired patient 3D dose from the treatment planning system [31].

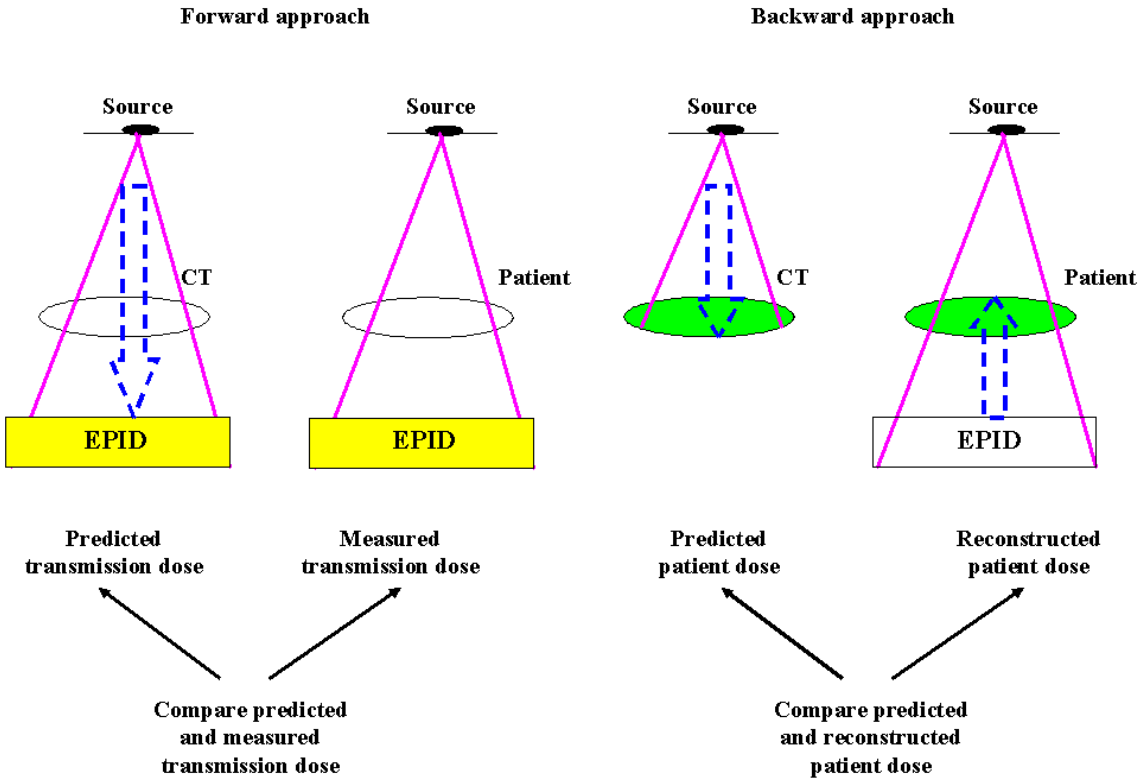


Figure 2-3: Two different approaches for using portal imaging for *in vivo* dosimetry. In the forward approach, predicted and measured transmission doses are compared while in the backward approach, predicted and reconstructed patient dose from measured transmission dose are compared.

2.4 Physics of Ionization Chambers

In radiation therapy, radiation detectors measure dose using either of two different approaches – direct or indirect methods. In the direct method, incident radiation interacts with the medium of detection directly, for example radiation interacts directly with the gas in ionization chambers to create charges that are measured by electrometer. In the

indirect method, radiation interacts with an intermediate medium, generating a secondary signal which is then used to measure dose. For example, radiation interacts with a scintillating medium to generate optical photons, which then deposit their energy in the medium of detection for example in the optical diodes of an electronic portal imaging device (EPID). The understanding of the characteristics and the limitations of the ionization chambers used for dose verification is an important part of this project. This section provides some introductory description of the physical basis of ionization chambers.

An ionization chamber is a gas-filled detector designed to measure charge generated by radiation-induced ionization events. The chamber consists of a measuring volume (typically shaped like a cylinder), a central and outer electrode (typically the chamber wall) across which a voltage is applied [50]. When incident radiation interacts with the gas, the photon's energy is transferred to orbital electrons that are ejected and positively charged ions are created. The electric field created by the applied voltage results in the movement of the electric charges towards the electrodes of opposite polarity, creating a current that can be measured using an electrometer. When the chamber operates at low voltages, ionic recombination occurs because the electric charge from the gas that reaches the electrodes is relatively small. However, as the voltage increases the signal increases since a large portion of the charge is collected before recombination. As voltage increases, the signal reaches a saturation value where all the ion pairs created in the gas are collected and this saturation region is called the ionization chamber region. Beyond this region one surpasses the 'multiplication threshold', where

increasing the voltage results in increased acceleration of the electrons causing increased collisions with gas molecules and the corresponding increased release of additional electrons, thus described as a multiplication effect. At still higher voltages, the state of continuous discharge is reached where the response size of the detector is independent of the number of electrons generated by the initial events. As one increases the applied voltage of the detector beyond the multiplication threshold, it will operate in the *proportional region, limited proportionality region, Geiger region,* and *continuous region* [2]. Typical applied voltage values for ionization chambers used in radiation therapy operating in the saturation region are between 200 V and 400 V.

There are two main types of ion chambers – cylindrical chambers and parallel-plate chambers (figure 2.4 a & b). Generally, cylindrical chambers are used for absolute or reference dose measurements because of convenience, precision and tissue equivalence of low-Z cavity. They are provided with the calibration factor (N_K or $N_{D,w}$) to determine the dose to water at a reference point [51, 52]. Parallel-plate chambers are preferred in regions with steep dose gradient in the beam direction, such as the build-up region in a megavoltage photon beam. The relatively large size of cylindrical chambers (typically about 6 mm) is not suitable for accurate dose measurement in the build-up region while plane parallel chambers offer improved spatial resolution (generally 2 mm) in this region [2].

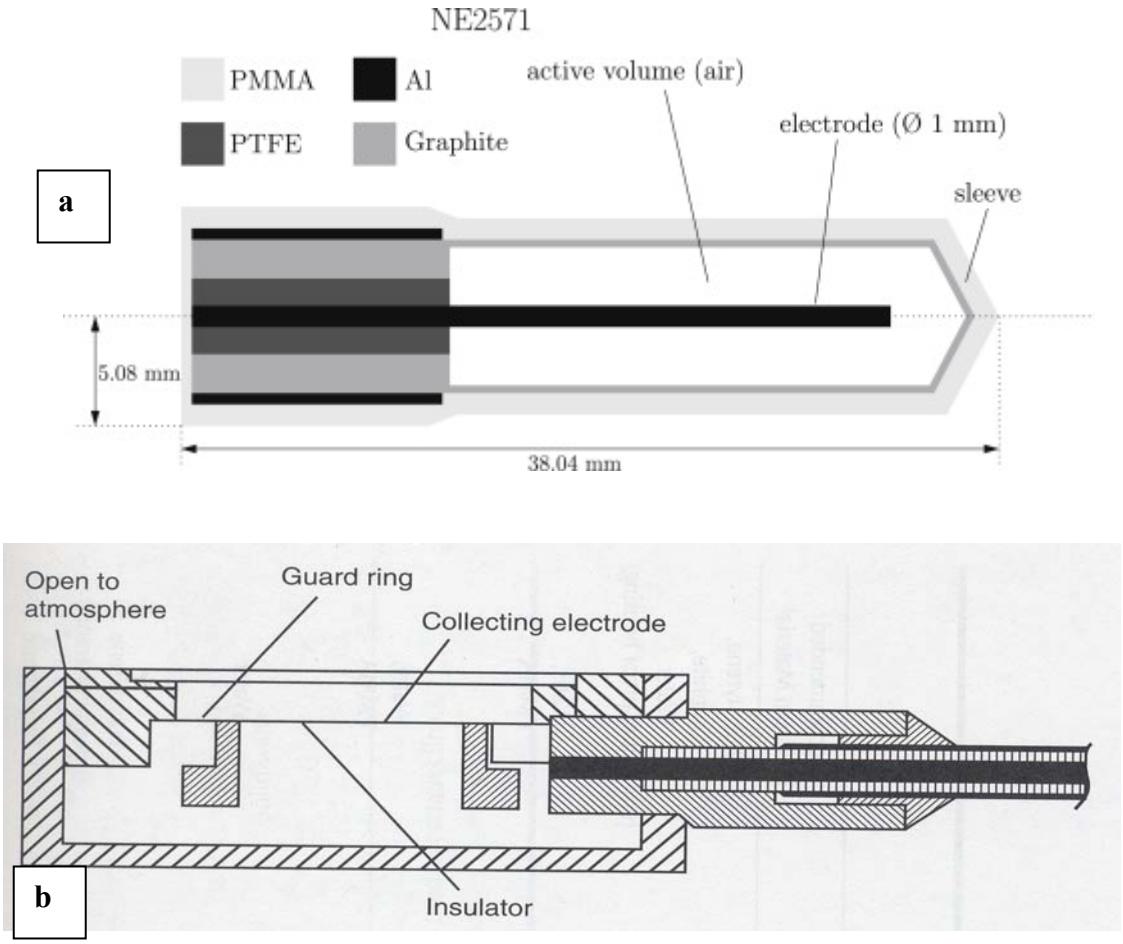


Figure 2-4: (a) A Farmer-type ionization chamber (b) Plane-parallel ionization chamber

2.5 The COMPASS System

The COMPASS system (IBA Dosimetry, Germany) is a novel dose verification tool, which can be implemented as part of a patient specific QA program in the clinic. It consists of a transmission detector (TRD) together with dose calculation software. It estimates the fluence delivered by the linac via measurement using the TRD (Figure 2.5)

during patient treatment and uses this to perform a three-dimensional dose reconstruction in the patient model. The suitability of using the detector during IMRT and VMAT patient treatments is a main goal of this thesis.

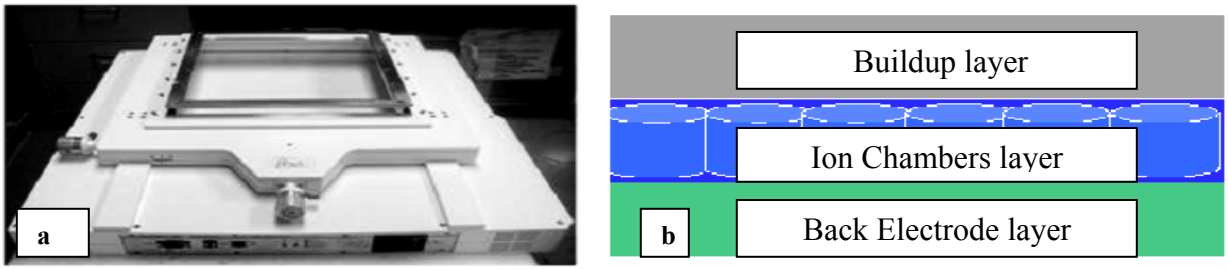


Figure 2-5: (a) Photo of the transmission detector (not inserted into the treatment unit) and (b) cross section of transmission detector modeled as three layers.

The TRD mounts in the head of the treatment machine and samples the beam fluence that will enter the patient, and is thus described as an 'entrance' detector. It consists of a 2D array of 1600 vented plane parallel ionization chambers arranged in a uniform 40 x 40 grid. Each chamber is 3.8 mm in diameter and 2 mm in height, giving a sensitive volume of 0.02 cm^3. The center-to-center chamber distance is 6.5 mm. The outer dimension of the TRD is 490 x 110 x 520 mm^3 and the mass is 16.4 kg. The detector design includes a top layer of 3 mm water-equivalent RW3 material (density 1.045 g/cm^3). The back electrode layer of the detector consists of thin layers of copper and insulating materials with a water equivalent thickness of approximately 4 mm. The air in the chambers is ionized when irradiated and the released charge is separated by means of an electric field applied across the electrodes. The measured current,

proportional to the dose rate, is digitized by a 1600 non-multiplexed channel analog-to-digital converter and recorded as detector 'counts'[53]. Measured signal is corrected for local changes in air density in the chamber cavities by internal temperature and pressure sensors in the detector. The detector has four modes for measuring signal: in the *free mode*, the user can start and stop signal integration manually; in the *single shot mode*, the user sets the integration time and starts measurement manually; in the *movie mode*, the user specifies a frame sampling period and the system acquires measurements continuously while the beam is on; and in the *trigger mode*, a variation of the movie mode, signal acquisition automatically starts when a small threshold current is detected in the system. The manufacturer recommends that device be pre-irradiated with a 10 Gy dose using a 40 x 40 cm^2 field size to cover the entire detector array before measurements, to improve detector stability.

Several 2D dosimeters including TRD, DAVID (PTW-Frieburg, Germany) and AIMS (developed by Islam *et al*) have been introduced for dose verification through entrance fluence dosimetry, which has been a focus of increasing research interest [43, 54, 55]. These devices can be used for *in vivo* entrance dose measurements, for checking beam characteristics and performance of a treatment device, leaf positioning, and measuring the number of monitor units delivered during patient treatment. While the use of these devices has the potential of contributing positively to treatment outcomes, major concerns include: influence on the photon beam, effect on patient surface dose (via contamination of the beam with secondary electrons), and the effect of large individual detector element sizes on measured IMRT and VMAT fluence. Studies that investigate

the first two major concerns for these devices have been performed [41, 43, 54, 56]. Venkataraman *et al* [43] examined the influence of the TRD on a 6 MV photon beam specifically investigating the effect of the detector on surface dose and dose in the build up region. The authors showed that the device increases the dose in the build up region but has little or no effect beyond the depth of maximum dose (d_{max}). In addition, the authors compared the attenuation of the TRD with a standard block tray and found that both devices have similar effect on photon beam. Note that this author performed the Monte Carlo validation of dose measurement in the build up region and the full paper describing the work is included in Appendix A of this thesis. Unlike other entrance dose devices, the TRD is accompanied by software that includes a full dose calculation engine capable of taking the measured entrance dose, converting to a fluence estimate, and predicting dose delivered to the patient.

The dose calculation software included with the COMPASS system consists of a physics-based fluence model (i.e. head fluence model) and a point-dose kernel convolution/superposition patient dose calculation engine. The fluence model computes a fluence using the model of linac and treatment planning system RT plan. This fluence is used with predicted model to calculate the detector response. A measured detector response (R_{meas}) is obtained directly using the TRD. Then the calculated fluence is corrected using a convolution kernel created by using the calculated and measured detector response function (see figure 2.6). The resulting estimate of incident fluence is then forward projected into the patient model to calculate dose (D_{RC}) [57, 58]. It is noted that the method of deriving detector response and fluence from measured dose is not

described in detail by the manufacturer [53].

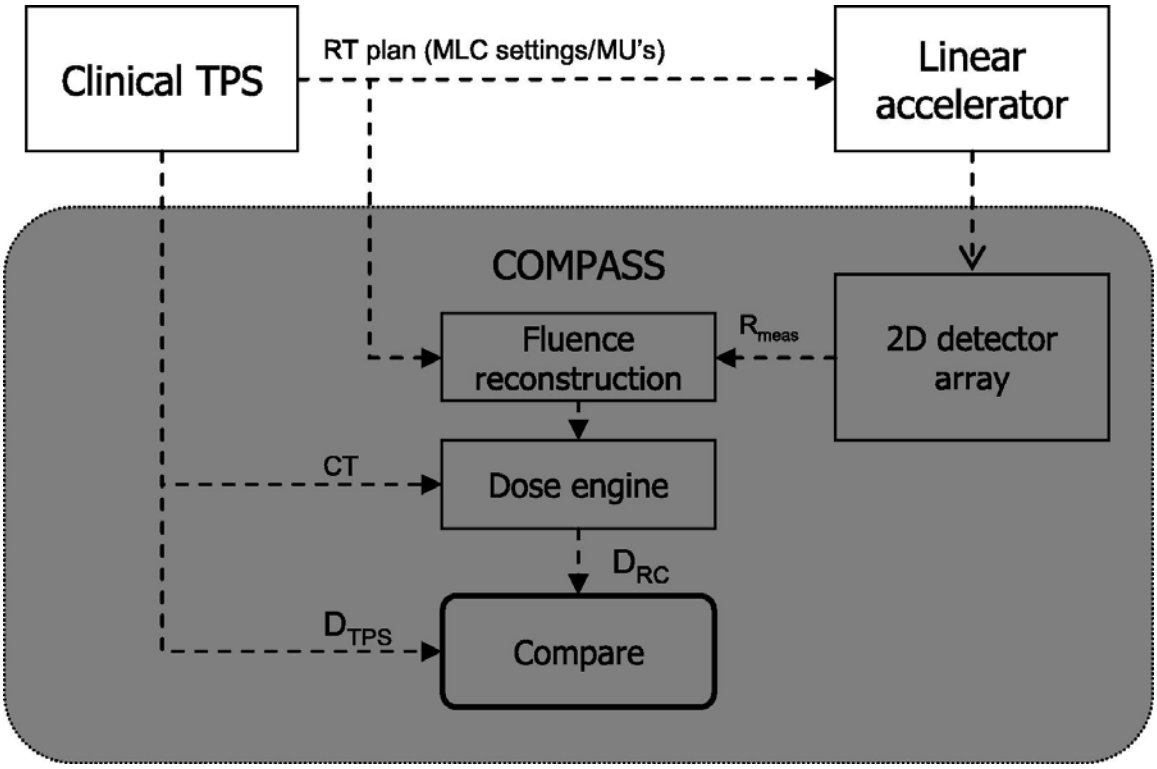


Figure 2-6: A schematic of dose reconstruction method in the COMPASS system. The RT plan from the TPS is exported to the software. Measurement of the plan with the TRD (R_{meas}) is used to reconstruct the fluence and to reconstruct the dose in the patient/phantom CT (D_{RC}).

Similar to treatment planning system commissioning, the parameters in the beam model of the COMPASS software are adjusted to match a specific treatment machine or multiple machines with identical parameters. The beam commissioning requires a set of depth dose curves for different square field sizes, two-sided cross-plane and in-plane dose profiles for different depths and field sizes, as well as output factors measured for a set of

field sizes and an absolute monitor unit calibration. In addition it requires a transmission factor to correct for the photon beam attenuation by the TRD. The beam model parameters used for commissioning of the treatment machine are fixed once and the machine-specific beam model can then be used for dose reconstruction. The beam fluence model in the software is quite detailed and includes focal and extra-focal source components (Gaussian shaped), arbitrary primary beam spectrum, arbitrary initial fluence shape, off-axis energy spectra softening, MLC leaf-end shape control, and transmission factors for both jaws and MLC.

The dose calculation in the software uses a convolution/superposition method [53, 59]. In this method, the dose calculation at each point in the medium considers primary photon interactions throughout the surrounding volume by integrating the dose contributions from each irradiated volume. The dose calculation is performed in a three-step process using (1) scaling of the measurement-derived beam fluence at a plane upstream of the patient surface, (2) calculation of TERMA (total energy released per unit mass) within the patient volume, and (3) superposition of point-dose kernels with the TERMA distribution. The calculated dose distribution *D(r)* in the patient model at point r in the volume is given by [53] :

$$D(r) = \int \frac{\mu(r')}{\rho(r')} \Psi(r') A(r - r') dr' \qquad (2.1)$$

where μ/ρ is the mass attenuation coefficient, Ψ(**r'**) is the photon energy fluence and A(**r-r'**) is the point spread kernel.

For comparison purposes, patient plan data from the clinical TPS may be imported into COMPASS software via DICOM (Digital Imaging and Communications in Medicine), including the calculated three-dimensional patient dose. A quantitative evaluation is performed using isodose distributions (overlaid on CT anatomy), dose volume histograms (DVHs) and gamma analysis. In addition, the software generates a report that contains results of the comparison between the reconstructed dose and the TPS calculated dose.

The TRD may be used as an *in vivo* IMRT or VMAT quality assurance tool and therefore is a source of contaminant electrons in the photon treatment beam. This could potentially affect prescribed dose to patients. In Chapter three of this thesis, the Monte Carlo technique is used to investigate the influence of the transmission detector on a 6MV photon beam typically used for IMRT and VMAT delivery. Also, the characterization of the system performance of the device by determining its spatial resolution and investigating the effect of pixel size on entrance dose of IMRT fields is the subject of Chapter four of this thesis. The accuracy of entrance fluence measured by the TRD was validated with Monte Carlo technique.

2.6 Electronic Portal Imaging Devices

EPIDs were originally developed for verifying patient position through anatomical imaging using the exiting megavoltage treatment beam. Since the EPID imagers are of reasonably high resolution, provide real-time imaging, and are conveniently mounted on

the radiation treatment units, there has been strong interest in using them as dosimeters. The current generation of commercially available, amorphous silicon (a-Si) based EPIDs consist of a metal backed by a phosphor-scintillating screen optically coupled to a large-area photodiode array (Figure 2.7). Each pixel in the photodiode array consists of an optical sensor and a thin-film transistor. Several publications have established a-Si EPIDs as possessing characteristics of good dosimeters such as high resolution, linearity with dose and dose rate, and good reproducibility [44-46].

The purpose of the thin metal layer (typically 1 mm of copper) in the EPID is to convert some of the incident photons into electrons. The electrons deposit energy in the phosphor screen (typically gadolinium oxysulphide doped with terbium, Gd_2O_2S:Tb) and optical photons are produced via phosphorescence. The optical photons incident on the photodiode array, are then converted to a signal. The optical photons create electron-hole pairs in the photodiode sensor, which behaves as a capacitor for storing the imaging signal until readout of the individual pixel is performed with the thin film transistor. The process of reading out the pixels reinitializes the EPID system, with the charge collected being digitized through an analog-to-digital converter (ADC) [60].

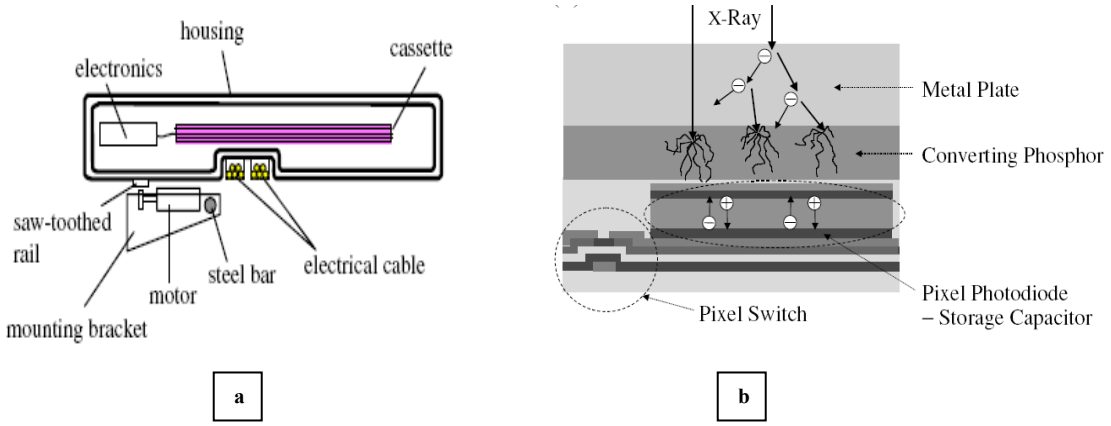


Figure 2-7: (a) Varian aS500/aS1000 imager design. (b) Pixel details including example interactions.

The aSi EPID that is used in this research project is the aS1000 (Varian Medical Systems, Palo Alto, CA), clinically available at CancerCare Manitoba. The size of the detector is 40 x 30 cm^2, containing 1024 x 768 pixels therefore defining a pixel size of 0.0392 x 0.0392 cm^2. The detector design consists of a protective epoxy front cover followed by a 2.2 cm air gap and then the imaging cassette. The imaging cassette includes a 0.1 cm thick copper buildup plate and a Lanex Fast-B phosphor screen (gadolinium oxysulphide, approximately 0.3 mm thick; Eastman Kodak Company, Rochester, NY) protected by polymethacrylimide hard foam shielding. Directly under the phosphor is the 2D array of amorphous silicon photodiodes.

Several authors have investigated the use of EPIDs for quality assurance of intensity modulated techniques via *in vivo* patient specific dose verification [61-64]. The results and conclusions of these studies indicate that EPID dosimetry will play an

increasingly important role in the radiation therapy clinic. The recent clinical introduction of VMAT techniques provides additional motivation to use EPID dosimetry to verify the accuracy of patient treatments as a function of gantry angle. Using the EPID in cine acquisition mode makes it possible to collect a series of images as a function of time (or equivalently, gantry angle, when the gantry is being rotated) during delivery. The acquired images for the numerous control points of a typical VMAT treatment can then be compared with TPS generated MLC shapes (geometrically verifying MLC position) or predicted portal images if an accurate prediction algorithm is available [65]. A method to perform Monte Carlo simulation of VMAT that includes both the patient and the EPID model would be a valuable tool for investigators working on this problem. Monte Carlo techniques provide unmatched dosimetric accuracy in many challenging situations such as the small field apertures common in VMAT, and the heterogeneous patient anatomy. The investigation of a new method that uses the Monte Carlo simulation technique to VMAT treatments, simultaneously tracking dose in both the patient geometry and a planar detector (such as the EPID or the TRD) is the subject of Chapter 5 of this thesis.

2.7 Sampling Theory and Application to Radiation Therapy Detectors

2.7.1 Sampling frequency and Nyquist frequency

The spatial distribution of incident fluence is a continuous function, but is measured by a two-dimensional grid of discrete detectors such as EPIDs, ionization chamber and diode arrays. The process in which this continuous function is sampled by

the discrete individual detectors can affect the final image (or recovered dose distribution). Specifically, if not enough information is sampled from the continuous fluence function due to detector size and spacing between individual detectors, distortions or artifacts will be introduced in the measured data [66, 67]. To accurately measure the fluence function, one needs to consider its frequency content. The image can be obtained by either sampling the data at the pixel positions or sampling the data at different positions to obtain a better result by moving the detector to increase effective resolution. Note that for *in vivo* dosimetry applications, the data is obtained by sampling the function at the fixed detector array positions. Since translating the detector array implies multiple treatment deliveries and is thus not practical for *in vivo* applications, this latter option is not considered further in this thesis. To avoid distortions or artefacts in the measured dose image, the sampling process must obey the Nyquist sampling theorem which states that the sampling (or Nyquist) frequency (f_s) should be at least twice the highest frequency (f_m) in the function being sampled i.e. $f_s \geq 2f_m$. The sampling rate or sampling frequency is defined as the number of samples obtained per unit distance in the spatial domain. The choice of sampling frequency may result in under-sampling or over-sampling of the function (Figure 2.8). Under-sampling occurs when a function is sampled at a frequency lower than half of the highest frequency (i.e. below the Nyquist frequency) in the function. Under these conditions, the measured data will not be an accurate replica of the original continuous function. This inadequate sampling is known as aliasing, and will result in the low and high frequency components in the sampled data to overlap. To avoid aliasing one should sample at a frequency higher than the Nyquist frequency. Over-sampling is the process of sampling at frequencies higher than twice the highest

frequency of the function being sampled. It is desirable because it eliminates aliasing, improves resolution, and reduces noise [66, 67].

The effect of spacing between individual detectors on a sampled function can be explained using sampling theorem in frequency domain. As stated earlier, sampling involves the measurement of a continuous function at discrete points that is equivalent to the multiplication of the continuous function and the sampling function in spatial domain. The sampling function is known as the "comb function" and is a collection of delta functions spaced by the distance between the individual detectors. The convolution theorem states that the convolution process in the spatial domain is equivalent to a multiplication in the frequency domain. Therefore, the sampling function is inversely proportional to the distance between the individual detectors in the frequency domain and represents the distance between spikes in the Fourier domain (i.e. frequency, ω). As shown in figure 2.9 a signal *I(x)* will be sampled appropriately if the spacing between individual detectors *s(x)* is small enough to avoid aliasing. However, a large distance between detectors s'(x) will result in reduced distance between delta functions and overlap of high and low frequency contents of the sampled signal in the Fourier domain (see figure 2.9). This indicates that large spacing between detectors will result in loss of information and the signal cannot be reconstructed from its samples.

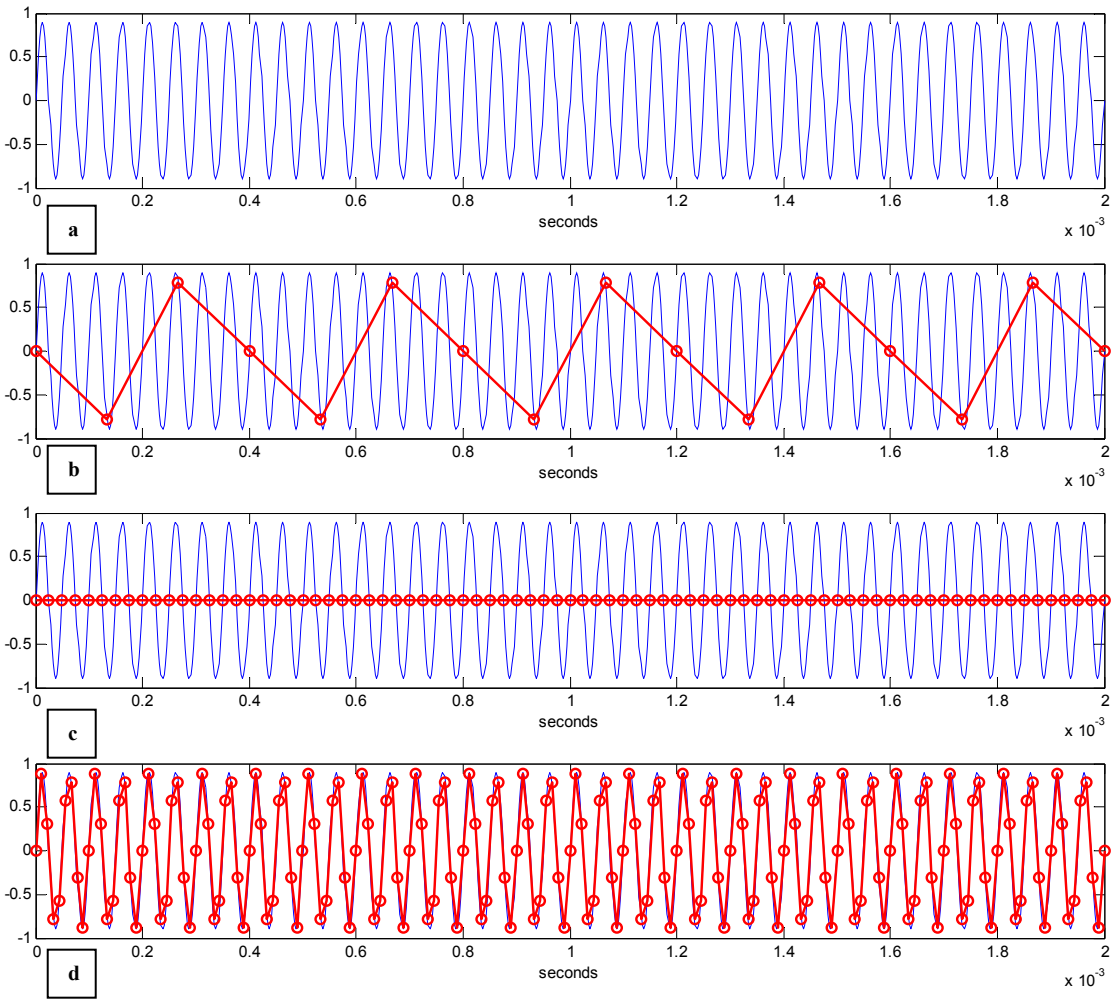


Figure 2-8: Example of aliasing (a) 20 kHz sinusoidal signal to be sampled by a digital system (b) sampling at 7.5 kHz frequency (c) sampling at 40 kHz (Nyquist) frequency (d) sampling of signal with no aliasing at 90 kHz frequency.

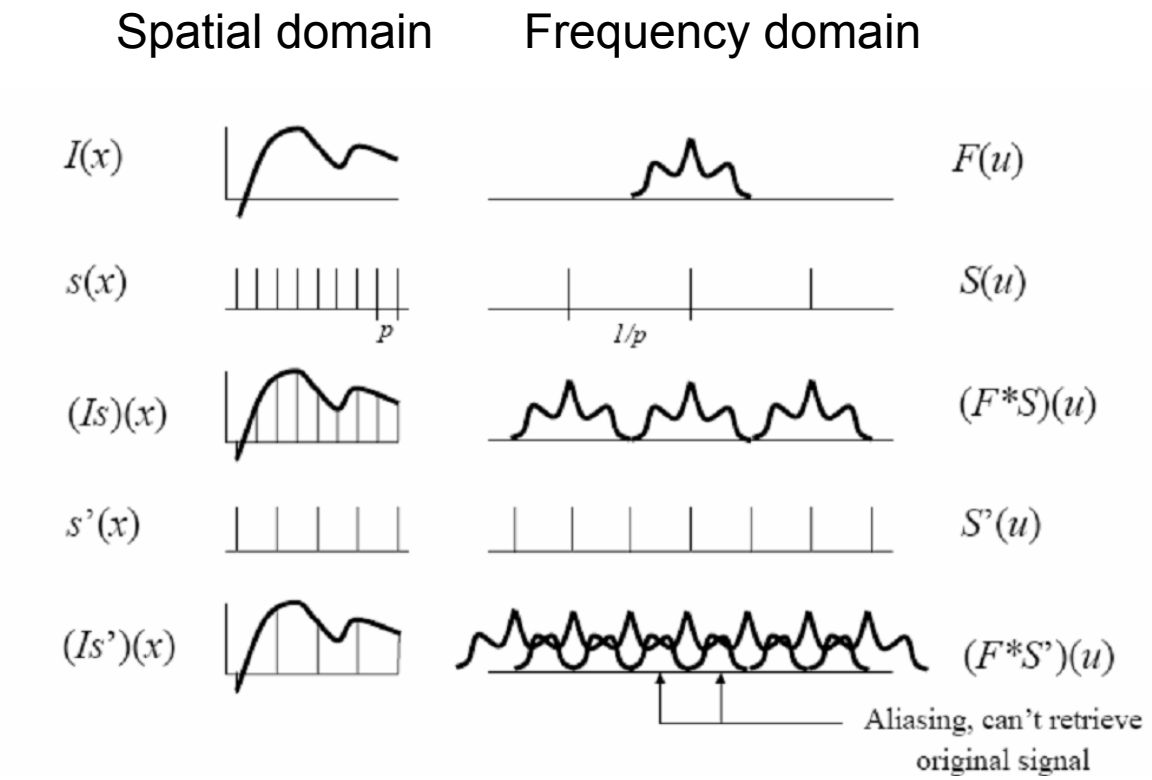


Figure 2-9: Example of effect of finite spacing between detectors on sampled signal. Large sampling distance will result in overlap of high and low frequency contents of sampled signal.

2.7.2 Spatial Resolution and Application to Radiation Therapy Detectors

The various 2D detectors that are used in radiation therapy for the measurement of incident radiation beams effectively produce an image representing the dose delivered to the detector array, and can be thought of as an imaging system. The performance of such an imaging system can be characterized by determining its spatial resolution using linear systems theory. Spatial resolution is a property that describes the ability of an

imaging system to accurately distinguish high contrast objects in close proximity in the spatial domain of the image. In lay-terms, it describes how close (spatially) two individual objects can be while being identified as two separate objects in an image. Therefore, an imaging system is said to have better spatial resolution when objects can be close together and the image still depict them as separate objects. The spatial resolution of an imaging system is characterized quantitatively by its point spread function (PSF) or line spread function (LSF) in the spatial domain and the modulation transfer function (MTF) in the frequency domain [66, 68].

The PSF describes the system response to an infinitesimally small radiation source (i.e. an incident delta-function of fluence) [68]. For a perfect imaging system, an incident delta function is exactly reproduced as a delta function in the image [68]. However, because of imperfections in the imaging system there will be some blurring of intensity around the ideal image point resulting in an un-sharp image (Figure 2.10). A common characterisation of this spatial degradation is by measurement of the PSF. The 2D image of an infinitesimally narrow delta function can be mathematically represented as a transform of two delta functions

$$\mathrm{PSF}(x,y) = \mathrm{T}\left[\delta(x)\times\delta(y)\right] \tag{2.2}$$

where T is the transformation of the point source by the system, while x and y are spatial dimensions in the image plane.

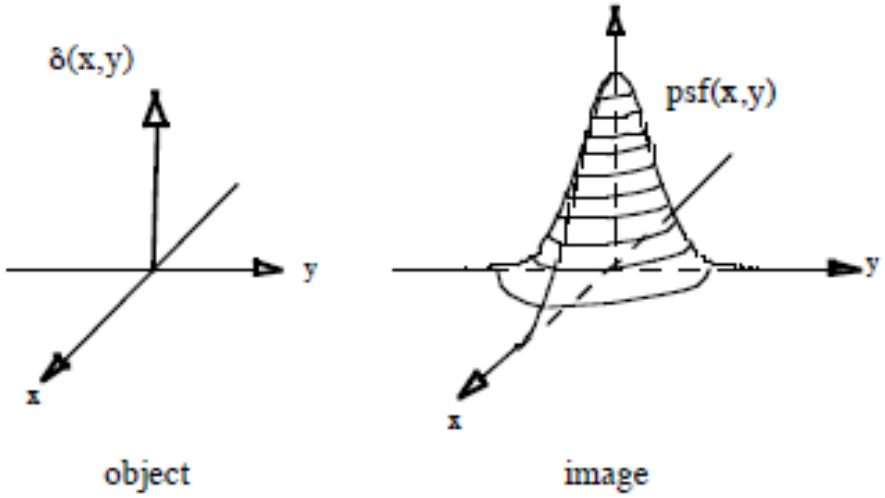


Figure 2-10: The image of a point source by non-ideal systems produces an un-sharp image.

In the frequency domain, we can derive the optical transfer function (OTF) as a two dimensional Fourier transform of the PSF(x,y) and it is represented mathematically as:

$$OTF(u,v) = FT\left[PSF(x,y)\right] \tag{2.3}$$

where u and v are the conjugate spatial frequency variables for the spatial variables (x,y). The modulation transfer function (MTF) is the magnitude of the OTF(u,v) and it is primarily used to describe the system's response in the frequency domain. More discussion on MTF will follow later in this section.

$$MTF(u,v) = \left|OTF(u,v)\right| \tag{2.4}$$

Experimental measurement of the PSF is very difficult, especially when using

megavoltage radiation sources. This is because in practice a perfect infinitesimal point object or source cannot be easily produced, but is usually approximated by collimating the incident fluence to a very tiny aperture using a material with a high atomic number such as tungsten or lead [68]. Very few photons from the radiation source would be transmitted through the small aperture, usually resulting in lengthy exposure times. In addition, misalignment of the aperture with the source and the detector may cause inaccurate measurement of the PSF. To overcome some of these experimental problems, the point spread function can be mathematically derived from the line spread function (LSF), described below, which can be measured more easily.

The line spread function represents the response of a system to an incident source which is infinitely thin, long, and of uniform intensity [68]. Similar to the PSF, imperfections in imaging systems will result in the blurring of the image of an ideal line source (Figure 2.11). The LSF is a one-dimensional representation of the two dimensional point spread function and can be obtained mathematically from the line source represented as:

$$\text{line}(x) = \delta(x) = \int_{-\infty}^{+\infty} \delta(x)\delta(y)dy \tag{2.5}$$

where in this representation the line is infinitely narrow in the x-direction and extends infinitely in the y-direction. Assuming T is the transformation of the line source by the imaging system then the LSF can be represented as:

$$\text{LSF}(x) = T\left[\text{line}(x)\right] = \int_{-\infty}^{+\infty} T\left[\delta(x)\delta(y)\right]dy = \int_{-\infty}^{+\infty} \left[\text{PSF}(x,y)\right] dy \tag{2.6}$$

As shown in equation(2.6), the LSF can be thought of as the integral across y of the PSF.

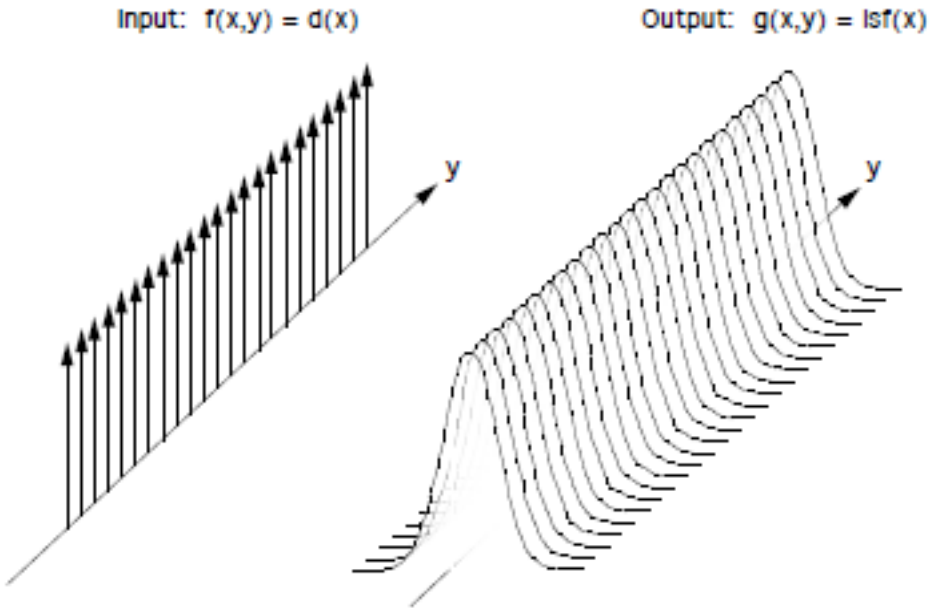


Figure 2-11: The line spread function (LSF) is the image of a line source.

Assuming radial symmetry the modulus of the Fourier transform of the normalized LSF is the MTF of the system and mathematically is represented as:

$$FT\left[LSF(x)\right] = \int_{-\infty}^{+\infty} LSF(x)\, e^{-2\pi iux} dx = \int_{-\infty}^{+\infty} \left[\int_{-\infty}^{+\infty} PSF(x,y)\, dy \right] e^{-2\pi iux} dx \qquad (2.7)$$

$$\int_{-\infty}^{+\infty}\int_{-\infty}^{+\infty} PSF(x,y)\, e^{-2\pi i(ux+0y)} dxdy = FT\left[PSF(x,y)\right]_{v=0} = OTF(u,0) \qquad (2.8)$$

From equation(2.8), the MTF can be derived by taking the modulus of the OTF

(u,0) as previously explained in this section (equation 2.3). For an imaging system a more narrow LSF indicates higher resolution as estimated by the MTF, i.e. it is better able to reproduce details of the source function compared to broader LSF curves (Figure 2.12).

For a perfect imaging system, when an intensity distribution such as a photon beam is transmitted through an object, the output (image) will have the same spatial frequency as the incident distribution. However, due to imperfections in the imaging systems the amplitude of the frequencies in the imaged distribution will be reduced. In real imaging systems, the higher frequency content is preferentially reduced in the image distribution. This is an indication of a loss of resolution. The modulation transfer function (MTF) is a measure of how well the frequencies in the intensity distribution are reproduced in the image [66-68]. It is a metric widely used to characterize the spatial resolution properties of an imaging system and is obtained via the MTF curve in which the amplitude of the distribution is plotted against spatial frequency (Figure 2.12).

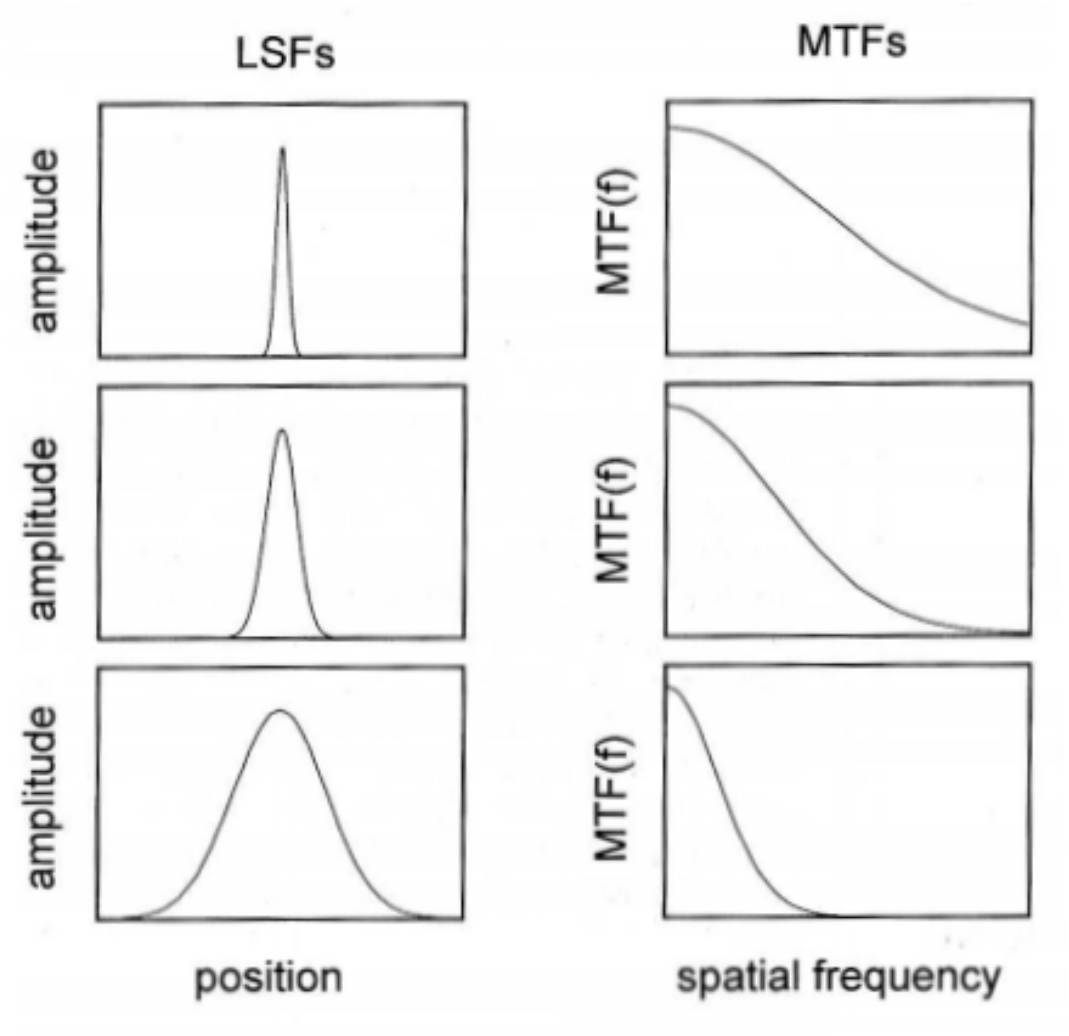


Figure 2-12: The modulation transfer function (MTF) is the modulus of the Fourier transform of the LSF. It is used to characterize the spatial resolution of an imaging system.

Due to the presence of steep dose gradients (high frequency) between normal tissue structures and target volumes in IMRT and VMAT, a detector with high spatial resolution is required for dose verification of the modulated fluence. The spatial resolution of a multi-element detector is limited by the (1) spacing between, and (2) size

of individual detector elements [41]. A large detector element size will result in poor resolution and a large spacing may result in lost information. Due to the finite size of detectors used for measurement, the discretely sampled measured fluence may not exactly represent the actual delivered fluence (i.e. a continuous function). This phenomenon is called the detector size effect and is a major perturbation in ionization chamber array dosimetry [69, 70]. The detector size effect is reduced in arrays using detector elements with smaller sizes such as diodes (~ 0.7-2 mm), film (microscopic, although film is typically digitized at 0.1 mm), and EPIDs (~0.4 mm). However, if the detector element size is uniform across the entire detector array, the measured fluence $F_m(x,y)$, may be represented as a convolution of the true continuous fluence with the response function of the detector element:

$$F_m(x,y) = F_a(x,y) * R(x,y) \tag{2.9}$$

where $F_a(x,y)$ is the 2D actual fluence delivered by the radiation treatment machine, and $R(x,y)$ is the 2D detector response function. The transmission detector studied in chapters three and four performs a 2D measurement of dose as converted from the sampled incident fluence $F_m(x,y)$.

To accurately sample the delivered dose distribution, the sampling frequency (i.e. sample spacing) of a detector system must obey the Nyquist sampling theorem in order to prevent loss of information [41, 68]. If the distribution contains frequencies greater than the Nyquist frequency, the distribution will be under-sampled and artefacts will be introduced into the measurement as explained earlier.

2.8 Use of Monte Carlo Technique in Radiation Therapy

The Monte Carlo technique is a powerful tool for simulating radiation transport in matter for radiation therapy applications [71]. It is a method for approximately solving mathematical problems by the simulation of random variables. The technique uses the knowledge of probability distributions governing the different photon-atom and electron-atom interactions in materials to simulate random trajectories or histories of individual particles in the geometry [72]. The probability distributions are sampled randomly in order to reduce systematic errors in this technique to solve radiation transport problems. When one keeps track of a large number of such histories, it provides information about specific physical quantities and related distributions of interest such as fluence, energy fluence, angular distribution, dose distribution, detector response, etc. The statistical uncertainty of the calculation result is proportional to the inverse square root of the number of incident particles used in the simulation (typically termed as histories, N), or $N^{-½}$ [72]. For realistic radiotherapy simulations, the simulation time can be very long depending on the desired accuracy and/or the complexity and size of the geometry. However, simulation times are constantly decreasing due to the decrease in the cost of computing power and data processing in recent times, as well as the development of variance reduction techniques (methods that reduce simulation time to produce an answer without noticeable loss of accuracy) and parallel computing options[73]. The technique is widely accepted and used for a variety of radiotherapy applications [74-76]. These include examples such as calculation of stopping power ratios used in radiation dosimetry, determination of photon spectra from sources, radiation detector response

simulations, determination of dose kernels in water (used in some model-based TPSs), as an independent dose calculation system, and optimization of portal imaging devices. The main advantages of using the Monte Carlo technique are its high accuracy in estimating various quantities of interest, and its ability to provide information that cannot be easily measured experimentally. The Monte Carlo codes that are commonly used for simulations of radiation transport in medical applications are EGSnrc/BEAMnrc, MCNP5, PENELOPE, and GEANT5. All these codes are written in the FORTRAN programming language except GEANT5 which is written in the C++ language [71].

2.8.1 The EGSnrc Monte Carlo System

All the Monte Carlo simulations in this work were performed using the EGSnrc Monte Carlo code [77], developed and distributed by the National Research Council (NRC) of Canada. It is an improved version of the EGS4 package [78] originally developed at the Stanford Linear Accelerator Center (SLAC). The EGSnrc package has several subroutines written in the MORTRAN3 language (a FORTRAN pre-processor) with a flexible user interface, which does not require one to be very familiar with the internal details of the code. In addition, it allows advanced users the possibility of editing user codes to create specific applications, without affecting the accuracy of the underlying radiation transport physics. The EGSnrc code is the hub of this radiation transport software, using its multiple routines for random number generation, calculation of particle path length, different processes governing particle interactions, particle tracking, etc., all required for radiation transport. However, the system also includes

many codes developed to perform specific tasks, such as BEAMnrc (used for simulation of the complex components of the head of medical linear accelerators), DOSXYZnrc (used for dose calculation in phantom or patient models based on CT data sets), CAVRZ (used for calculation of ion chamber response), BEAMDP (used for phase-space analysis), and others. BEAMnrc and DOSXYZnrc are the two most commonly used well-validated user codes and detailed discussions on their use and features are provided in section 2.8.1.1 and section 2.8.1.2 respectively. An illustration of a schematic of the typical geometries simulated in a linear accelerator treatment head (using BEAMnrc) and the resulting radiation transport through a patient CT data set is shown in figure 2.13.

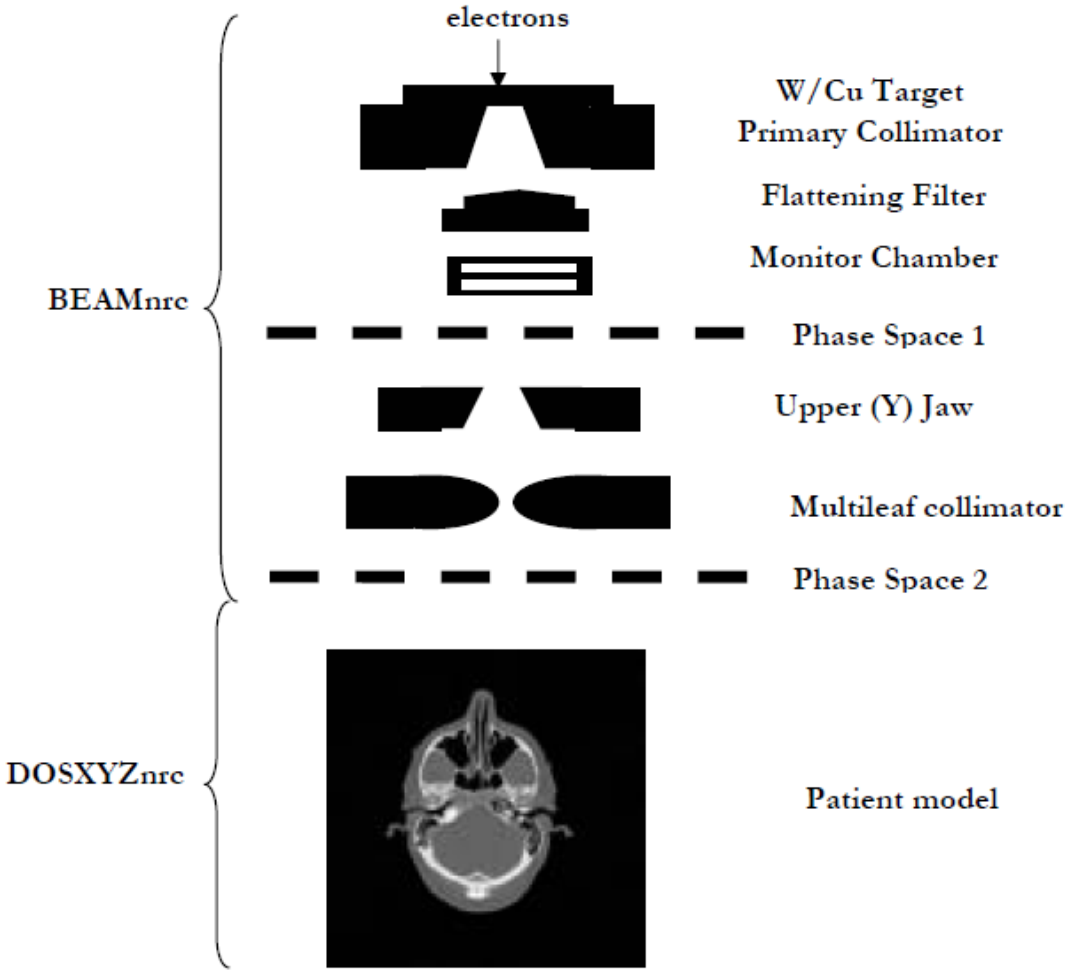


Figure 2-13: Illustration of the Linac head simulation in BEAMnrc and dose calculation in DOXYZnrc.

The EGSnrc code simulates a number of photon interactions and electron/positron interactions in the energy range of 1 keV to 10 GeV. Photon interactions include photoelectric absorption and photoelectron production, Compton scattering from atomic electrons (incoherent scattering), pair production, and Rayleigh scattering from the atom.

Electron and positron interactions include bremsstrahlung photon creation in the nuclear and atomic fields, positron annihilation with atomic electrons, multiple scattering of electrons and positrons by atomic electrons, excitation of atoms and molecules, and creation of knock-on electrons. Knock-on electrons are electrons that are ejected from an atom due to an inelastic collision with an incident electron or positron [77].

Due to the large number ($\sim 10^6$) of elastic and inelastic collisions that an electron undergoes during its history until it is absorbed, specialized electron transport algorithms based on the condensed history technique (CHT) have been developed [79]. In the CHT algorithm, a large number of individual interactions occurring along the path of an electron are grouped together and the transport is handled in a series of steps. This saves a significant amount of time that would have been spent in simulating each individual collision. These CHT transport algorithms are used by all Monte Carlo codes and are classified into two broad categories, class I and class II. The main difference between them is how the individual events that lead to bremsstrahlung photons and /or knock-on electrons are treated [72]. In class I algorithms, the effects of all individual events of a certain type on the primary electron are grouped together for each condensed history step. Also, the creation of individual secondary particles does not affect either the energy or direction of the primary electron. In class II algorithms, the effects of only a subset of the individual events of each type are grouped together while the effects of the remaining interactions are treated individually. It is well known that the class II algorithms are more accurate than class I because of the inclusion of correlation between primary and secondary particles. Both class I and class II algorithms use ‘energy cutoffs’, but

'production thresholds' apply only to class II algorithms. Energy cutoffs are kinetic energies below which particle histories are terminated (i.e. all remaining kinetic energy is deposited locally and the particle is removed from the simulation), and are generally user-defined. Production thresholds are defined as kinetic energy values above which all secondary particles are simulated. EGSnrc uses a class II algorithm and requires users to specify both energy cutoffs and production thresholds. The choice of energy cutoffs are based on efficiency and desired accuracy of the simulation. Selection of high energy cutoffs will results in faster simulation times at the expense of accuracy. In EGSnrc, electron transport cutoff energy (ECUT) of 0.700 MeV and photon transport cutoff energy (PCUT) of 0.01 MeV are commonly used for radiotherapy applications to achieve an acceptable tradeoff between efficient and accurate simulations. In addition, an electron production threshold (AE) of 0.521 MeV and a photon production threshold (AP) of 0.01 MeV are commonly used. The EGSnrc code offers significant improvements in radiation transport accuracy compared to the original EGS4 code, including the use of a new 'any-angle' multiple scattering theory for electron scattering, improved electron step algorithm, and addition of an exact boundary crossing algorithm [80].

All versions of EGS have a standalone utility program called PEGS4 (Preprocessor for EGS) which creates the cross-section data required for the code to simulate the interactions within various materials, defined by atomic composition and density. The program determines the cross-section data for elements theoretically, while cross-section data for compounds and mixtures of elements are created through weighted combinations of cross-sections of the constituent elements.

2.8.1.1 Simulation of particle transport in EGSnrc Monte Carlo code

The simulation of particle transport in EGSnrc Monte Carlo code consists of four main stages [73]:

1. Sample the distance to the next interaction
2. Transport a particle to the interaction site considering the geometry
3. Select the interaction type
4. Simulate the selected interaction

The following processes are performed repeatedly until the original particles and all secondary particles leave the geometry or are absorbed (ie. locally depositing their energy if it is less than the defined energy cutoffs). In the first stage, the probability that a particle will interact in an interval *dr* at a distance *r* relative to the initial particle position is:

$$p(r)dr = e^{-\mu r}\mu dr \tag{2.10}$$

Where μ is the linear attenuation coefficient (number of interaction per unit length). The inverse transform method is then used to sample the distance *r* according to *p*(*r*). It equates the cumulative probability of *p*(*r*) with a random number ξ that is uniformly distributed between zero and one.

$$\int_0^r p(r')dr' = \xi \Rightarrow r = -\frac{\ln(1-\xi)}{\mu} \tag{2.11}$$

The selection of a random number in Monte Carlo simulation applications needs to be truly random and is in fact an active field of research devoted to developing algorithms to

generate sequences of "true" random numbers. In the second stage, the particle is transported to the interaction site through a basic ray-tracing step. It takes into account the medium and mass density of the geometry model in the defined region but also considers the distance to the next geometry boundary along the particle trajectory. The type of radiation interaction that will occur is selected in the third stage using a probability distribution function similar to that described in stage one. However, it involves defined discrete final states that correspond to a particular interaction type. For example, the cross section for an interaction type *i* is denoted by σ_i and the total cross section is $\sigma = \sum \sigma_i$ for all n interaction types. The probability that interaction 1 will occur is $\xi \le \sigma_1 / \sigma$, else interaction 2 if $\xi \le (\sigma_1 + \sigma_2)/\sigma$, else interaction n if $\xi \le (\sigma_1 + \sigma_2 + ... + \sigma_n)/\sigma$. In the final stage, the energy/direction of resultant particles are sampled from the differential cross section of the selected interaction type. It then score or keeps track of their parameters for future processing. The EGSnrc manual [77] provides additional information on methods used for appropriate photon interactions.

2.8.1.2 Accuracy of EGSnrc Monte Carlo code

The stochastic nature of the Monte Carlo method introduces statistical uncertainties into the results. In EGSnrc estimates of the statistical uncertainties are obtained using the batch method because of its conceptual and numerical simplicity. In the batch method, the simulation is divided into n independent batches, each processing the same number of histories. The estimate of uncertainty (i.e. variance of the mean, $s_{\bar{x}}$)

of a scored quantity, X is given by:

$$s_{\bar{x}} = \sqrt{\frac{\sum_{i=1}^{n}\left(X_i - \bar{X}\right)^2}{n(n-1)}} \tag{2.12}$$

where X_i is the scored quantity such as energy fluence in batch i, and $\bar{X}$ is the mean value of X over all the batches. The main disadvantage of this method is that statistical fluctuation in the uncertainty estimate may exist because of the small number of batches (typically 10) [73].

For over thirty years, the EGSnrc code has been validated, benchmarked, and used for different medical physics applications, but small systematic errors may still be present in the code. In general for Monte Carlo simulation software, common sources of systematic errors include programming errors, round off and truncation errors, modelling inaccuracies, and errors in photon cross section data. The extensive use of the EGSnrc code and the frequent revision to the code by the development group minimize the probability of significant programming errors. Roundoff and truncation errors may occur due to the finite precision of real numbers within the computer. This is typically associated with a roundoff or truncation of small values in accumulation variables. Again, the widely use of the EGSnrc code and good coding practice employed reduce the effect of this error. Modelling inaccuracies due to certain simplifying assumptions made in the modeling of the underlying physical processes may introduce systematic errors in EGSnrc simulations. Errors in photon cross section data are likely the most important limiting systematic error, because any error in the data will be transferred to the result

through the random sampling process. Currently this error depends on both the source of cross section data and the type of photon interaction. For example, the photoelectric effect cross sectional data may have a 3-5% uncertainty, while Compton scattering may have 2-3% uncertainty for high Z materials and <1% uncertainty for low Z materials, while pair production is about a 5% uncertainty. In the work in this thesis, the photon interactions are dominated by the Compton effect and are mostly dealing with lower Z materials, and thus the expected systematic error in Monte Carlo simulation results is estimated to be in the 1% range.

2.8.1.3 BEAMnrc user code

The BEAMnrc user code available with the EGSnrc Monte Carlo system was developed for modelling of the complex geometries encountered in radiation treatment units [81, 82]. The code provides a user interface to allow the user to build a customized linear accelerator head from a series of component modules. This makes the code very flexible in that complex head models can be simulated using several building blocks of different materials and geometries. One advantage of this approach is that individual component modules can be tested and debugged, significantly improving the reliability of the results. The code comes with a graphical user interface, which allows the creation of input files and visualization of the customized linear accelerator. The BEAMnrc code does not score dose in the simulation, but rather it creates a "phase-space" file (i.e. output file) at an arbitrary, user-defined plane in the simulation. The phase-space file contains detailed information about all particles crossing the plane, including the particle charge,

energy, position, direction, weight, and LATCH. The LATCH variable option allows for tagging particles based on the interactions they undergo and/or the location of the interactions. The advantage of using the LATCH tracking option is that one can obtain valuable information about the physics of the radiation beam that is not available through measurement, such as the relative dose contribution from various treatment head components, and it is also invaluable to the construction of head source models [83].

The BEAMnrc code has been used extensively in the simulation of the head of different radiotherapy units for studies such as photon and electron beam characteristics [84], calculation of surface doses [85-87], prediction of EPID response [88], and ion chamber dosimetry [89]. It is also a great teaching aid to help scientists understand the physics of radiotherapy beams and the role of different head components in shaping the final properties of the treatment beam. The BEAMnrc website (http://irs.inms.nrc.ca/software/beamnrc/) contains articles, reports, and conference presentations that provide additional descriptions of the system and serve as valuable resources for both new and advanced users.

2.8.1.4 DOSXYZnrc user code

DOSXYZnrc is an EGSnrc user-code developed for three-dimensional dose calculations. It simulates the transport of photons and electrons/positrons in Cartesian coordinates and scores the energy deposition in the designated voxels [90]. A voxel is simply a sub-volume of the total simulation volume. The code has a graphical user

interface which allows input files to be created and executed. The geometry is a rectilinear volume with voxel dimensions that are variable in all three directions. Each voxel can be assigned different materials and/or varying densities (e.g. for use with CT data). The code allows a variety of radiation source options, such as diverging or parallel beams, circular, rectangular, or arbitrarily shaped beams, monoenergetic or polyenergetic energies, and can also use phase-space files generated by BEAMnrc simulations. The variety of source options are represented as ISOURCE inputs in the software (e.g. ISOURCE=1 is a simple isotropic point source). Recently two new sources, ISOURCE 20 and 21 have been added to perform VMAT simulation and dose calculation. These two sources support continuously rotating gantry and collimator, dynamic MLC motion, variable dose rate, as well as couch rotation and translation of the couch in any direction. DOSXYZnrc has a variety of features such as dose component calculations, a number of source configurations, CT to phantom conversion (via `ctcreate`), simulation restart capabilities, phase-space redistribution, and more. This user code is flexible enough to simulate many different situations, but comes with a simple graphical user interface so that basic users do not need to possess a detailed understanding of the MORTAN programming language.

2.9 Monte Carlo Dose Calculation Methods for Complex Treatment Delivery Techniques

Often in radiation therapy the patient dose calculation process is separated into two steps: (1) determination of radiation beam fluence incident upon the patient or

phantom and (2) determination of the dose deposition to the patient or phantom, resulting from that incident energy fluence [73]. These two steps may be performed using Monte Carlo methods. For the EGSnrc system, the first step can be done using BEAMnrc to obtain a phase-space file incident on the patient or phantom, and the second step can be performed using the phase-space file as a radiation source for the DOSXYZnrc code. Alternatively, the entire simulation and patient dose calculation may be performed in a single simulation in DOSXYZnrc without the need for a phase-space file by synchronizing the treatment head simulation in BEAMnrc with the dose calculation [91].

A key element of the Monte Carlo simulation methods for IMRT and VMAT techniques is the simulation of incident fluence through a model of the MLC. Due to the complex shape of the MLC leaves, especially the MLC leaf tips, it is very important to accurately model the MLC to ensure accurate patient dose evaluation [92]. In the EGSnrc system, several different component modules for various MLC designs have been written for BEAMnrc, and their names and features are listed in Table 2.1. A full Monte Carlo simulation through the MLC of all beam segments of an IMRT delivery would take tens or hundreds of hours to be performed on a single CPU. For routine clinical use this will be a significant limitation in the application of such modules for IMRT optimization or plan verification. However, independent customized Monte Carlo MLC modules have been developed specifically to reduce the overall radiation transport time through the MLC without introducing clinically unacceptable bias into the simulation result [93, 94]. An independent Monte Carlo MLC model developed by Siebers *et al* simplifies the problem by not including electron transport within the MLC, including only the first

Compton events in the MLC scatter radiation, and simplifying the transport through the complex MLC geometry for highly divergent particles that may miss the patient plane [94]. These simplifications result in speed increases of several hundred-fold compared to more general purpose codes such as BEAMnrc or DOSXYZnrc, without introducing significant bias into the patient dose computation.

Table 2-1: Multi-leaf collimator (MLC) component modules developed in BEAMnrc

Component Modules	Features
MLC	Models a generic double-focused MLC with flat faces but does not model the tongue-and-groove effect
MLCQ	Models a single-focused MLC that has rounded leaf ends but does not model the tongue-and-groove
VARMLC	Models a single-focused MLC that has rounded leaf ends with a tongue-and-groove design similar to a 80-leaf Varian MLC.
DYNVMLC	Models a 120-leaf Varian Millennium MLC with tongue-and-groove and supports dynamic MLC motion.
MLCE	Models Elekta MLCs, including their tongue-and-groove design.

A significant advantage of using Monte Carlo dose-computation algorithms is their ability to accurately calculate dose for fluence patterns in complex geometries without making assumptions regarding radiation equilibrium conditions [73]. It has been shown that Monte Carlo algorithms can accurately compute dose for small field sizes and heterogeneous geometries such as those found in head-and-neck and lung patients [95, 96]. In general, the Monte Carlo technique is a well-established method for solving radiation transport problems in complex situations such as linear accelerator treatment heads and heterogeneous patients. It is often considered as the "gold standard" for

accurate dose calculation [73] and has been used in this role throughout this thesis.

2.10 Dosimetric Evaluation of Measured and Calculated Dose Distributions

Traditionally, dose verification tests that compare measured and calculated dose distributions use overlays of dose profiles or isodose distributions (i.e. contours of equal dose on a 2D display). However, for quantitative evaluation of both 2D dose profiles and 3D dose distributions, advanced techniques that use a combination of percentage dose difference and distance-to-agreement (DTA) metrics have been developed [97, 98]. Clinical dose distributions, even those created with simple non-modulated beams, consist of various regions of high and low dose, as well as high and low dose gradients. To address this issue, Van Dyk *et al* suggested that for comparisons, dose distributions should be subdivided into regions of low dose gradient (less than 30%/cm) and high dose gradient (greater than 30%/cm) each with different acceptance criteria [99]. A percentage dose difference criterion is applied in regions of relatively low dose gradient because a dose difference map will easily reveal where calculated and measured distributions disagree. For high dose gradient regions, a small spatial displacement in the calculated distribution relative to the measured distribution will result in a large dose difference if percentage dose difference only is used. Thus the use of dose difference only may not be a sufficient comparison metric but a distance to agreement is a more meaningful parameter. Therefore, a combination of dose difference and distance-to-agreement comparison is often applied to determine the accuracy of the calculated dose distribution.

In radiation therapy, the most frequently used quantitative analysis that accomplishes a combined dose difference and distance-to-agreement comparison is termed the ‘gamma method’. It combines a comparison of percentage dose differences and distance-to-agreement between reference and evaluated dose distributions, into a single parameter termed the gamma value [98]. The distance-to-agreement metric defined for a given reference dose is the maximum spatial distance within which a point in the comparison data set has to be found that receives the same dose. When using the gamma method to compare two dose distributions, a distribution of gamma values is returned in which gamma > 1 indicates the comparison point lies outside the defined tolerances and a gamma < 1 indicates the comparison point lies within the defined tolerances (Figure 2.14).

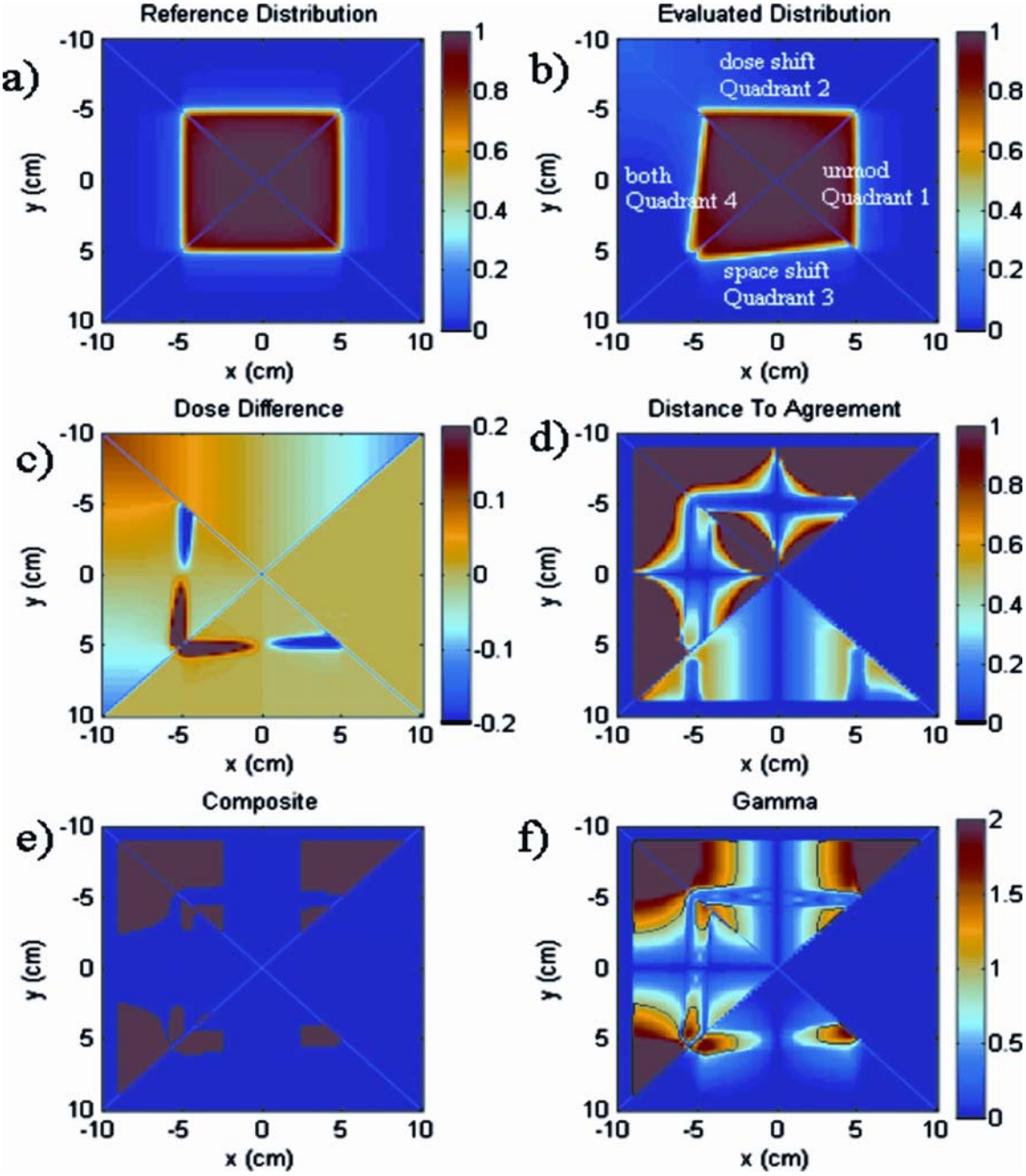


Figure 2-14: Example of gamma test for a 10 x 10 cm^2 field showing (a) reference distribution (b) modified evaluated distribution (c) dose difference analysis shows differences in dose between both distributions (d) distance to agreement analysis

shows differences in DTA between the quadrants of both distributions (e) composite distribution shows regions that passed either or both the DD or DTA (f) gamma distribution for 3% and 3 mm criteria.

The chi (χ) comparison method [100] is conceptually a nearly identical concept to the gamma method, but is mathematically more efficient and offers the additional advantage of preserving the sign of the comparison (i.e. positive or negative indicating an under or over estimate). Other quantitative evaluation methods such as the χ^2 confidence method, the normalized agreement tests, and the dose gradient compensation method have been suggested in the literature [101]. For complex techniques (i.e. IMRT and VMAT) where pre-treatment verification is commonly performed, gamma evaluation criteria of a 3% dose difference (DD) and 3 mm distance to agreement (DTA) are often used, typically expecting a minimum portion of comparison points of around 90-95% to lie within this tolerance. Locally at CancerCare Manitoba, a tolerance of 3%/3mm is used clinically, and the current pass/fail tolerance for measurement-based QA using film media (planar) as well as 3D dose reconstruction (via MatriXX measurement) is set at 95% of points in the high dose region with $\gamma \leq 1$. The gamma method returns a single value of gamma per comparison point so 2D gamma comparisons can be viewed as a 2D image and 3D gamma comparisons can be viewed as a volumetric data set. These data sets represent the pass or fail of pixels or voxels for a given set of tolerances. Although the gamma method is currently the most widely used metric for dose comparisons, it has several limitations including insensitivity to clinically relevant patient dose errors [102].

Nelms *et al* [102] showed that treatment plans with wrong MLC positions were found to have about 95% gamma passing rates but dose volume histograms (DVH) of the same plans showed significant errors. Another limitation of the tool is the presence of noise in the evaluated dose distribution, which results in the underestimation of the gamma comparison (i.e. masks a poor comparison). Investigations by Low and Dempsey [98] on the effect of noise showed that, in regions where the reference and evaluated dose distributions differ by about 3%, a 1% standard deviation noise in evaluated distribution reduced the average gamma value from 1.0 to 0.5. However, when the noise was added to the reference distribution the average value of gamma was accurately calculated an indication that the selection of the reference or evaluated distribution should consider this. In addition, the choice of 3%/3 mm criteria, although extremely common in the medical physics community, has not been justified through rigorous scientific studies but rather is based on anecdotal results from several institutions [103].

The gamma index mathematics are briefly described here. Defining D_m to be the dose measured at position r_m, D_c the calculated dose at position r_c relative to the measurement point r_m, ΔD_m the percentage dose tolerance criterion, and Δd_m the distance-to-agreement tolerance criterion, then the gamma value for the measurement point r_m is defined as:

$$\gamma\left(r_m\right) = \min\left\{\Gamma\left(r_m, r_c\right)\right\} \forall \left\{r_c\right\} \tag{2.13}$$

$$\Gamma\left(r_m, r_c\right) = \sqrt{\frac{r^2\left(r_m, r_c\right)}{\Delta d_M^2} + \frac{\delta^2\left(r_m, r_c\right)}{\Delta D_M^2}} \tag{2.14}$$

$$r\left(r_m, r_c\right) = \left|r_c - r_m\right| \text{ and } \delta\left(r_m, r_c\right) = D_c\left(r_c\right) - D_m\left(r_m\right) \tag{2.15}$$

The pass/fail criteria are:

$\gamma\left(r_m\right) \le 1$ Calculation passes

$\gamma\left(r_m\right) > 1$ Calculation fails

The dosimetric evaluations of dose distributions in this thesis were performed using both gamma evaluation and χ-comparison. The χ-comparison is a fast and computationally efficient implementation of the gamma evaluation concept. The χ approach also works in either two or three dimensions and applies a percentage dose difference and a distance –to-agreement tolerance, in the form of a gradient-weighted dose difference described mathematically below [100]:

$$\chi = \frac{D_c(\vec{r}) - D_r(\vec{r})}{\sqrt{\Delta D_{\max}^2 + \Delta d_{\max}^2 . \left\|\nabla D_r\right\|^2}} \tag{2.16}$$

where D_c is the compared dose (e.g. measured dose) and D_r is the reference dose (e.g. calculated dose), while ΔD_{max} and Δd_{max} are the percentage dose tolerance criterion and the distance-to-agreement tolerance criterion respectively. ∇D_r is dose gradient of the reference dataset.

Similar to the gamma methods, the pass/fail criteria are:

$\chi\left(r_c\right) \le 1$ Calculation passes

$\chi\left(r_c\right) > 1$ Calculation fails

Unlike the gamma methods, the χ-comparison uses the dose gradient of the reference dataset to define an "acceptance tube" around the reference points then evaluates dose differences at pairs of points in the two dose distributions to be compared and does not require a search for the distance to the closest agreement (Figure 2.15). Some of the advantages of the χ-comparison method over the gamma method include increased computational efficiency, and the ability to classify dose difference observed as under-prediction or over-prediction that is not possible using the gamma method. For IMRT and VMAT dose verification in this thesis, the χ comparison method is used typically with a 3% dose difference and 3 mm distance-to-agreement criteria.

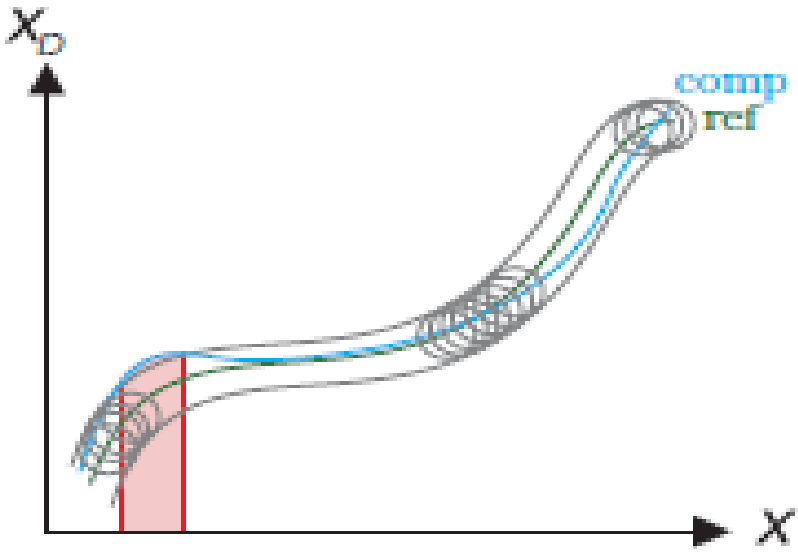


Figure 2-15: Acceptance tube defining the dose gradient of the reference dataset around the reference points for comparison of both dose distributions.

2.11 Bibliography

1. Metcalfe, P., T. Kron, and P. Hoban, *The physics of radiotherapy X-rays and electrons*. 2007: Medical Physics Publishing.
2. Nahum, A.E. and J.C. Rosenwald, *Handbook of radiotherapy physics: theory and practice*. 2007: Taylor & Francis Group.
3. Khan, F.M. and S. Stathakis, *The physics of radiation therapy.* Med Phys, 2010. **37**: p. 1374.
4. Nutting, C., D.P. Dearnaley, and S. Webb, *Intensity modulated radiation therapy: a clinical review.* Br J Radiol, 2000. **73**(869): p. 459-69.
5. Otto, K., *Volumetric modulated arc therapy: IMRT in a single gantry arc.* Med Phys, 2008. **35**: p. 310.
6. Palma, D., et al., *Volumetric modulated arc therapy for delivery of prostate radiotherapy: comparison with intensity-modulated radiotherapy and three-dimensional conformal radiotherapy.* Int J Radiat Oncol Biol Phys, 2008. **72**(4): p. 996-1001.
7. Zhang, P., et al., *Volumetric modulated arc therapy: planning and evaluation for prostate cancer cases.* Int J Radiat Oncol Biol Phys, 2010. **76**(5): p. 1456-62.
8. Ezzell, G.A., et al., *Guidance document on delivery, treatment planning, and clinical implementation of IMRT: Report of the IMRT subcommittee of the AAPM radiation therapy committee.* Med Phys, 2003. **30**: p. 2089.
9. Verbakel, W.F., et al., *Volumetric intensity-modulated arc therapy vs. conventional IMRT in head-and-neck cancer: a comparative planning and*

dosimetric study. Int J Radiat Oncol Biol Phys, 2009. **74**(1): p. 252-9.

10. Bortfeld, T., *IMRT: a review and preview.* Phys Med Biol, 2006. **51**: p. R363.
11. Velec, M., et al., *Cone-beam CT assessment of interfraction and intrafraction setup error of two head-and-neck cancer thermoplastic masks.* Int J Radiat Oncol Biol Phys, 2010. **76**(3): p. 949-55.
12. Mijnheer, B. and D. Georg, *Guidelines for the verification of IMRT.* Estro booklet No, 2008. **9**.
13. Low, D.A., et al., *Dosimetry tools and techniques for IMRT.* Med Phys, 2011. **38**(3): p. 1313-1338.
14. Ismail, A., et al., *Radiotherapy quality assurance by individualized in vivo dosimetry: state of the art.* Cancer Radiother, 2009. **13**(3): p. 182-9.
15. Chen, J., et al., *Calibration of an amorphous-silicon flat panel portal imager for exit-beam dosimetry.* Med Phys, 2006. **33**(3): p. 584-94.
16. Bucciolini, M., F.B. Buonamici, and M. Casati, *Verification of IMRT fields by film dosimetry.* Med Phys, 2004. **31**(1): p. 161-8.
17. Low, D.A., et al., *Quantitative dosimetric verification of an IMRT planning and delivery system.* Radiother Oncol, 1998. **49**(3): p. 305-16.
18. Jursinic, P.A., *Implementation of an in vivo diode dosimetry program and changes in diode characteristics over a 4-year clinical history.* Med Phys, 2001. **28**(8): p. 1718-26.
19. Quach, K.Y., et al., *Measurement of radiotherapy x-ray skin dose on a chest wall phantom.* Med Phys, 2000. **27**(7): p. 1676-80.
20. Leunens, G., et al., *Quality assurance in radiotherapy by in vivo dosimetry. 1.*

Entrance dose measurements, a reliable procedure. Radiother Oncol, 1990. **17**(2): p. 141-51.

21. Leunens, G., et al., *Quality assurance in radiotherapy by in vivo dosimetry. 2. Determination of the target absorbed dose.* Radiother Oncol, 1990. **19**(1): p. 73-87.

22. Kutcher, G.J., et al., *Comprehensive QA for radiation oncology: Report of AAPM Radiation Therapy Committee Task Group 40.* Med Phys, 1994. **21**(4): p. 581-618.

23. ICRU, *Determination of absorbed dose in a patient irradiated by beams of X or gamma rays in radiotherapy procedures*. ICRU Report 24. 1976, Bethesda, Maryland.

24. *Procedures in external radiation therapy dosimetry with electron and photon beams with maximum energies between 1 and 50 MeV. Recommendations by the Nordic Association of Clinical Physics (NACP).* Acta Radiol Oncol, 1980. **19**(1): p. 55-79.

25. *Radiotherapy: Hidden dangers. In: 2006 Annual Report of the Chief Medical Officer* 2007, Department of Health: London.

26. Grein, E.E., R. Lee, and K. Luchka, *An investigation of a new amorphous silicon electronic portal imaging device for transit dosimetry.* Med Phys, 2002. **29**(10): p. 2262-8.

27. He, X., et al., *Evaluation of an electronic portal imaging device for transit dosimetry.* Acta Oncol, 1999. **38**(5): p. 591-6.

28. Symonds-Tayler, J.R., M. Partridge, and P.M. Evans, *An electronic portal*

imaging device for transit dosimetry. Phys Med Biol, 1997. **42**(11): p. 2273-83.

29. Alecu, R., M. Alecu, and T.G. Ochran, *A method to improve the effectiveness of diode in vivo dosimetry.* Med Phys, 1998. **25**(5): p. 746-9.

30. Lee, P.C., J.M. Sawicka, and G.P. Glasgow, *Patient dosimetry quality assurance program with a commercial diode system.* Int J Radiat Oncol Biol Phys, 1994. **29**(5): p. 1175-82.

31. Podgorsak, E.B., *Radiation Oncology Physics: A Handbook for Teachers and Students.* International Atomic Energy Agency, 2005.

32. Westermark, M., et al., *Comparative dosimetry in narrow high-energy photon beams.* Phys Med Biol, 2000. **45**(3): p. 685-702.

33. Danciu, C., et al., *Variation of sensitometric curves of radiographic films in high energy photon beams.* Med Phys, 2001. **28**(6): p. 966-74.

34. Zeidan, O.A., et al., *Characterization and use of EBT radiochromic film for IMRT dose verification.* Med Phys, 2006. **33**(11): p. 4064-72.

35. Essers, M. and B.J. Mijnheer, *In vivo dosimetry during external photon beam radiotherapy.* Int J Radiat Oncol Biol Phys, 1999. **43**(2): p. 245-59.

36. Jursinic, P.A. and B.E. Nelms, *A 2-D diode array and analysis software for verification of intensity modulated radiation therapy delivery.* Med Phys, 2003. **30**(5): p. 870-9.

37. Letourneau, D., et al., *Evaluation of a 2D diode array for IMRT quality assurance.* Radiother Oncol, 2004. **70**(2): p. 199-206.

38. Wong, J.H., et al., *Characterization of a novel two dimensional diode array the "magic plate" as a radiation detector for radiation therapy treatment.* Med Phys,

2012. **39**(5): p. 2544-58.

39. Jursinic, P.A., R. Sharma, and J. Reuter, *MapCHECK used for rotational IMRT measurements: step-and-shoot, TomoTherapy, RapidArc.* Med Phys, 2010. **37**(6): p. 2837-46.

40. Langen, K.M., et al., *Evaluation of a diode array for QA measurements on a helical tomotherapy unit.* Med Phys, 2005. **32**(11): p. 3424-30.

41. Poppe, B., et al., *Spatial resolution of 2D ionization chamber arrays for IMRT dose verification: single-detector size and sampling step width.* Phys Med Biol, 2007. **52**(10): p. 2921-35.

42. Stasi, M., et al., *D-IMRT verification with a 2D pixel ionization chamber: dosimetric and clinical results in head and neck cancer.* Phys Med Biol, 2005. **50**(19): p. 4681-94.

43. Venkataraman, S., et al., *The influence of a novel transmission detector on 6 MV x-ray beam characteristics.* Phys Med Biol, 2009. **54**(10): p. 3173-83.

44. van Elmpt, W., et al., *A literature review of electronic portal imaging for radiotherapy dosimetry.* Radiother Oncol, 2008. **88**(3): p. 289-309.

45. Greer, P.B. and C.C. Popescu, *Dosimetric properties of an amorphous silicon electronic portal imaging device for verification of dynamic intensity modulated radiation therapy.* Med Phys, 2003. **30**(7): p. 1618-27.

46. McCurdy, B.M., K. Luchka, and S. Pistorius, *Dosimetric investigation and portal dose image prediction using an amorphous silicon electronic portal imaging device.* Med Phys, 2001. **28**(6): p. 911-24.

47. Talamonti, C., M. Casati, and M. Bucciolini, *Pretreatment verification of IMRT*

absolute dose distributions using a commercial a-Si EPID. Med Phys, 2006. **33**(11): p. 4367-78.

48. Parent, L., et al., *Monte Carlo modelling of a-Si EPID response: the effect of spectral variations with field size and position.* Med Phys, 2006. **33**(12): p. 4527-40.

49. Winkler, P., A. Hefner, and D. Georg, *Dose-response characteristics of an amorphous silicon EPID.* Med Phys, 2005. **32**(10): p. 3095-105.

50. Attix, F.H., *Introduction to radiological physics and radiation dosimetry.* 1986.

51. Almond, P.R., et al., *AAPM's TG-51 protocol for clinical reference dosimetry of high-energy photon and electron beams.* Medical Physics, 1999. **26**: p. 1847.

52. Khan, F.M., *The Physics of Radiation Therapy*. 2003, Baltimore, MD: Williams & Wilkins.

53. *COMPASS User's Guide version P-05-008-510-001 03.* (IBA Dosimetry, Schwarzenbruck, Germany).

54. Islam, M.K., et al., *An integral quality monitoring system for real-time verification of intensity modulated radiation therapy.* Med Phys, 2009. **36**(12): p. 5420-8.

55. Poppe, B., et al., *Clinical performance of a transmission detector array for the permanent supervision of IMRT deliveries.* Radiother Oncol, 2010. **95**(2): p. 158-65.

56. Looe, H.K., et al., *Enhanced accuracy of the permanent surveillance of IMRT deliveries by iterative deconvolution of DAVID chamber signal profiles.* Phys Med Biol, 2010. **55**(14): p. 3981-92.

57. Godart, J., et al., *Reconstruction of high-resolution 3D dose from matrix measurements: error detection capability of the COMPASS correction kernel method.* Phys Med Biol, 2011. **56**(15): p. 5029.

58. Korevaar, E.W., et al., *Clinical introduction of a linac head-mounted 2D detector array based quality assurance system in head and neck IMRT.* Radiother Oncol, 2011.

59. Ahnesjo, A. and M.M. Aspradakis, *Dose calculations for external photon beams in radiotherapy.* Phys Med Biol, 1999. **44**(11): p. R99-155.

60. Antonuk, L.E., *Electronic portal imaging devices: a review and historical perspective of contemporary technologies and research.* Phys Med Biol, 2002. **47**(6): p. R31-65.

61. Piermattei, A., et al., *In vivo dosimetry by an aSi-based EPID.* Med Phys, 2006. **33**(11): p. 4414-22.

62. McDermott, L.N., et al., *Replacing pretreatment verification with in vivo EPID dosimetry for prostate IMRT.* Int J Radiat Oncol Biol Phys, 2007. **67**(5): p. 1568-77.

63. van Elmpt, W.J., et al., *Treatment verification in the presence of inhomogeneities using EPID-based three-dimensional dose reconstruction.* Med Phys, 2007. **34**(7): p. 2816-26.

64. McDermott, L.N., et al., *3D in vivo dose verification of entire hypo-fractionated IMRT treatments using an EPID and cone-beam CT.* Radiother Oncol, 2008. **86**(1): p. 35-42.

65. Chytyk, K., *Model-based prediction of portal dose images during patient*

treatment 2013 (in press).

66. Barrett, H.H. and W. Swindell, *Radiological imaging: the theory of image formation, detection, and processing.* 1996.

67. Bracewell, R.N., *The fourier transform & its applications 3rd Ed.* 2000.

68. Rossmann, K., *Point spread-function, line spread-function, and modulation transfer function. Tools for the study of imaging systems.* Radiology, 1969. **93**(2): p. 257-72.

69. Sibata, C.H., et al., *Influence of detector size in photon beam profile measurements.* Phys Med Biol, 1991. **36**(5): p. 621-31.

70. Pappas, E., et al., *Experimental determination of the effect of detector size on profile measurements in narrow photon beams.* Med Phys, 2006. **33**(10): p. 3700-10.

71. Verhaegen, F. and J. Seuntjens, *Monte Carlo modelling of external radiotherapy photon beams.* Phys Med Biol, 2003. **48**(21): p. R107-64.

72. Rogers, D. and A. Bielajew, *Monte Carlo techniques of electron and photon transport for radiation dosimetry.* 1990.

73. Chetty, I.J., et al., *Report of the AAPM Task Group No. 105: Issues associated with clinical implementation of Monte Carlo-based photon and electron external beam treatment planning.* Med Phys, 2007. **34**(12): p. 4818-53.

74. Mackie, T.R., J.W. Scrimger, and J.J. Battista, *A convolution method of calculating dose for 15-MV x rays.* Med Phys, 1985. **12**(2): p. 188-96.

75. Mohan, R., C. Chui, and L. Lidofsky, *Energy and angular distributions of photons from medical linear accelerators.* Med Phys, 1985. **12**(5): p. 592-7.

76. McCurdy, B.M. and S. Pistorius, *Photon scatter in portal images: physical characteristics of pencil beam kernels generated using the EGS Monte Carlo code.* Med Phys, 2000. **27**(2): p. 312-20.

77. Kawrakow, I. and D. Rogers, *The EGSnrc code system: Monte Carlo simulation of electron and photon transport.* 2010.

78. Nelson, W.R., H. Hirayama, and D.W.O. Rogers, *EGS4 code system*. 1985, Stanford Linear Accelerator Center, Menlo Park, CA (USA).

79. Berger, M.J., *Monte Carlo calculation of the penetration and diffusion of fast charged particles.* Methods in computational physics, 1963. **1**: p. 135-215.

80. Kawrakow, I., *Accurate condensed history Monte Carlo simulation of electron transport. I. EGSnrc, the new EGS4 version.* Med Phys, 2000. **27**(3): p. 485-98.

81. Rogers, D.W., et al., *BEAM: a Monte Carlo code to simulate radiotherapy treatment units.* Med Phys, 1995. **22**(5): p. 503-24.

82. Rogers, D., B. Walters, and I. Kawrakow, *BEAMnrc users manual.* NRC Report PIRS, 2001. **509**.

83. Malataras, G., C. Kappas, and D.M. Lovelock, *A monte carlo approach to electron contamination sources in the Saturne-25 and -41.* Phys Med Biol, 2001. **46**(9): p. 2435-46.

84. Ding, G.X., *Energy spectra, angular spread, fluence profiles and dose distributions of 6 and 18 MV photon beams: results of monte carlo simulations for a varian 2100EX accelerator.* Phys Med Biol, 2002. **47**(7): p. 1025-46.

85. Ding, G.X., *Dose discrepancies between Monte Carlo calculations and measurements in the buildup region for a high-energy photon beam.* Med Phys,

2002. **29**(11): p. 2459-63.

86. Abdel-Rahman, W., et al., *Validation of Monte Carlo calculated surface doses for megavoltage photon beams.* Med Phys, 2005. **32**(1): p. 286-98.

87. Chibani, O. and C.M. Ma, *On the discrepancies between Monte Carlo dose calculations and measurements for the 18 MV varian photon beam.* Med Phys, 2007. **34**(4): p. 1206-16.

88. Siebers, J.V., et al., *Monte Carlo computation of dosimetric amorphous silicon electronic portal images.* Med Phys, 2004. **31**(7): p. 2135-46.

89. Kawrakow, I., *Accurate condensed history Monte Carlo simulation of electron transport. II. Application to ion chamber response simulations.* Med Phys, 2000. **27**(3): p. 499-513.

90. Walters, B., I. Kawrakow, and D. Rogers, *DOSXYZnrc users manual.* NRC Report PIRS, 2005. **794**.

91. Kawrakow, I. and B.R. Walters, *Efficient photon beam dose calculations using DOSXYZnrc with BEAMnrc.* Med Phys, 2006. **33**(8): p. 3046-56.

92. Siebers, J., *Monte Carlo applications in IMRT planning and quality assurance.* Proceedings of the 2006 AAPM Summer School, edited by I. Chetty (Medical Physics Publishing Corp, Madison, WI, 2006), 2006.

93. Keall, P.J., et al., *Monte Carlo dose calculations for dynamic IMRT treatments.* Phys Med Biol, 2001. **46**(4): p. 929-41.

94. Siebers, J.V., et al., *A method for photon beam Monte Carlo multileaf collimator particle transport.* Phys Med Biol, 2002. **47**(17): p. 3225-49.

95. Das, I.J., G.X. Ding, and A. Ahnesjo, *Small fields: nonequilibrium radiation*

dosimetry. Med Phys, 2008. **35**(1): p. 206-15.

96. Jones, A.O. and I.J. Das, *Comparison of inhomogeneity correction algorithms in small photon fields.* Med Phys, 2005. **32**: p. 766.

97. Low, D.A., et al., *A technique for the quantitative evaluation of dose distributions.* Med Phys, 1998. **25**(5): p. 656-61.

98. Low, D.A. and J.F. Dempsey, *Evaluation of the gamma dose distribution comparison method.* Med Phys, 2003. **30**(9): p. 2455-64.

99. Van Dyk, J., et al., *Commissioning and quality assurance of treatment planning computers.* Int J Radiat Oncol Biol Phys, 1993. **26**(2): p. 261-73.

100. Bakai, A., M. Alber, and F. Nusslin, *A revision of the gamma-evaluation concept for the comparison of dose distributions.* Phys Med Biol, 2003. **48**(21): p. 3543-53.

101. Alber, M., et al., *Guidelines for the Verification of IMRT*. 2008: Estro.

102. Nelms, B.E., H. Zhen, and W.A. Tomé, *Per-beam, planar IMRT QA passing rates do not predict clinically relevant patient dose errors.* Med Phys, 2011. **38**(1037).

103. Ezzell, G.A., et al., *IMRT commissioning: multiple institution planning and dosimetry comparisons, a report from AAPM Task Group 119.* Department of Radiation Oncology Faculty Papers, 2009: p. 14.

CHAPTER THREE: A Monte Carlo investigation of contaminant electrons due to a novel *in vivo* transmission detector

This chapter is adapted from a manuscript entitled "A Monte Carlo Investigation of contaminant electrons due to a novel in vivo transmission detector" by Ganiyu Asuni, Martin Jensen, and Boyd McCurdy published in Physics in Medicine and Biology 56 (2011) 1207 – 1223. The work in this chapter investigates the effect of contaminant electrons generated by the transmission detector in the path of the photon beam. In addition, the impact of the device on the electron contamination model of two treatment planning system dose calculation algorithms was investigated.

3.1 Introduction

Advanced treatment techniques such as intensity modulated radiation therapy (IMRT) and volumetric modulated arc therapy (VMAT) have introduced additional challenges to ensure that the planned dose is accurately delivered to the patient. One important way of verifying the dose delivered is to perform patient-specific dose verification which becomes increasingly important as the complexity of the technique increases. Current patient-specific dose verification involves the comparison of a pre-calculated radiation dose from the treatment planning system (TPS) applied to a phantom to a measurement of the delivered radiation dose on that phantom. This measurement is performed only once before the patient treatment course begins, and without the patient

present. A better approach is to perform dose verification based on in vivo dose measurement, which offers the advantage of verifying the accuracy of every treatment fraction actually delivered to the patient. Several in vivo dosimetry systems mounted on the clinical linear accelerator, DAVID (PTW-Frieburg, Germany), area integrating energy fluence monitoring sensor (AIMS) and COMPASS (IBA Dosimetry, Germany), have recently been investigated for their effects on the beam attenuation, patient surface dose and the modulation of the photon beam [1-3]. While they have the potential of contributing positively to patient outcomes, the major concern for these devices is that they are likely to contaminate high energy photon beams used in radiation therapy with secondary electrons. An investigation of the secondary electrons they create will improve understanding of the effects of mounting these devices on clinical linear accelerators. The current study investigates several beam parameters (fluence, energy spectra, mean energy and angular distribution) of contaminant electrons from the COMPASS transmission detector (TRD).

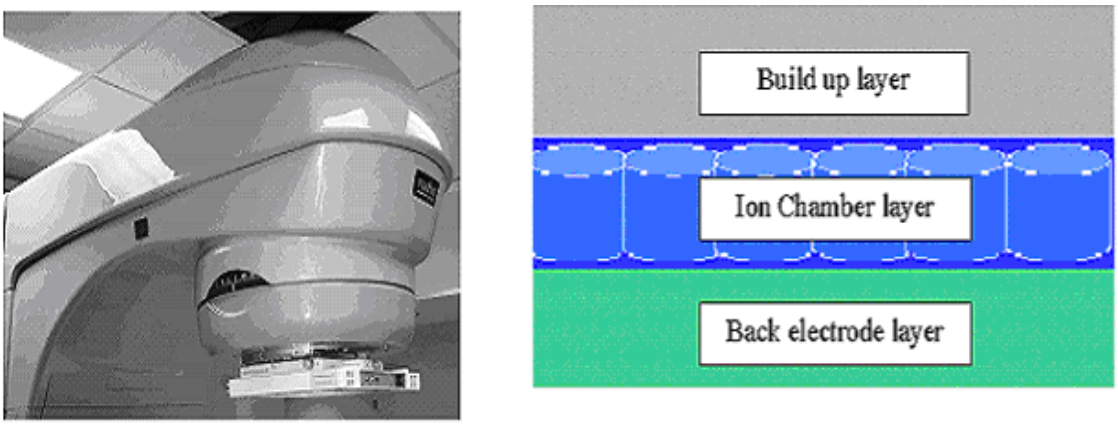
In general, contaminant electrons are due to photon interactions in the air, in the collimator, in the flattening filter and in any scattering material (such as linac-mounted dosimeters) in the path of the photon beam [4-6]. However, when a scattering material with thickness greater than the range of the secondary electrons is placed in the beam path, the scattering material absorbs almost all the incident contaminant electrons but itself becomes a major source of contaminant electrons [7] . The distance of the scattering material from the surface of the patient and the jaw settings are two important parameters that affect the contribution of contaminant electrons to surface dose. Increase in surface

dose and dose in the buildup region are known to potentially have several biological consequences, such as increased erythema, fibrosis, necrosis and epilation. 'Surface' dose is the nonzero dose at the incident surfaces i.e. the energy deposited in the sensitive cell layer of the epidermis and dermis (typically considered to be a depth of surface to 0.1 – 2.0 mm). Studies of the effects of a plastic tray on surface dose measured at different source-to-surface distances (SSDs), showed that there is a large increase in surface dose at shorter distance [8]. They found that surface dose decreases with increasing SSD, especially for large jaw settings, from 45% relative to maximum dose at SSD = 85 cm to 27% at SSD = 120 cm, for a 20 × 20 cm2 field (8 MV photon beam). To fully understand the effects of contaminant electrons on photon beams, specific physical information (such as energy spectra, angular distribution and fluence distribution) of the contaminant electrons are required, but these parameters cannot easily be experimentally measured. However, the Monte Carlo technique allows this information to be obtained. Many researchers have simulated radiation therapy beams using the BEAM/BEAMnrc code [9], based on the EGS4/EGSnrc code [10-12] for calculation of surface dose and dose in the buildup region [13-17]. Ding [14] used EGS4 and BEAM to study different beam parameters (i.e. energy spectra, angular distribution and fluence profiles) for the characterization of 6 and 18 MV photon beams. In his work, calculated surface dose and contributions from photons and charged particles (i.e. contaminant electrons and positrons) to surface dose across the field were evaluated. The increase in surface dose with increase in field size was found to be due to charged particles, and the contribution of charged particles to surface dose for a 6 MV beam increased from 7% of maximum dose to 21% for a 10 × 10 cm^2 field and a 40 × 40 cm^2 field respectively. In a different

study, Abdel-Rahman *et al* [16] found good agreement between calculated and measured percentage depth ionization (PDI) in the buildup region for a 6 MV beam. They found discrepancies in calculated and measured surface doses for an 18 MV beam (i.e. 9.6% versus 15.5%), which recently have been shown [17] to be due to incorrect primary collimator dimensions, resulting in an underestimation of electron contamination. However, using the appropriate primary collimator dimensions and parameters, calculated and measured surface doses for an 18 MV beam are within 3% [17]. Several studies have shown that detailed knowledge of electron contamination is crucial for the characterization of the photon beam and also for accurate beam modeling in clinical treatment planning algorithms using multiple-source models [5, 18-20].

Although there are several studies in the literature [8, 19, 21-23] on the effect of electron contamination in photon beams due to different scattering materials, this work provides new information about the effects of a novel TRD designed to remain in the beam path during the entire treatment day. To our knowledge the study of the effects of the contaminant electrons for these detectors has not been investigated; thus, it is of importance to potential users and developers of similar devices. The TRD is a 2D array of 1600 pixel parallel ionization chambers mountable in the block tray slot of all major vendors' radiation treatment units [2].The device is a dosimetric verification tool which measures the incident entrance beam fluence and has the ability to perform in vivo dose measurements. When used for in vivo dose measurements it will be a source of contaminant electrons, increase surface dose and dose in the buildup region, potentially affecting the prescribed patient treatment. In this work, fluence profiles, energy spectra

and angular distributions of contaminant electrons produced in the open field (i.e. no scattering material), the TRD field and the plastic block tray field were generated using the BEAMnrc/EGSnrc Monte Carlo radiation transport software and analyzed to fully understand the effects of the TRD on the clinical photon beam. The component where contaminant electrons, that reach the scoring plane, originated from was also investigated. In particular, the impact on the electron contamination model of the patient dose calculation algorithm, a critical aspect of clinical implementation, was demonstrated and quantified for two commercially available TPSs for a 6 MV photon beam.



(a) (b)

Figure 3-1 (a) TRD mounted on the gantry of the linear accelerator. (b) The TRD modeled as a three layer device in a BEAMnrc simulation

3.2 Materials and methods

3.2.1 Monte Carlo simulations of beam characteristics

Monte Carlo simulation of the head of a linear accelerator (Varian Clinac2100ix) was performed using the BEAMnrc/EGSnrc code. The 6 MV photon beam was modeled using the detailed description provided by the manufacturer. The output files of the beam simulations, the phase-space files, were obtained at 70, 80, 90 and 100 cm SSD. In this study, the phase-space files were used for two purposes. Firstly, the file was analyzed to obtain beam parameters of contaminant electrons (such as energy spectra, angular distribution and fluence profiles), to obtain particle history information (i.e. where the particle last interacted or where the particle was created), and to obtain parameter values for contaminant electron models used in two dose calculation algorithms. Secondly, the file was used as an input source (i.e. radiation beam) for surface dose calculations with DOSXYZnrc/EGSnrc user code. ECUT and PCUT were set at 0.521 and 0.010 MeV respectively; the PRESTA-II electron step algorithm and the EXACT boundary crossing algorithm where used (i.e. the simulation goes into a single elastic scattering mode whenever an electron comes closer to a boundary than a user-defined minimum step length. Russian roulette for secondary electrons was turned off.

BEAMnrc simulations with different scoring planes for non-open fields (i.e. with the TRD or plastic block tray inserted) and open fields were performed to understand the influence of the TRD on a 6 MV photon beam. The TRD was modeled using the

manufacturer's detailed description as a three-layer device as shown in figure 3.1; the buildup layer was 3.1 mm of water equivalent material, the ion chamber layer consisting of the 1600 circular plane-parallel ion chambers was 2.1 mm thick, and the back electrode layer was modeled as the radiologically equivalent thickness of 0.4 mm copper. The TRD with external dimensions of 52 cm × 49 cm × 11 cm was mounted at 65 cm from the target, while the plastic block tray with 0.6 cm thickness and density 1.2 g cm^{-3} was mounted at 64.8 cm from the target. The plastic tray is a common treatment device that has been used clinically for decades and is a known and accepted source of contaminant electrons in treatments. The effect of the scattering materials was determined from the analysis of the phase-space files produced for different SSDs (i.e. 70, 80, 90 and 100 cm) with different field sizes defined at 100 cm SSD in all test situations (i.e. open, TRD and tray). The following data were obtained from the phase-space files.

(1) Electron planar fluence profiles: to examine the influence of the scattering materials (i.e. TRD and block tray) in the production of contaminant electrons in a 6 MV photon beam.

(2) Energy spectra, mean energy and angular distribution of contaminant electrons: to understand their effect on surface dose and buildup region dose.

(3) Sources of contaminant electrons reaching the phase-space plane, to differentiate particles according to where they were created.

The BEAMDP/EGSnrc user code was used to generate fluence profiles, energy spectra, mean energies, and angular distribution of contaminant electrons at the scoring plane. For the fluence profiles, 200 square bins with 1.5 x 1.5 mm^2 size each were used

to score the fluence of contaminant electrons that reached the phase-space scoring region. The energy spectra of the contaminant electrons in the scoring region were scored in bins that are 125 keV wide. For the angular distribution for both open and non-open fields, 90 angular bins were used for scoring with minimum angle of 0^0 and maximum angle of 90^0 giving 10 per angular bin. The LATCH variable option in BEAMnrc described in [6] was used to track the history of scored particles in the phase-space file. The phase space file was read with our in-house developed MATLAB code to obtain the LATCH variable of all the contaminant electrons scored in the phase space file. The electrons were separated according to the component modules (i.e. flattening filter, monitor chamber, jaws, air, TRD, and tray) where they were created, and their percentage contributions to the total number of contaminant electrons were also obtained. For all the studies described above, 1.5 x 10^9 electron histories were simulated using the variance reduction technique uniform bremsstrahlung splitting (UBS).

3.2.2 Calculations and Measurements of Surface Dose

Dose calculation in water was performed using a 30 cm × 30 cm × 30 cm water phantom with voxels of different sizes depending on the regions of interest and the intended output. For the percentage depth-dose (PDD) calculation the voxel size used was 0.5 cm × 0.5 cm and with varying thicknesses of 0.001, 0.5 and 1 cm. For dose profile calculation the voxel size used was 0.25 cm × 0.25 cm in the in-field region and 0.5 cm × 0.5 cm in the out-of-field region with varying thicknesses of 0.001, 0.5 and 1 cm. The following dose calculation data for both open and non-open fields were

obtained: surface dose for 10 × 10 cm^2 fields at 80, 90 and 100 cm SSD, and surface dose for different square field sizes (3 × 3, 5 × 5, 10 × 10 and 20 × 20 cm^2) at 90 cm SSD. The field sizes used in this study are defined at the isocenter (i.e. SAD = 100 cm). Percentage depth-dose (PDD), dose profiles and output factors calculated at 90 cm SSD with Monte Carlo simulations were validated with measurements on a 6 MV Clinac 2100iX (Varian Associates, Inc., Oncology Systems, Palo Alto, CA) with Millennium 120-leaf MLC. In this study, all measurements were performed with a Markus-type PTW Model 329 fixed parallel-plate chamber, and measurements in the buildup region were corrected for overresponse using Mellenberg's correction factor [24]. The chamber was inserted in a 30 × 30 cm^2 slab of solid water with 10 cm of solid water backscatter to ensure full phantom scatter conditions.

The influence of the TRD on calculated surface doses of photon beams for different SSDs (80, 90 and 100 cm) and for different square field sizes (3 × 3, 10 × 10, 20 × 20 cm^2) at 90 cm SSD was studied and compared to measured data under similar conditions but using the plastic block tray. The increase in contributions of contaminant electrons due to TRD and tray on surface dose and dose in buildup region as compared to the contaminant electron contributions for open fields was calculated as a function of SSD and field size. To accomplish this, PDDs due to contaminant electrons only were calculated (ePDDs) for the various field sizes for the open, TRD and block tray fields. The additional contribution of contaminant electrons was taken as the difference between the ePDDs of the non-open fields (i.e. TRD and tray) and the open field. The contaminant electrons scored in the phase-space file were read using

READPHSP/EGSnrc user code and then used as a source in the DOSXYZnrc dose calculations to obtain contaminant electrons only PDD which are normalized to the maximum dose.

3.2.3 Effect of the TRD on TPS modeling of electron contamination

Accurate beam models used in TPSs are required to reproduce treatment unit characteristics for dose calculation (Ahnesjö and Aspradakis 1999). A variation of the multiple-source model widely reported in the literature [20, 25-27] is currently implemented in the dose calculation algorithms of most major vendors' TPSs. One of the major components in any multiple-source model for dose calculation of megavoltage photon beams is the electron contamination source. The electron contamination source is typically characterized by several model parameters derived from measured data or from Monte Carlo phase-space data. It is modeled to accurately account for dose due to contaminating electrons in the beam. The parameters influence the amount of electron dose that will be included in the TPS calculated dose, the maximum depth of dose deposition due to contaminant electrons, and the off-axis and field-size dose effects of contaminating electrons. In this study the impact of the TRD on contaminant electron model parameters developed specifically for the anisotropic analytic algorithm (AAA) version 8.6.1.4 in Eclipse Integrated Treatment Planning System (Varian Medical Systems, Palo Alto, CA) and the Pinnacle^3 collapsed cone superposition dose algorithm release 7.6 have been investigated.

The energy fluence of electron contamination source in AAA has been proposed as a linear combination of two convolution terms [20] :

$$\Phi_e(x,y) = c\Phi_{ph}(x,y) \otimes G_1(x,y) + (1-c)\Phi_{ph}(x,y) \otimes G_2(x,y) \quad (3.1)$$

where Φ_e and Φ_{ph} are the electron and photon energy fluence respectively, G_i is a Gaussian kernel with width σ_i, and c is their relative weight. The Gaussian widths and the relative weight are free parameters in the beam model. The first Gaussian represents the electrons created inside the field while the second Gaussian represents electrons created outside the field (Eclipse Algorithms Reference Guide, 2008). The electron and photon energy fluence of particles scored in the phase-space at 100 cm SSD for different field sizes were obtained for open and TRD fields. An optimization algorithm developed in MATLAB (MathWorks, Natick, MA) was used to model equation 3.1. The three free parameters, both Gaussian widths and relative weight with and without TRD were obtained and compared.

In the Pinnacle^3 dose calculation algorithm, the electron contamination model accounts for electron depth dose effect, off-axis effect, and field size effect of contaminating electrons (Pinnacle^3 Physics Reference Guide, 2005). The electron depth dose parameters model the rate of electron dose fall-off with respect to depth using:

$$ED_{depth}(d_{fs}) = \frac{F_{FS}(fs)}{SF} \times \frac{e^{-K.d} - e^{-K.MAXD}}{1 - e^{-K.MAXD}} \quad (3.2)$$

where F_{FS} is the electron surface dose, MAXD is the electron maximum depth, K (depth coefficient) and SF (scale fraction) are parameters determining the linear region which replaces the exponential decrease in dose with depth. In this work, calculations of

electron depth dose in water with and without the TRD in DOSXYZnrc for different field sizes were performed as described in section 3.2.2 for PDD calculation. The depth dose curves were fitted to equation 3.2 and the depth coefficient (K) and scale fraction (SF) for with and without the TRD were obtained.

The off-axis model accounts for the change in electron contamination away from the central axis. In Pinnacle[3] the off-axis parameter allows the shaping of the electron contamination dose magnitude and is modeled using:

$$F_{OA}(r) = e^{-OAC \times r^2} \tag{3.3}$$

where F_{OA} is the relative electron fluence, OAC(off-axis coefficient) is the representation of the FWHM of the normalized fluence profile, and r is the off-axis distance. The function in equation 3.3 is fitted to MC simulated electron fluence profiles scored at 100 cm SSD for different field sizes with and without TRD to obtain their respective OAC. Finally, the electron contamination field-size parameters model changes in contaminating electrons as a function of field size. The electron contamination field-size effect in Pinnacle[3] is modeled using:

$$F_{FS}(fs) = ECD_{10\times10} + C_1.(fs - 10) + C_2(e^{-C_3.10} - e^{-C_3.fs}) \tag{3.4}$$

where $ECD_{10 \times 10}$ is the electron contamination surface dose for a 10×10 cm^2 field, *fs* is the field size, and model parameters C1, C2 and C3 account for the change in contaminating electron dose for different field sizes. Calculated electron surface dose for different field sizes with and without the TRD were used to obtain the model parameters.

3.3 Results and Discussion

3.3.1 Validation of the Monte Carlo model

Monte Carlo simulations of the PDD, beam profiles, and output factors of different field sizes were validated with measured data for several 6 MV photon fields incident on a water phantom. Calculated and Mellenberg's corrected measured PDD data between the surface and a few mm beyond the buildup region agree well within 2% of maximum dose (see figure A-II in Appendix A of thesis). For beam profiles, calculated data inside the field and at field edges are well within 1.5% of measured data, and for outside the field they are within 2% of maximum dose. Comparison of calculated and measured output factors for different field sizes at depth of maximum dose (d_{max}) shows good agreement within about 1.5% for all field sizes.

3.3.2 Beam characteristics from phase-space analysis

3.3.2.1 Electron fluence

The electron planar fluence profiles of non-open fields (TRD and block tray) and open fields for a 10×10 cm^2 field at 70 and 100 cm SSDs are shown in figures 3.2(a) and (b) respectively.

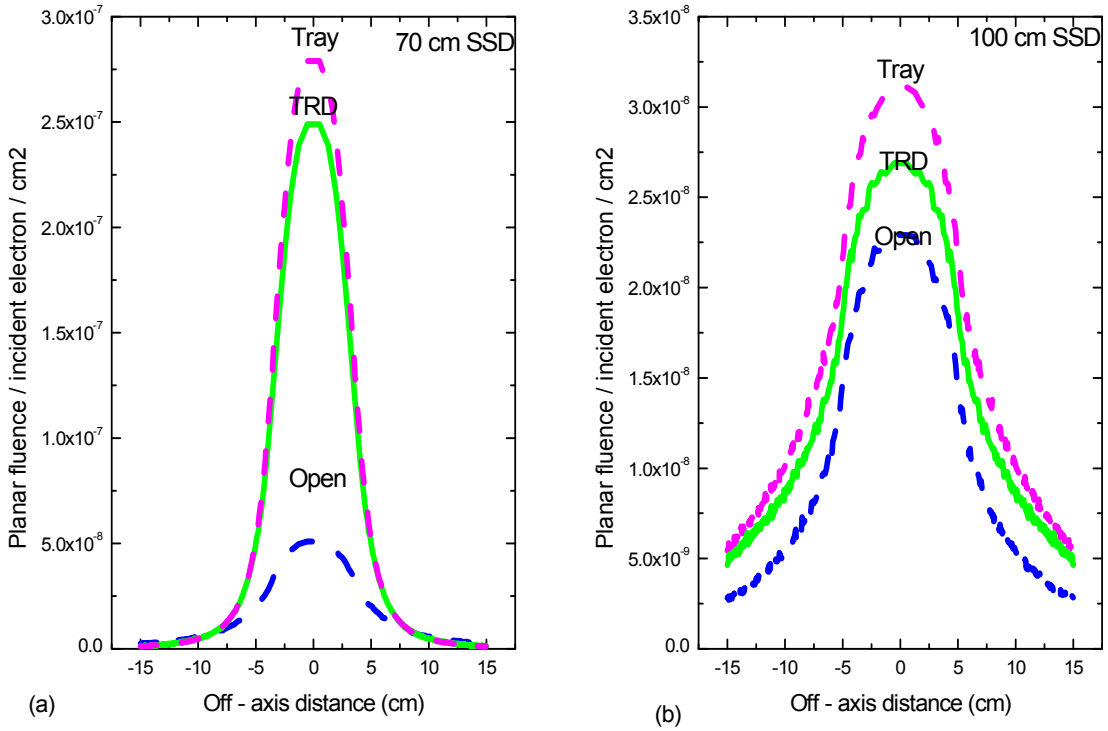


Figure 3-2: Planar fluence profiles of contaminant electrons for open and non-open 10x10 cm^2 fields scored in the phase-space at (a) 70 cm SSD and (b) 100 cm SSD

At 70 cm SSD, the electron fluence profiles increase dramatically when the TRD or the block tray is introduced in the beam path. On the central axis in a 1 x 1 cm^2 scoring region, electron fluence increased by 389% in the presence of the TRD and increased by 448% in the presence of the block tray compared to the open beam. However, at 100 cm SSD, with the TRD and block tray in the beam path, the electron fluence increases are much less. On the central axis, electron fluence increased by 17.5% in the presence of the TRD and increased by 35.8% in the presence of the block tray compared to the open

beam. The electron fluence profiles for open and non-open fields at 100 cm SSD for different field sizes (5x5, 10x10, and 20 x 20 cm^2) are shown in figure 3.3; electron fluences are normalized to the central axis of the 10 x 10 cm^2 field. In figure 3.3, the electron fluence for the 20 x 20 cm^2 field size of non-open fields have larger magnitude and are more laterally spread compared to the open field. In addition, the electron fluence increases with increasing field size for both open and non-open fields as expected. On the central axis of the TRD field, the electron fluence for the 5 x 5 cm^2 field is 41.6% of the fluence for the 10 x 10 cm^2 field, while the fluence for the 20 x 20 cm^2 field is 127% larger than that of the 10 x 10 cm^2 field. Similarly in the block tray field, the electron fluence on the central axis for the 5 x 5 cm^2 field is 58.2% of the fluence for the 10 x 10 cm^2 and the fluence for the 20 x 20 cm^2 field is 129% larger than that of the 10 x 10 cm^2 field. This quantifies the expected increase in contaminant electron fluence with increasing field size [19, 22].

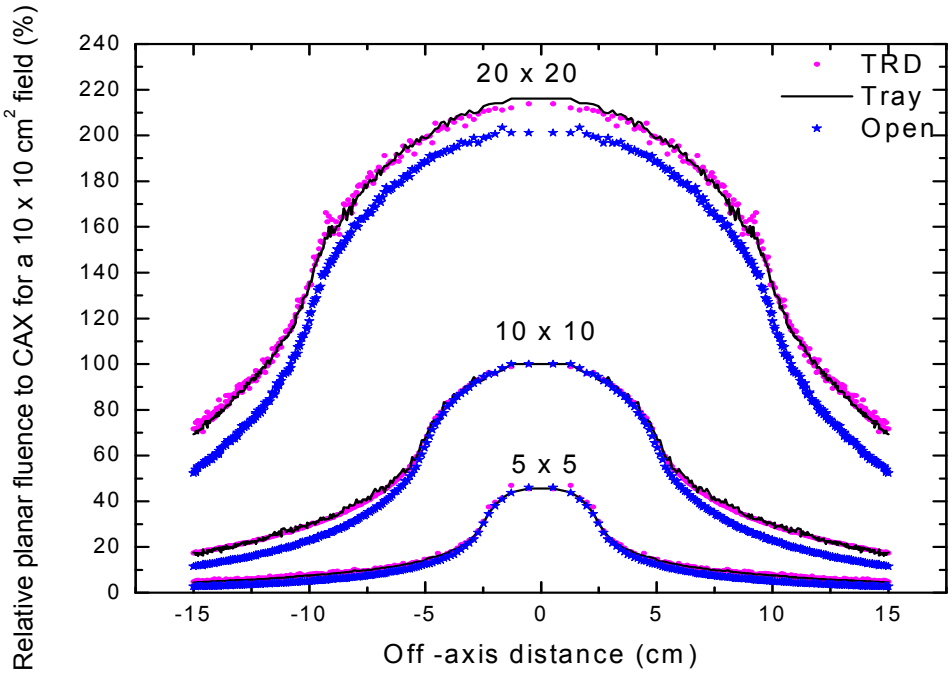


Figure 3-3: Planar fluence profiles of contaminant electrons scored in the phase-space at 100 cm SSD for different field sizes in open and non - open fields: TRD (●) and Tray (—).

3.3.2.2 Energy spectra, mean energy, and angular distribution

In figure 3.4a and b, the calculated planar energy fluence from the open and non-open fields are normalized to the maximum planar energy fluence for 10 x 10 cm^2 for open field scored at 100 cm SSD. As shown in figure 3.4a, at shorter SSD (i.e., 70 cm) there is a large increase in electron fluence in the presence of TRD and block tray. However, most of the contaminant electrons are less energetic such that the percentage energy fluence of contaminant electrons below 2 MeV to total electrons are 74.6%,

76.4% and 81.0% for open, TRD, and block tray respectively. High-energy particles mainly produced above the scattering materials (i.e., TRD and block tray) in air and in the flattening filter interact with the materials to generate additional contaminant electrons with low energies for non-open fields. Low energy electrons are known to contribute to surface dose, thus at 70 cm SSD contaminant electrons produced in both TRD and block tray fields will increase the surface dose. At 100 cm SSD, most of the contaminant electrons from the block tray with relatively low energies will contribute more to the dose at the surface compared to electrons produced in the TRD field. The average or mean energies of the contaminant electrons scored in the phase-space file at 70 cm and 100 cm SSD for open and non-open field are shown in Table 3.1. Contaminant electrons scored at 70 cm SSD phase-space plane for the block tray have mean energy relatively lower than for the open field and TRD, this is probably due to the large number of low energy electrons created in this field. Although one would expect that the mean energy of contaminant electrons for the TRD and the block tray to be similar at 100 cm SSD, the back electrode of the TRD (made of copper) results in a relatively small “beam hardening” effect as seen in Table 3.1.

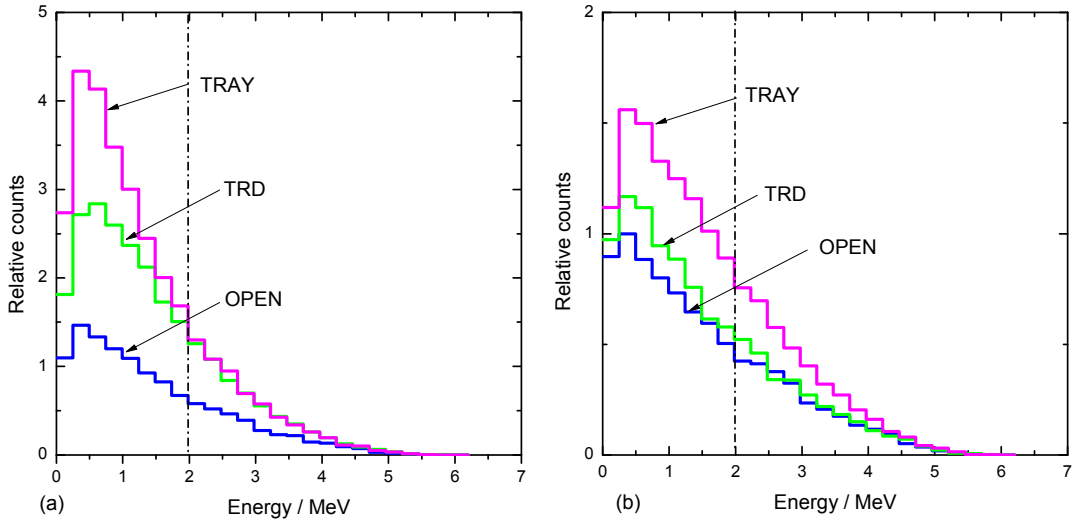


Figure 3-4: Energy spectra of contaminant electrons for open and non-open 10x10 cm^2 fields scored in the phase-space at (a) 70 cm SSD and (b) 100 cm SSD. The absolute counts/MeV/incident electrons are normalized to the maximum value for the 10 x10 cm^2 open field at 100 cm SSD.

Table 3-1. Mean energy of contaminant electrons for open and non-open 10x10 cm^2 fields scored at 70 cm and 100 cm SSD in the 30 x 30 cm^2 phase-space file.

SSD (cm)	OPEN	TRD	TRAY
70	1.23 ± 0.01 MeV	1.29 ± 0.01 MeV	1.12 ± 0.01 MeV
100	1.32 ± 0.01 MeV	1.37 ± 0.01 MeV	1.35 ± 0.01 MeV

The angular distribution of contaminant electrons produced in the open and non-open fields at 70 cm SSD and 100 cm SSD are shown in figure 3.5a and b. The large angular distribution for contaminant electrons is an indication that they are low energy particles and are likely to scatter or be absorbed in air. Here the absolute count per degree is normalized to the maximum value for the 10 x 10 cm^2 open field. In figure 3.5a, contaminant electrons in the non-open field have large angular spread, with average relative counts/degree of 64.0% and 80.8% for TRD and block tray respectively, compared to the open field with 33.5% average relative counts/degree. Again, the average relative counts/degree for block tray is an indication of large number of low energy electrons produced in this field. The angular distributions of the contaminant electrons at 100 cm SSD for the non-open fields show smaller angular spread compared to those at 70 cm SSD which indicates that there are more low energy electrons at 70 cm SSD. With average relative counts/degree of 29.5% and 41.6% for TRD and block tray respectively, these angular distributions exhibit only a small shift from the angular distribution of the open field with average relative counts/degree of 25.6% compared to those at 70 cm SSD.

The effect of different field sizes on angular distribution of contaminant electrons was studied. The angular distributions of contaminant electrons for open and non-open fields at 100 cm SSD for two field sizes (5 x 5 cm^2 and 20 x 20 cm^2) are shown in figure 3.6a and b. For both field sizes, the angular spread of contaminant electrons in non-open fields is similar. However, electrons of the open field have smaller angular spread compared to non-open fields, and the contaminant electrons in the non-open fields are

likely to be scattered or absorbed in air, creating secondary particles that are stopped either on or in the phantom/patient. It is noted that the angular distributions of contaminant electrons produced at 100 cm SSD for different field sizes (i.e. 5 x 5 cm^2, 10 x 10 cm^2, and 20 x 20 cm^2) in both open and non-open fields have similar shapes when normalized to the maximum counts for open field. Hence, angular distributions of contaminant electrons produced at 100 cm SSD are not strongly dependent on field size.

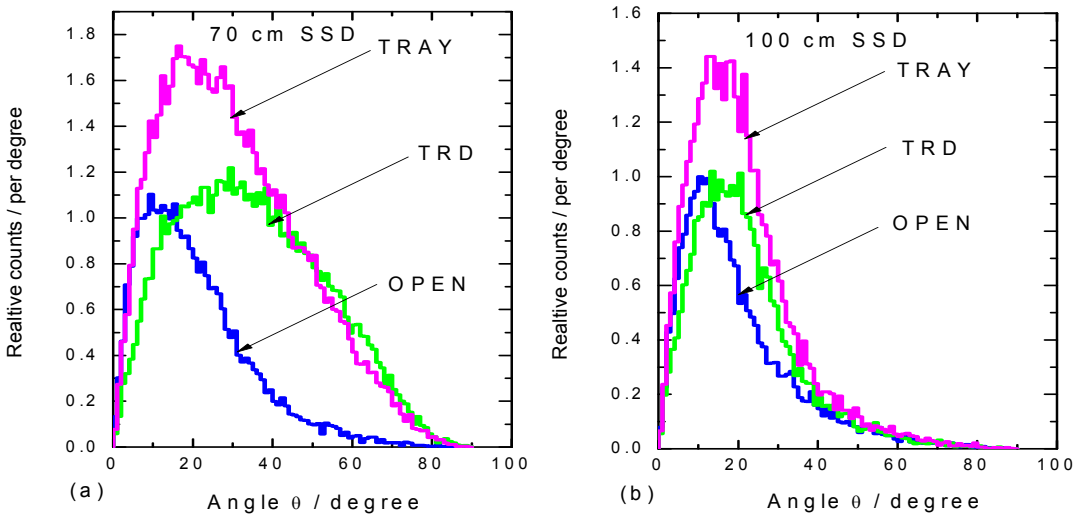


Figure 3-5: Angular distributions of contaminant electrons for open and non-open 10x10 cm2 fields scored in the phase-space at (a) 70 cm SSD and (b) 100 cm SSD. The absolute counts/per degree are normalized to the maximum value for the open field scored at 100 cm SSD.

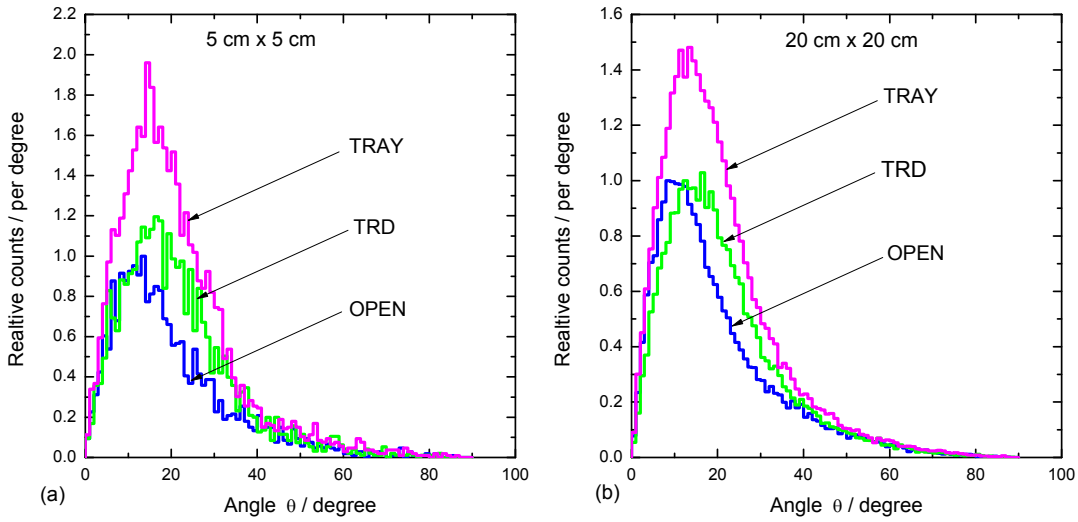


Figure 3-6: The angular distribution of open and non-open fields for field sizes (a) 5 x 5 cm^2 and (b) 20 x 20 cm^2, at 100 cm SSD. The absolute counts/per degree are normalized to the maximum value for the open field.

3.3.2.3 Sources of scored particles

Contaminant electrons are categorized according to the region where they were created. The percentage of contaminant electrons from the beam simulation scored in the phase-space at 70 cm and 100 cm SSD are shown in Table 3.1 and 3.2, respectively. In Tables 3.2 and 3.3, the contaminant electrons produced in the flattening filter, monitor chambers, jaws, TRD and air are normalized to the total number of electrons scored in a 30 x 30 cm^2 phase space plane at 70 and 100 cm SSD respectively. The main source of contaminant electrons without the TRD in place is the air, and the percentage of electrons

created increases with increasing SSD. However, when the TRD is placed in the beam path, it absorbs all the electrons generated above it but then becomes the major source of contaminant electrons as shown in Tables 3.2 and 3.3. In Tables 3.2 and 3.3 the percentage of the contaminant electrons created in the TRD (i.e. portion from the TRD to total electrons scored) for different field sizes are similar. However, the number of scored contaminant electrons created in the TRD increases with increasing field size. As stated in section 3.3.2.1, additional contaminant electrons in the phase-space plane are due to the increase in field size and are scattered or absorbed in air at larger SSD. These explain the reduction in the percentage of electrons created in TRD and the increase in the percentage of electrons created in air at larger SSD (Table 3.3).

Table 3-2: Contaminant electrons scored in the phase-space at 70 cm SSD from different component modules in the linear accelerator model. Raw particle counts are shown, with the percentage of total fluence given in parentheses.

Component	5 x 5 cm^2		10 x 10 cm^2		20 x 20 cm^2	
Modules (CM)	OPEN	TRD	OPEN	TRD	OPEN	TRD
Flattening Filter	577 (13.3%)	103 (1.5%)	3444 (18.7%)	549 (2.0%)	15246 (21.2%)	2077 (2.1%)
Chambers	456 (10.5%)	43 (0.6%)	2654 (14.4%)	319 (1.2%)	12353 (17.2%)	1108 (1.1%)
Jaws	1773 (40.9%)	95 (1.4%)	5808 (31.5%)	317 (1.2%)	15458 (21.5%)	783 (0.8%)
TRD	n/a	6099	n/a	24249	n/a	90190

		(91.0%)		(90.0%)		(90.2%)
Air	1525	362	6552	1511	28752	5846
	(35.2%)	(5.4%)	(35.5%)	(5.6%)	(40.0%)	(5.8%)
Total	4332	6702	18459	26946	71809	100004
	(100%)	(100%)	(100%)	(100%)	(100%)	(100%)

Table 3-3: Contaminant electrons scored in the phase-space at 100 cm SSD from different component modules in the linear accelerator model. Raw particle counts are shown, with the percentage of total fluence given in parentheses.

Component	5 x 5 cm^2		10 x 10 cm^2		20 x 20 cm^2	
Modules (CM)	OPEN	TRD	OPEN	TRD	OPEN	TRD
Flattening Filter	502 (13.1%)	50 (1.0%)	2921 (18.1%)	316 (1.6%)	12577 (19.8%)	1187 (1.6%)
Chambers	368 (9.7%)	25 (0.5%)	2099 (13.0%)	201 (1.0%)	9387 (14.8%)	642 (0.9%)
Jaws	884 (23.2%)	56 (1.1%)	2658 (16.5%)	156 (0.8%)	6259 (9.9%)	413 (0.6%)
TRD	n/a	3625 (73.1%)	n/a	14305 (71.3%)	n/a	52500 (70.3%)
Air	2051 (53.9%)	1201 (24.2%)	8423 (52.3%)	5085 (25.3%)	35293 (55.6%)	19911 (26.7%)
Total	3806 (100%)	4957 (100%)	16102 (100%)	20063 (100%)	63516 (100%)	74653 (100%)

3.3.3 Comparison of Calculated and Measured surface Dose

Calculated and measured surface dose relative to maximum dose in a 10 x 10 cm^2 field for three clinical SSDs (80, 90, and 100 cm) from open and non-open fields have been compared in Table 3.4. The statistical uncertainty (σ_{total}) of the calculated data is the quadrature sum of the Monte Carlo statistical error for a particular depth (σ_{depth}) and statistical error at depth of maximum dose d_{max} (σ_{dmax}), where $\sigma_{total} = \left(\sigma_{depth}^2 + \sigma_{d\max}^2\right)^{0.5}$ [16]. It is consistently estimated as 0.4% relative to maximum dose, while measured data were estimated to have a 0.5% uncertainty as reported by Mellenberg [24]. As shown in Table 3.3 the agreement between calculated and measured surface dose is good with an average dose difference of <3% (i.e. the difference between calculated surface dose and measured surface dose). For all fields (i.e. open and non-open), the surface doses, either calculated or measured, are higher for the block tray than for TRD and open fields. This is expected because the fluence of contaminant electrons produced in the block tray field (shown in figure 3.2 and 3.3) is larger than those produced in other fields at shorter and larger SSDs. Also, most of the contaminant electrons are of low energy and unable to penetrate deeper inside the phantom, but rather deposit their energy on the phantom surface, thus increasing the surface dose.

Table 3-4: Calculated and measured percentage surface dose relative to maximum dose in a 10 x 10 cm^2 field for open and non-open fields.

SSD (cm)	MC_open (%)	Meas_Open (%)	MC_TRD (%)	Meas_TRD (%)	MC_Tray (%)	Meas_Tray (%)
80	14.0 ± 0.4	15.1 ± 0.5	20.6 ± 0.4	23.4 ± 0.5	22.6 ± 0.4	24.9 ± 0.5
90	13.3 ± 0.4	14.6 ± 0.5	16.4 ± 0.4	17.8 ± 0.5	17.4 ± 0.4	19.6 ± 0.5
100	13.6 ± 0.4	15.0 ± 0.5	14.8 ± 0.4	16.8 ± 0.5	16.9 ± 0.4	17.5 ± 0.5

The increased contribution of contaminant electrons on surface dose for non-open fields has been evaluated by taking the difference between the contaminant electron surface dose of the non-open fields (i.e. TRD and block tray) and the open field. Table 3.5 shows the calculated surface dose due to contaminant electrons and the extra contribution of contaminant electrons compared to the open field on surface dose at 80, 90, and 100 cm SSD. As expected, the contribution of contaminant electrons decreases with increasing SSD because most of the electrons are scattered or absorbed in air before reaching the phantom surface, as shown earlier in figure 3.2. The maximum additional contribution of contaminant electrons on surface dose of 17.4% and 8.6% were calculated for block tray respectively at 80 cm SSD, while the minimum additional contribution of contaminant electrons of 8.9% and 0.5% were calculated for TRD respectively at 100 cm SSD.

Table 3-5: Contaminant electron surface dose (ESD) relative to maximum dose and additional electron contamination contribution to dose at the surface (compared to open field) in a 10 x 10 cm^2 field for both TRD and block tray.

SSD (cm)	ESD_{open} (%)	ESD_{TRD} (%)	ESD_{TRAY} (%)	$ESD_{TRD} - ESD_{open}$ (%)	$ESD_{TRAY} - ESD_{open}$ (%)
80	8.8 ± 0.4	11.9 ± 0.4	17.4 ± 0.4	3.1 ± 0.6	8.6 ± 0.6
90	8.6 ± 0.4	9.7 ± 0.4	12.6 ± 0.4	1.1 ± 0.6	4.0 ± 0.6
100	8.4 ± 0.4	8.9 ± 0.4	11.2 ± 0.4	0.5 ± 0.6	2.8 ± 0.5

The effect of different jaw settings (i.e. 3 x 3 cm^2, 10 x 10 cm^2, and 20 x 20 cm^2) on surface dose was also investigated. From the contamination electron calculated dose in the buildup region at 90 cm SSD for open and non-open fields, the extra contribution of contaminant electrons with increased field size for both TRD and block tray are shown in figure 3.7. Due to the increase in scattered radiation as jaw settings increase, the contribution of contaminant electrons for TRD and block tray increases with field size. The maximum contribution of contaminant electrons of 5% and 14% for 20 x 20 cm^2 field was calculated for the TRD and block tray respectively and a minimum contribution for 3 x 3 cm^2 field of 0.2% and 0.6% was calculated for TRD and block tray respectively.

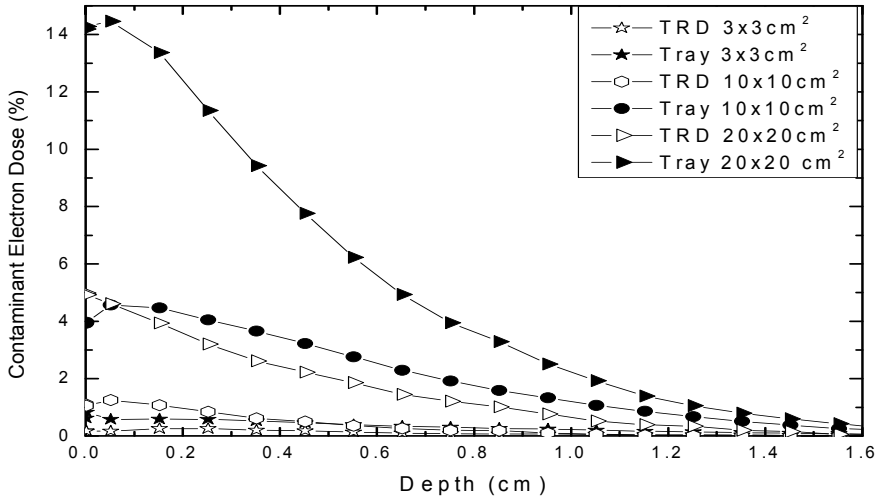


Figure 3-7: Extra contribution of contaminant electrons to surface dose for different field sizes for TRD and block tray. The extra contaminant electron dose is the difference between the calculated ePDDs for non-open fields and open fields, as described in section 3.2.2.

3.3.4 Electron contamination model parameters with and without TRD

The contaminant electron source model parameters of equation 3.1, used in the AAA dose calculation algorithm have been calculated for different field sizes (5 x 5, 10 x 10, and 20 x 20 cm^2) with and without the TRD using an optimization algorithm. The algorithm is based on the least square non-linear data fitting function (lsqnonlin) in the optimization toolbox in MATLAB. The optimization function derives the minimization of the objective function by calculating the deviation between the right hand side and left hand side of equation 3.1 in a least square sense. The optimized average Gaussian widths

and relative weights for all the field sizes increase when the detector is in the beam as shown in Table 3.6. Increases of 12% and 15% were found in the first and second Gaussian widths respectively when the detector is in the beam path, an indication of the larger spread of the contaminant electron fluence due to the TRD (figure 3.3).

Table 3-6: The optimized electron contamination parameters (i.e. average for 5 x 5, 10 x 10, and 20 x 20 cm^2 field sizes) for the Eclipse AAA dose algorithm (equation 3.1): Gaussian widths s1 and s2 and c the relative weight of the first Gaussian for open and TRD fields.

Fields	σ_1 (mm)	σ_2 (mm)	c (%)
OPEN	7.3	50.8	8.3
TRD	8.2	58.5	17.0

Depth dose effect model parameters used in Pinnacle[3] dose calculation algorithm, the scale fraction (SF) and depth coefficient (K) for different field sizes for both open and TRD fields are shown in Table 3.6. Both model parameters decrease in the presence of the TRD for all field sizes. The average SF and K values for all field sizes when the device is used are 1.05 and 1.77 compared to 1.08 and 2.07 in the open field. For the off-axis model parameter, the contaminating electron fluence scored at 100 cm SSD is normalized to the beam central axis after removing the offset value at the field edges. The off-axis coefficient (OAC) indicates how broad the contaminant electron fluence is, and for different field sizes with and without the TRD are shown in Table 3.7. The OAC for

the TRD is less than those without the device except for the largest field size and it decreases with increasing field size. Table 3.8 contains the model parameters for contaminant electrons output factors described in section 3.2.3 with and without the TRD for different field sizes (3 x 3, 5 x 5, 10 x 10, and 20 x 20 cm^2). Comparing the contaminant electrons output factors model parameters, there is a change with the TRD to without the device. While model parameter C1 increases with the device, parameters C2 and C3 decrease when the device is in the beam path.

In general, the observed differences in the electron model parameters for both commercial dose calculation algorithms show that the effect of the device should be considered in the treatment planning system. Based on the result presented in this chapter the contaminant electron model parameters in both calculation algorithms can be adjusted for improved accuracy of beam modeling in the treatment planning system. A similar recommendation has been proposed for other beam modifiers such as the block tray and the physical wedge [19].

Table 3-7: The depth dose and off-axis effect electron contamination parameters in Pinnacle^3 dose calculation algorithm (equation 3.2 and 3.3): the scale fraction (SF), depth coefficient (K), off-axis coefficient (OAC) and for open and TRD fields.

Field Size (cm^2)	SF_{OPEN}	SF_{TRD}	K_{OPEN}	K_{TRD}	OAC_{OPEN} (cm)	OAC_{TRD} (cm)
5 x 5	1.12 ± 0.01	1.07 ± 0.01	2.14 ± 0.07	1.79 ± 0.04	0.06 ± 0.01	0.05 ± 0.01
10 x 10	1.08 ± 0.01	1.06 ± 0.01	1.96 ± 0.05	1.73 ± 0.03	0.022 ± 0.002	0.020 ± 0.001
20 x 20	1.06 ± 0.01	1.02 ± 0.01	2.01 ± 0.04	1.78 ± 0.02	0.009 ± 0.002	0.009 ± 0.002

Table 3-8: The relative output effect (i.e. average for 5 x 5, 10 x 10, and 20 x 20 cm^2 field sizes) in Pinnacle^3 dose calculation algorithm (equation 3.4) for open and TRD field

Fields	C1	C2	C3
OPEN	3.96×10^{-2}	0.56×10^{1}	12.34×10^{-3}
TRD	10.91×10^{-2}	0.26×10^{1}	-0.11×10^{-3}

3.4 Conclusions

This work presents a comprehensive study of contaminant electrons in a clinical photon beam originating from an in vivo measurement device. Monte Carlo simulation was used to study the influence of the TRD on beam characteristics, surface dose and

dose in the build-up region, and on contaminant electron model parameters in two commercial dose calculation algorithms, as required prior to clinical implementation. The detector introduces additional contaminant electrons compared to the open field. These electrons are less energetic and have larger angular spread compared to contaminant electrons in an open field at shorter SSDs. It is shown that without the TRD in the beam path, the air (i.e. within the linac head and between the linac head and the phantom surface) is the major source of contaminant electrons and similar results have been reported in the literature for other in-field treatment devices[4, 28]. When the TRD is placed in the beam path it absorbs most of the incident contaminant electrons and becomes the major source of contaminant electrons. The effects of the TRD and block tray on surface dose and dose in build-up region show that the contribution of contaminant electrons to dose increases with increasing field size, with calculated extra contributions (i.e., difference between the contaminant electron surface dose of the non-open fields and the open field) of 14% and 5% (relative to maximum dose) for a 20 x 20 cm^2 field and 0.6% and 0.2% for a 3 x 3 cm^2 field, for a standard block tray and the TRD device respectively. The device has been shown to have a non-negligible impact on the contamination electron model parameters of two commercial dose calculation algorithms. The Gaussian widths in the contaminant electron source model in Eclipse AAA dose algorithm have been found to increase by 12% and 15% when the device is in the beam. The Pinnacle^3 off-axis coefficient (OAC) decreases with TRD, as expected due to the larger contaminant electron fluence from the device. Finally, the TRD may be used for in vivo dosimetry with the contaminant electron model parameters in the treatment planning system modified as described here for accurate dose calculation when using the device.

3.5 Bibliography

1. Islam, M.K., et al., *An integral quality monitoring system for real-time verification of intensity modulated radiation therapy.* Med Phys, 2009. 36(12): p. 5420-8.
2. Venkataraman, S., et al., *The influence of a novel transmission detector on 6 MV x-ray beam characteristics.* Phys Med Biol, 2009. 54(10): p. 3173-83.
3. Poppe, B., et al., *Clinical performance of a transmission detector array for the permanent supervision of IMRT deliveries.* Radiother Oncol, 2010. 95(2): p. 158-65.
4. Nilsson, B. and A. Brahme, *Absorbed dose from secondary electrons in high energy photon beams.* Phys Med Biol, 1979. 24(5): p. 901-12.
5. Zhu, T.C. and J.R. Palta, *Electron contamination in 8 and 18 MV photon beams.* Med Phys, 1998. 25(1): p. 12-9.
6. Malataras, G., C. Kappas, and D.M. Lovelock, *A monte carlo approach to electron contamination sources in the Saturne-25 and -41.* Phys Med Biol, 2001. 46(9): p. 2435-46.
7. Khan, F.M., *The Physics of Radiation Therapy*. 2003, Baltimore, MD: Williams & Wilkins.
8. Kim, S., et al., *Photon beam skin dose analyses for different clinical setups.* Med Phys, 1998. 25(6): p. 860-6.
9. Rogers, D.W., et al., *BEAM: a Monte Carlo code to simulate radiotherapy treatment units.* Med Phys, 1995. 22(5): p. 503-24.

10. Mohan, R., C. Chui, and L. Lidofsky, *Energy and angular distributions of photons from medical linear accelerators.* Med Phys, 1985. 12(5): p. 592-7.

11. van der Zee, W. and J. Welleweerd, *Calculating photon beam characteristics with Monte Carlo techniques.* Med Phys, 1999. 26(9): p. 1883-92.

12. Kawrakow, I. and B.R. Walters, *Efficient photon beam dose calculations using DOSXYZnrc with BEAMnrc.* Med Phys, 2006. 33(8): p. 3046-56.

13. Ding, G.X., *Dose discrepancies between Monte Carlo calculations and measurements in the buildup region for a high-energy photon beam.* Med Phys, 2002. 29(11): p. 2459-63.

14. Ding, G.X., *Energy spectra, angular spread, fluence profiles and dose distributions of 6 and 18 MV photon beams: results of monte carlo simulations for a varian 2100EX accelerator.* Phys Med Biol, 2002. 47(7): p. 1025-46.

15. Ding, G.X., C. Duzenli, and N.I. Kalach, *Are neutrons responsible for the dose discrepancies between Monte Carlo calculations and measurements in the build-up region for a high-energy photon beam?* Phys Med Biol, 2002. 47(17): p. 3251-61.

16. Abdel-Rahman, W., et al., *Validation of Monte Carlo calculated surface doses for megavoltage photon beams.* Med Phys, 2005. 32(1): p. 286-98.

17. Chibani, O. and C.M. Ma, *On the discrepancies between Monte Carlo dose calculations and measurements for the 18 MV varian photon beam.* Med Phys, 2007. 34(4): p. 1206-16.

18. Yang, J., et al., *Modelling of electron contamination in clinical photon beams for Monte Carlo dose calculation.* Phys Med Biol, 2004. 49(12): p. 2657-73.

19. Lopez Medina, A., et al., *Characterization of electron contamination in megavoltage photon beams.* Med Phys, 2005. 32(5): p. 1281-92.

20. Tillikainen, L., et al., *Determination of parameters for a multiple-source model of megavoltage photon beams using optimization methods.* Phys Med Biol, 2007. 52(5): p. 1441-67.

21. Li, X.A. and D.W. Rogers, *Reducing electron contamination for photon beam-quality specification.* Med Phys, 1994. 21(6): p. 791-7.

22. Sjogren, R. and M. Karlsson, *Electron contamination in clinical high energy photon beams.* Med Phys, 1996. 23(11): p. 1873-81.

23. Rogers, D.W., *Correcting for electron contamination at dose maximum in photon beams.* Med Phys, 1999. 26(4): p. 533-7.

24. Mellenberg, D.E., Jr., *Determination of build-up region over-response corrections for a Markus-type chamber.* Med Phys, 1990. 17(6): p. 1041-4.

25. Mackie, T.R., J.W. Scrimger, and J.J. Battista, *A convolution method of calculating dose for 15-MV x rays.* Med Phys, 1985. 12(2): p. 188-96.

26. Sharpe, M.B. and J.J. Battista, *Dose calculations using convolution and superposition principles: the orientation of dose spread kernels in divergent x-ray beams.* Med Phys, 1993. 20(6): p. 1685-94.

27. Ahnesjo, A., et al., *Beam modeling and verification of a photon beam multisource model.* Med Phys, 2005. 32(6): p. 1722-37.

28. Yorke, E.D., C.C. Ling, and S. Rustgi, *Air-generated electron contamination of 4 and 10 MV photon beams: a comparison of theory and experiment.* Phys Med Biol, 1985. 30(12): p. 1305-14.

CHAPTER FOUR: INVESTIGATION OF THE SPATIAL RESOLUTION OF AN ONLINE DOSE VERIFICATION DEVICE

This chapter is adapted from a manuscript entitled "Investigation of the spatial resolution of an online dose verification device" by Ganiyu Asuni, Daniel Rickey, and Boyd McCurdy" published in Medical Physics 39 (2012) 697 – 1223. In this chapter, the spatial resolution of the COMPASS transmission detector, which describes the ability of the device to accurately measure complex IMRT fields, was investigated.

4.1 INTRODUCTION

Patient-specific dose verification is commonly performed to ensure that an intensity modulated radiation therapy (IMRT) treatment plan is accurately delivered [1, 2]. To effectively and independently verify the patient treatment plan, several dose verification methods comparing a pre-calculated radiation dose from the treatment planning system (TPS) to a measurement of the delivered radiation dose without the patient present have been reported [3-8]. Each of these methods has advantages and disadvantages. However, the ideal verification technique is one that is applied during patient treatment by employing either entrance or exit dose measurements. *In vivo* entrance dose measurements, although uncommon in the clinic, are well suited for checking beam characteristics and performance of a treatment device, leaf positioning, and the number of monitor units delivered. Dose verification through entrance fluence

dosimetry has seen increasing research interest [9-11] and corresponds to the introduction of two-dimensional (2D) dosimeters mounted in the head of the clinical linear accelerator. Dosimeters that have been studied include DAVID (PTW-Frieburg, Germany), AIMS (developed by Islam *et al* [9]), and COMPASS transmission detector (IBA Dosimetry, Germany). A major concern for these devices is that their large pixel size will blur the measurement of the incident IMRT fluence. It is well known that the spatial resolution of a multi-element detector is limited by the size and spacing of individual detector elements [12]. A large detector element and a large spacing will result in poor resolution. Since IMRT fluence is characterized by sharp dose gradients between critical organs and target volumes, the measured dose distribution will not represent the true photon fluence delivered and may be unsuitable for the patient-specific dose verification process. Thus for accurate dose verification of IMRT fluence, the performance of these devices needs to be well understood before clinical use. In this work we characterize the spatial resolution of a transmission detector (TRD) by measuring its line spread function (LSF). The resulting detector response function (DRF) is used to predict the measured fluence from the calculated dose.

Previous studies characterizing dose verification devices have included measurements of the modulation transfer function (MTF), as well as signal-to-noise ratio, and detector quantum efficiency [12-15]. Poppe *et al* [12] measured the LSF of a single chamber in a 27 x 27 ionization chamber array (2D-ARRAY Type 10024 - PTW-Frieburg, Germany) and found a limiting (pre-sampling) resolution of 0.153 mm^{-1}. The authors also showed that sampling frequency of 0.1 mm^{-1} was not sufficient for a typical

IMRT field. Herzen *et al* (2007) investigated the dosimetric properties of a similar detector (MatriXX - IBA Dosimetry, Germany) containing 32 x 32 cylindrical chambers of 4 mm diameter with 7.6 mm spacing between chamber centers. They obtained the LSF using a 1 mm slit shifted across the device [15]. By convolving, the LSF with a TPS calculated dose distribution they found good agreement with measured dose distributions of IMRT plans and concluded that the device can be used for quality assurance and 2D dose verification. For dose verification, the LSF has been used in two different methods. In the first method, the LSF was convolved either with the calculated dose from the TPS or with measured dose from detectors with negligible-size elements. The resultant dose distribution was then compared to the measured dose [12, 15]. In the second method, the LSF was used in an iterative deconvolution algorithm to obtain a true (blur-free) photon fluence from the measured signal [16]. These studies showed the importance of characterizing new dose verification devices prior to clinical implementation.

In this work, we evaluate the spatial resolution of the COMPASS transmission detector, which was developed for *in vivo* dose verification. Specifically, we measure the LSF of a single detector chamber and validate these measurements with Monte Carlo (MC) calculations. Our validation approach is to convolve the DRF, derived from the measured LSF of the detector; with the incident fluence calculated using the Monte Carlo technique. The result can then easily be compared with entrance dose measured by the detector. By using this technique on two patient IMRT fields, we demonstrate that the detector can be used to verify dose during treatment.

4.2 MATERIALS AND METHODS

4.2.1 Experimental setup for LSF Measurement

The COMPASS transmission detector consists of 1600 plane-parallel ionization chambers, with 3.8 mm diameters, 6.5 mm center-to-center distances, and 0.02 cm^3 active volumes. Prior to measurements, the device was irradiated with a 10 Gy dose using a 40 x 40 cm^2 field size to cover the entire detector array as recommended by the manufacturer [17]. The LSF is the response of the detector to an infinitesimal thin photon beam and is used to characterize the spatial degradation of the input signal by the detector. A related parameter, the MTF is normally used to characterize the spatial resolution of the system. The MTF is the modulus of the Fourier transform of the normalized LSF and is given as:

$$MTF(f) = \left| \int_{-\infty}^{\infty} LSF(x) e^{-2\pi i f x} dx \right| \tag{4.1}$$

where f is spatial frequency and x is the spatial distance.

The LSF of the COMPASS transmission detector was measured as shown in figure 4.1 by collimating a 6 MV photon beam (Varian Clinac 2100ix with Millennium 120-leaf MLC). A narrow slit collimator was formed by two machined 24 x 72 x 152 mm^3 lead (ρ = 11.3 g/cm^3) blocks, containing a milled groove of dimensions 0.25 x 10 x 152 mm^3 (i.e., the slit opening). The couch top was removed and the slit collimator was

suspended underneath. The collimator was held stationary with its exit surface located 5.7 cm above the surface of the transmission detector, which was as close as the setup allowed. The distance between the source and the entrance of the slit collimator was 175.8 cm. To reduce the effect of scattered radiation on the measurement, the secondary jaws and the MLC were used to define 4 x 12 mm^2 and 4 x 20 mm^2 fields at isocenter, respectively. Proper alignment of the slit collimator along the central axis of the beam was a crucial step. Any misalignment would result in a decrease in the fraction of the source that contributed to the x-ray fluence passing through the slit.

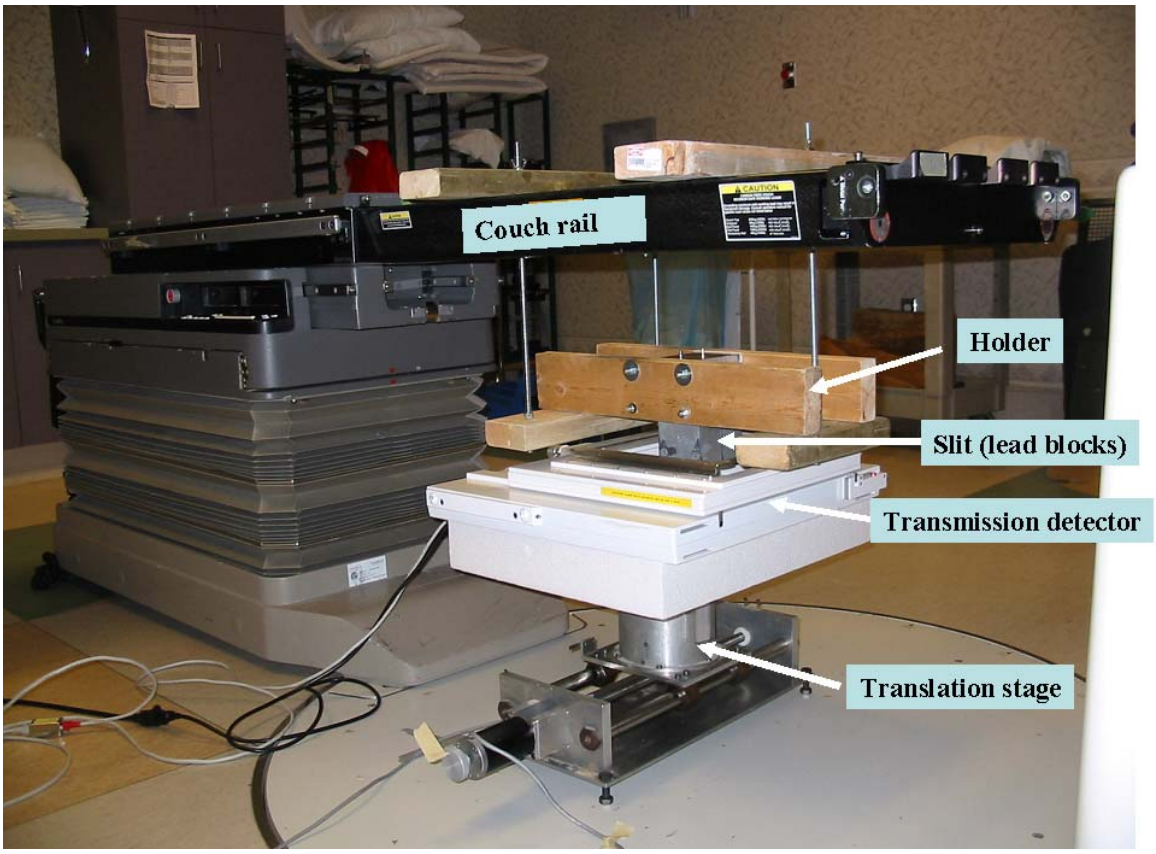


Figure 4-1: The experimental set up used for measuring the LSF of the transmission

detector. The slit collimator with an opening of 0.25 x 10 x 152 mm^3 was suspended underneath the couch and held stationary above the TRD. The three threaded rods allowed adjustment of the slit collimator angle.

For accurate alignment of the slit along the central axis of the beam, rotation and translation of the slit collimator and detector were performed as follows:

a. The room laser was used to coarsely align the slit collimator with the central axis of the beam. A precision bubble level was used to level the slit collimator. Then a high-intensity diode flashlight was placed under the slit collimator to project light onto the exit window of the linac. The slit angle was adjusted so the projected light was centered on the field light.
b. A piece of GafChromic EBT2 film (International Specialty Products, Wayne, NJ) was placed on the entrance of the slit and the film was marked at a point corresponding to the slit opening, and then irradiated with 500 MU at 600 MU/min. After irradiation, the position of the irradiated portion of the film was compared to the position of the marked line. The slit was then translated by the difference of these positions. The process was repeated until the slit was properly centered in the radiation field.
c. To confirm alignment, a second film was placed under the slit collimator and the film was irradiated with 5000 MU at 600 MU/min. If the slit was properly aligned a slit image would be seen on the irradiated film otherwise a blank film would be observed.
d. After aligning the slit collimator, the detector was placed on an in-house developed translation stage as shown in figure 4.1. The bubble level was used to check that the TRD was level.

e. Initial detector alignment was performed using the manufacturer alignment marks on the TRD and the room laser. It was necessary to centre a detector chamber longitudinally with the slit opening by irradiating the detector with 500 MU of dose several times and translating the detector until the position with maximum signal was obtained.

f. A final alignment of the collimator was made by rotating the slit a very small angle in the gantry rotation plane and then irradiating the TRD with a dose of 500 MU. This procedure was repeated several times until a maximum signal was measured by the TRD.

The translation stage was driven by a stepper motor (STEVAL-SPMD250V1 STMICROELECTRONICS, Geneva) controlled by software PractiSPIN^{TM} installed on a Netbook computer. The accuracy of the linear stage was verified with a dial indicator and found to be within 0.3%. After alignment, the detector was translated in 0.25 mm steps across the slit collimator. Data were acquired at 96 different positions corresponding to 24 mm, which allowed us to obtain the LSFs for three neighbouring chambers. All measurements were corrected for background and leakage. Before translating the detector, Gafchromic EBT2 film was placed at the exit of the slit to obtain the size of the beam at the detector. The film was irradiated with 5000 MU at 600 MU/min. The irradiated film was scanned on a flatbed scanner with a 600 dpi resolution (Microtek). The image was imported and analyzed in ImageJ [18].

4.2.2 Monte Carlo simulation and calculation of LSF

To further characterize the detector, we performed Monte Carlo (MC) studies of the response function.

4.2.2.1 Calculation of the film response function

BEAMnrc/EGSnrc Monte Carlo code [19] was used to model the head of the linear accelerator based on a detailed description provided by the manufacturer for the 6 MV photon beam. This model has been previously validated [20] and found to be accurate. For this work, two phase-space files were obtained as shown in figure 4.2. Each phase space file contained a complete description of every particle that reached the scoring plane, including the position, energy, angle, charge, direction cosine and weight of the particles. The first phase-space file was obtained at the entrance plane of the slit collimator, placed 175.8 cm distance away from the source. The second phase-space file was obtained at the exit plane of the slit collimator, located at a 191.0 cm source-to-surface distance (SSD). The first phase-space file was used as an input source in the DOSXYZnrc/EGSnrc calculation of film response to the thin slit collimator. The DOSXYZnrc calculation included the geometry of the slit collimator, the air gap between the exit of the slit collimator and the transmission detector, and the Gafchromic EBT2 film properties. The GafChromic EBT2 film was described in DOSXYZnrc using the geometry and material specifications reported in the literature [21]. The dose deposited in

the active layer of the film was scored in 0.30 x 0.30 x 0.03 mm^3 voxels. The secondary jaws and the MLC-defined fields used in the experimental setup described in section 4.2.1 were also used in the BEAMnrc simulation. For the BEAMnrc simulation and DOSXYZnrc calculation, $1x10^{10}$ incident electrons on the target were simulated, and the electron energy cutoff (ECUT) and photon energy cutoff (PCUT) were set to 0.521 MeV and 0.010 MeV respectively. The PRESTA-II electron step algorithm and the EXACT boundary crossing algorithm were used; directional bremsstrahlung splitting was used, while Russian roulette for secondary electrons was turned off.

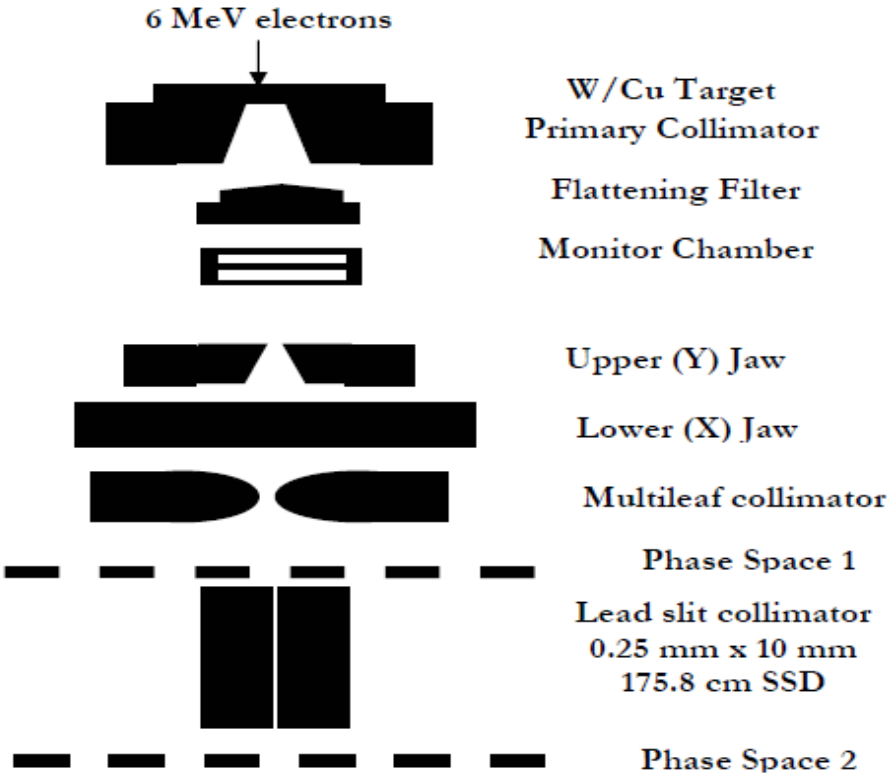


Figure 4-2: Schematic representation of the linear accelerator head geometry used for

simulating the detector response function in BEAMnrc. Phase space files were obtained at two different scoring regions, i.e., the entrance and exit surfaces of the slit collimator at 175.8 and 191.0 cm SSD, respectively.

4.2.2.2 Calculation of the TRD line spread function

Unfortunately, the DOSXYZnrc user code was unable to score dose in a circular region. Thus, the *reciprocity theorem* was used to simulate the measured response function for a single circular detector. The reciprocity theorem for radiation transport states that the source and the detector geometry may be interchanged without altering the dose measured provided both are parts of an infinite homogeneous medium [22]. The use of this theorem allowed us to perform a single simulation of the entire detector response curve instead of a simulation for each point on the curve. For this calculation, we used a circular source of photons incident on a three-layer model of the TRD [Ref. 20] with a linear array of voxels in the sensitive layer of the TRD. This is equivalent to a rectangular source and a circular detector. Since a circular source option is not available, we modified the DOSXYZnrc source code (i.e., *srcxyznrc.mortran*) to define a circular source with an adjustable beam radius and direction cosines of particles, with the option of using a user-defined energy spectrum. A 3.8 mm diameter circular source (the size and shape of a single detector) with a typical full photon energy spectrum was used for the calculation of the TRD's LSF. Then dose was scored in the TRD detector elements in voxels with size similar to the slit opening (i.e., 0.25x10 mm^2) using DOSXYZnrc. The energy spectrum

of the particles in the second phase-space file was scored using the BEAMDP/EGSnrc user code in 250 keV wide bins.

4.2.2.3 Calculation of the LSF for an ideal circular detector

The general expression for the LSF of an ideal, assuming a homogeneous circular detector has been described by Garcia-Vicente *et al* [23] as follows:

$$K(x) = \begin{cases} \dfrac{(R^2 - x^2)^{1/2}}{\pi R^2}, & |x| \le R \\ 0, & |x| > R \end{cases} \tag{4.2}$$

where K(x) is the LSF, x is the position, and R is the detector radius.

The ideal LSF for a single chamber in the TRD was calculated using equation 4.2 with a detector radius of 1.9 mm. This was compared to the measured and MC calculated LSF.

4.2.3 Validation of the measured LSF and detector response function

Due to the finite diameter of the detectors in the array, a measured dose pattern will not exactly represent the actual delivered dose. This phenomenon has been called the detector size effect and is a major perturbation in ion chamber dosimetry [24, 25]. This effect is considerably reduced for detectors with small elements such as diodes, films,

and electronic portal imaging devices (EPIDs). However, if all detector elements have the same size, the measured dose, $D_m(x,y)$, is represented as a convolution of the true dose with the response function of a detector element.

$$D_m(x,y) = F_a(x,y) * DRF(x,y) \tag{4.3}$$

where $F_a(x,y)$ is the true incident fluence and DRF(x,y) is the detector response function. Thus, by knowing the DRF, the output of the detector can be compared to the calculated dose.

There are different methods of computing the DRF from the measured LSF, including solving an integral equation or using Fourier transforms [26, 27]. In our case, we used a Fourier method because solving the integration equation could be very complex and introduce additional uncertainties into the results. First, the optical transform (OTF) was calculated from the Fourier transform of the LSF i.e., MTF

$$MTF(u) = \left| \int_{-\infty}^{\infty} LSF(x, \theta = 0) e^{-2\pi i u x} dx \right| = \left| \mathrm{OTF(u)} \right| \tag{4.4}$$

Assuming radial symmetry this one dimension OTF (u) was spatially mapped onto a two-dimension matrix to obtain a 2D OTF (u,v). Then the detector response function DRF(x,y) was calculated from the inverse Fourier transform of the 2D OTF (u,v).

$$OTF(u) \Rightarrow OTF(u,v) \tag{4.5}$$

$$DRF(x,y) = \int_{-\infty}^{\infty}\int_{-\infty}^{\infty} OTF(u,v)e^{+2\pi i(ux+vy)}dudv \quad (4.6)$$

To confirm the suitability of equation 4.3, two clinical head and neck IMRT fields were measured with the TRD and also simulated using BEAMnrc MC code. These were sliding-window fields with 119 and 149 control points, generated in the Eclipse Treatment Planning System (Varian Medical Systems, Palo Alto, CA). Data acquisition was performed using the COMPASS software that accompanied the TRD and data analysis was implemented in MATLAB (MathWorks, Natick, MA). Simulations were performed with the BEAMnrc code using the DYNVMLC component module [28], which modeled the geometry of the Varian Millennium 120 leaf collimator and allowed sampling of the leaf sequence file (MLC Shaper file) during the simulation of IMRT delivery. Validating the measurement was performed in two steps.

a. *Step 1:* In the first step, the accuracy of the MC simulation was verified by comparing the dose patterns measured by the TRD (D_{meas}^{TRD}) to the MC calculated dose distributions (D_{calc}^{TRD}) of the same IMRT fields. To validate the incident fluence scored in the BEAMnrc simulation of the IMRT fields, the scored phase-space files of the incident fluences of the two clinical IMRT fields were used as a source in the DOSXYZnrc user code to calculate the dose delivered to the TRD. The doses scored in 1600 square voxels of 3.4 x 3.4 mm^2, i.e., the equivalent area to the 3.8 mm diameter chambers, were compared to the measured doses using a χ comparison, with a dose difference (DD) criteria of 3 % and a distance-to-agreement (DTA) criteria of 3 mm. The χ comparison [29] is a fast, quantitative evaluation method to compare

dose distributions, and is a computationally efficient implementation of the γ - evaluation concept [30].

b. *Step 2:* In the second step, equation 4.3 was verified by comparing the dose pattern measured by the TRD (D_{meas}^{TRD}) to the calculated dose obtained from the convolution of the 2D detector response with the incident fluence from the MC simulation ($D_{calc,R}^{TRD}$). Figure 4.3 illustrates how the measured and calculated dose distributions were compared. The incident fluence scored in the plane of the measured IMRT fields (i.e. 65 cm) was obtained at high resolution (i.e. 0.46 x 0.46 mm^2) using the BEAMDP user code. This incident fluence was then convolved with the 2D detector response, *DRF(x,y)*. The resultant dose distribution was resampled to the pixel size of the TRD chambers. Then the in-field pixels (as defined by a threshold of 10 % of maximum dose) of the calculated and measured dose distributions were evaluated using the χ - comparison of 3 %/3 mm.

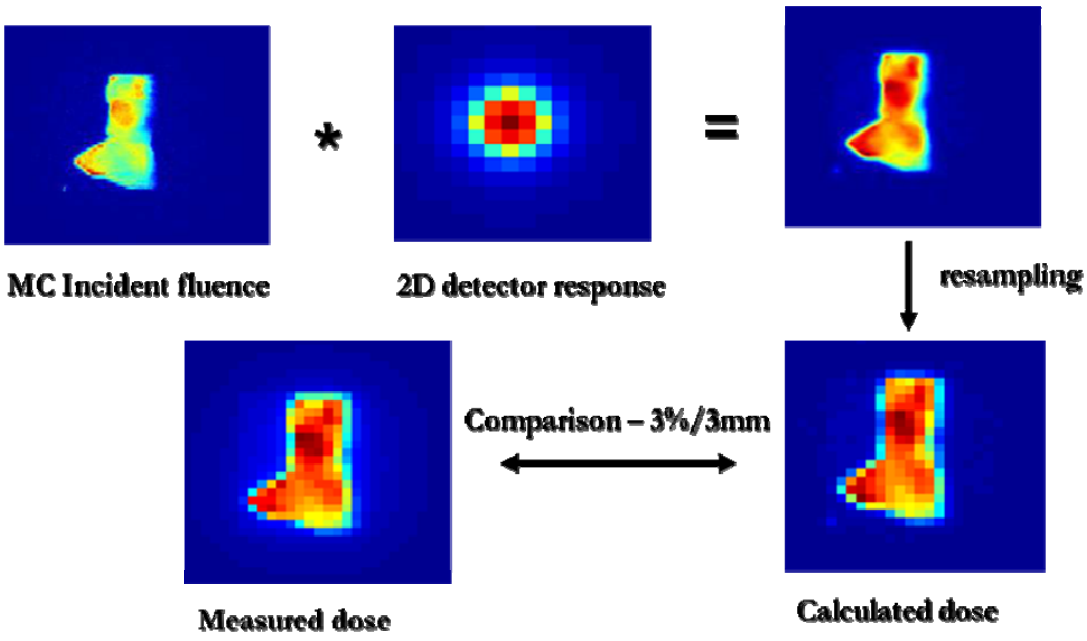


Figure 4-3: An overview of the method of comparing measured and calculated dose distributions of the IMRT fields. The calculated dose is a convolution of the Monte Carlo generated incident fluence and the measured 2D detector response

4.3 Results and Discussion

4.3.1 Measured and calculated response function

The narrow photon beam exiting the slit collimator was measured with Gafchromic EBT2 film and is plotted in figure 4.4. Also shown is the calculation of the film response performed in DOSXYZnrc. Both profiles are normalized to their maximum values. There is qualitative agreement between the measured and calculated responses of

the film, except for fluctuations in the tail region of the measured data, which may be attributed to a non-uniform background (base) in the film and could have been removed if we had pre-scanned the film before measurement. The full-width half-maximum (FWHM) was found to be 0.28 mm for the measurement and 0.26 mm for the MC calculation. These compare very well with the slit width of 0.25 mm. These results also indicate that the slit opening was well aligned with the beam.

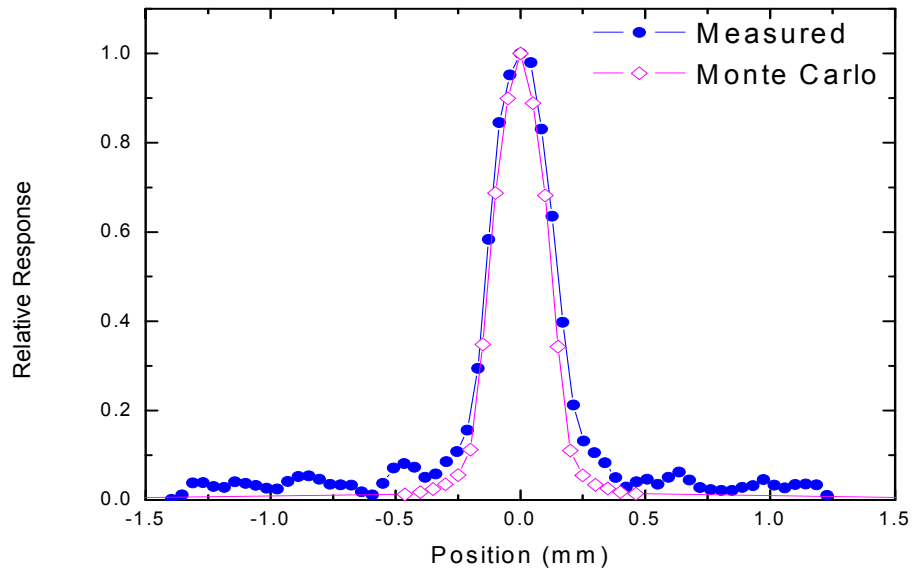


Figure 4-4: The width of the collimated photon beam as measured by Gafchromic EBT2 film and predicted by MC simulation.

All chambers in the TRD are the same size and are, therefore, expected to have the same measured LSFs. Figure 4.5, shows the absolute response measured for three adjacent chambers in the TRD. As expected figure 4.6, shows little difference in the

individual responses. Figure 4.7 shows the measured LSF of a single chamber in the transmission detector, the theoretical response of a 3.8 mm diameter ideal circular photon detector, and the MC calculated LSF. The profile of the measured LSF has a peak at the center of the detector with small over-responses near the chamber edges. The ideal detector response ignores the effect of secondary electrons, which if present would result in the broadening of the response. Aside from ignoring the secondary electrons, the ideal detector demonstrates good agreement within the physical limits of the detector (i.e. 3.8 mm diameter). The FWHM of the measured detector response is 4.3 mm which is comparable to the chamber diameter of 3.8 mm. The MC calculated LSF shows qualitative agreement with the measured data in the central region of the chamber. However, there is an over-response in the measurement near the chamber wall compared to the MC calculation that shifts the edges outwards by approximately 0.25 mm. This over-response on the edges suggests that the sensitive volume of an individual chamber cannot be modeled as a perfectly uniform cylinder.

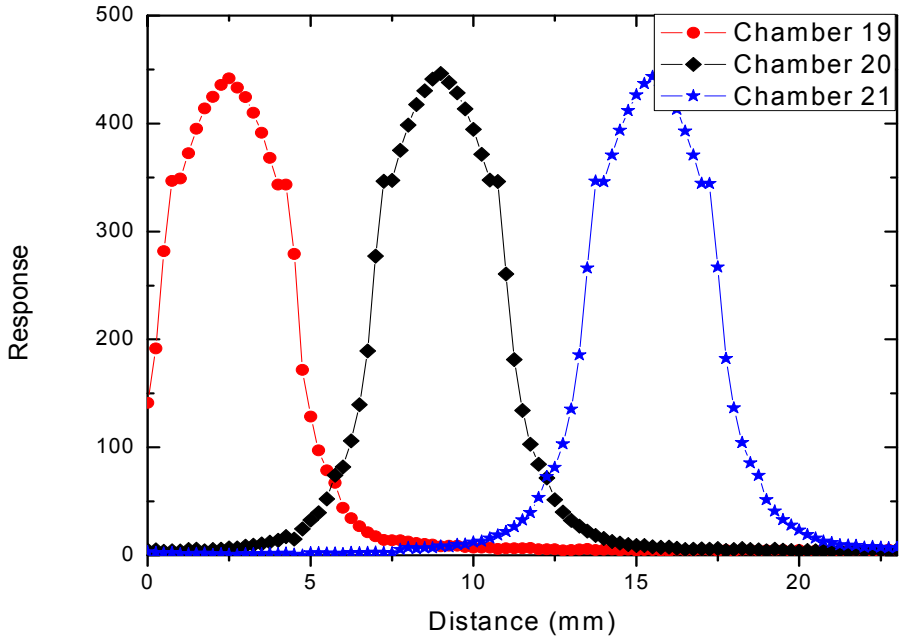


Figure 4-5: The LSF for three adjacent chambers in the transmission detector. The chambers are in row 21 of the TRD.

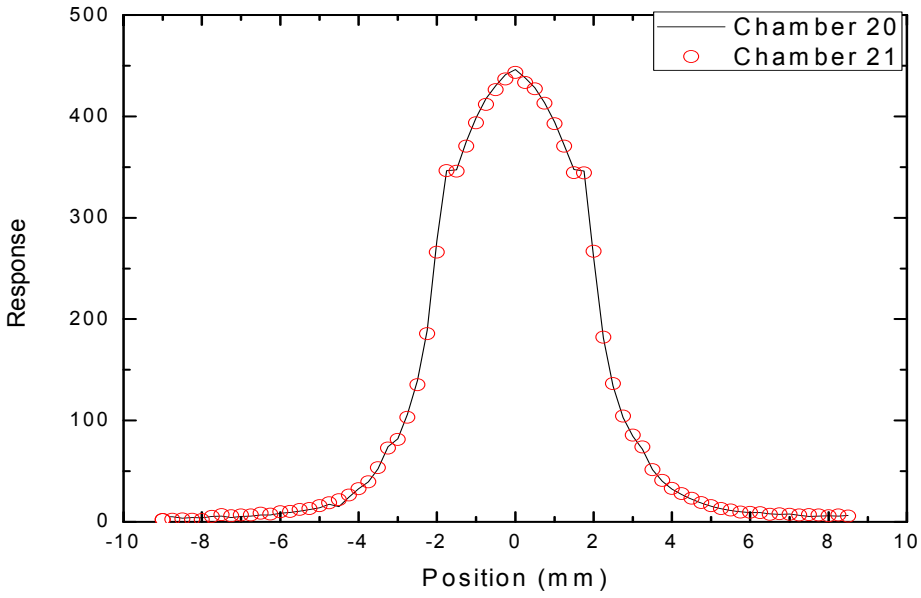


Figure 4-6: The LSFs of two adjacent chambers in the transmission detector are overlaid.

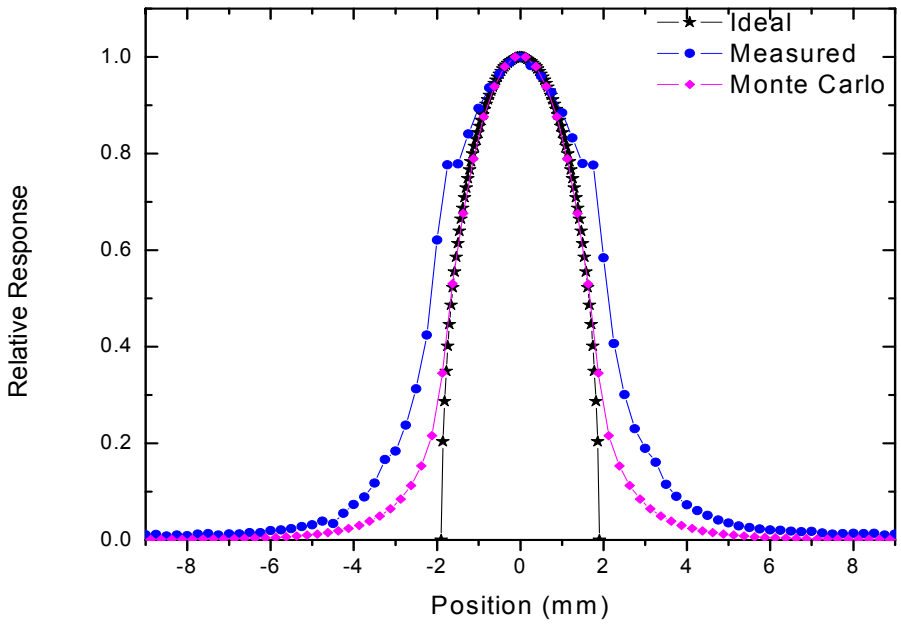


Figure 4-7: Plot showing the measured LSF of one chamber of the TRD, the MC calculated response function, and the ideal response of a cylindrical detector of 3.8 mm diameter.

The measured modulation transfer functions were calculated for the measured, MC calculated and ideal LSFs and are shown in figure 4.8. For an ideal circular detector the expected MTF is related to a Bessel function. The first zero crossings of the MTFs occur at frequencies of 0.25 mm^{-1}, 0.31 mm^{-1}, and 0.31 mm^{-1} for the measured, MC calculated, and ideal responses respectively. For the MC data the first zero crossing is similar to that of the ideal case but the theoretical MTF has a higher modulation transfer. Although the measured MTF has its first zero crossing at 0.25 mm^{-1}, a chamber spacing

of 6.5 mm results in aliasing of frequencies above 0.077 mm^{-1}. Data published by Poppe *et al*. [12] suggest that an IMRT field can contain frequencies up to at least 0.15 mm^{-1} at an SDD of 65 cm. Thus, aliasing artifacts are expected and future detector designs will require a smaller chamber separation. Though the TRD is a segmented detector, the MTF measurement is valid because the chambers are centered on a uniform grid and are calibrated to have equivalent responses [31].

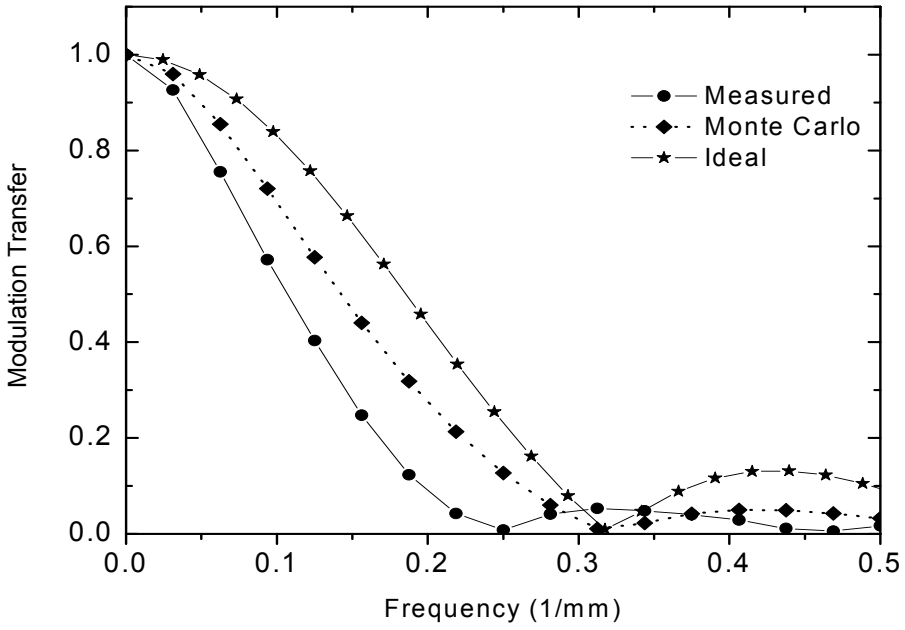


Figure 4-8: The measured, MC calculated and ideal pre-sampling modulation transfer functions (MTF) for a single chamber in the transmission detector.

4.3.2 Effect of the detector response function

The calculated detector response function is plotted in figure 4.9. For reference, the LSF is also shown. It can be seen that the chamber is slightly more sensitive at its wall and this is due to the edge enhancement of the chamber's sensitive volume.

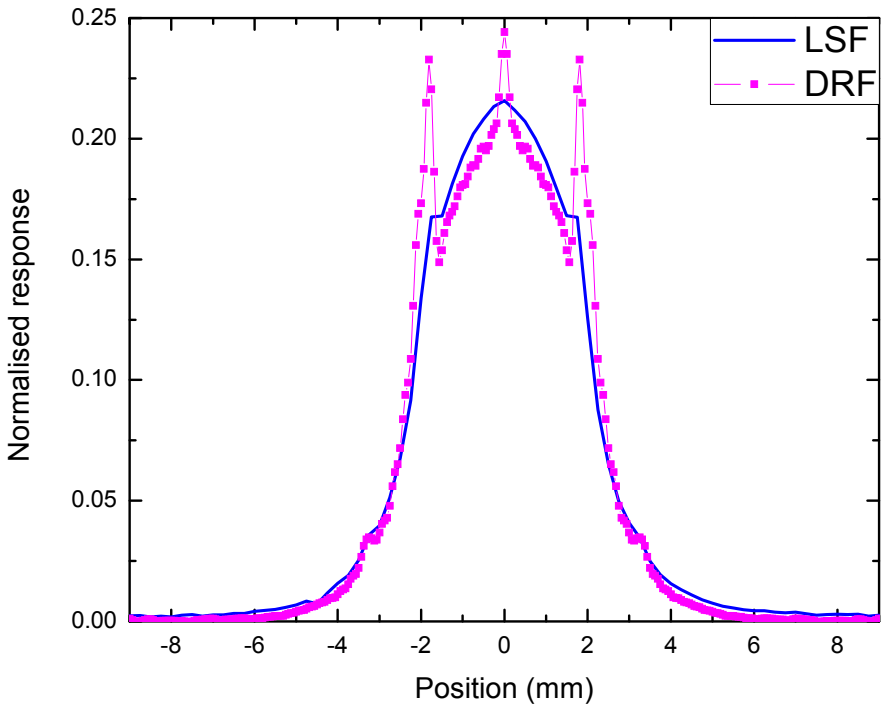


Figure 4-9: The detector response function (DRF) normalized to unit area of a single chamber in the transmission detector. The LSF is shown for reference.

Figure 4.10 shows the results of step 1 as described in section 4.2.3, it contains the measured and calculated profiles in the in-plane and cross-plane directions through the dose distributions. There is qualitative agreement between profiles of the measured

(D_{meas}^{TRD}) and calculated doses (D_{calc}^{TRD}). The relative statistical uncertainty for the MC calculated dose for in-field voxels is estimated to be <0.5% of the maximum dose value. The maximum dose difference is less than 3%. Figure 4.11 shows the results of the χ-comparison between the calculated and measured IMRT dose distributions for field 1 using criteria of 3% and 3 mm. It shows very good agreement between the measured and calculated dose with 99.0% of pixels having χ <1 for IMRT field 1. Similarly, we found good agreement between measured and calculated dose for IMRT field 2 with 99.5% of pixels having χ <1. These results establish that the simulation of incident IMRT fluence in BEAMnrc and subsequent dose calculation in DOSXYZnrc of the IMRT field are accurate within an acceptable tolerance.

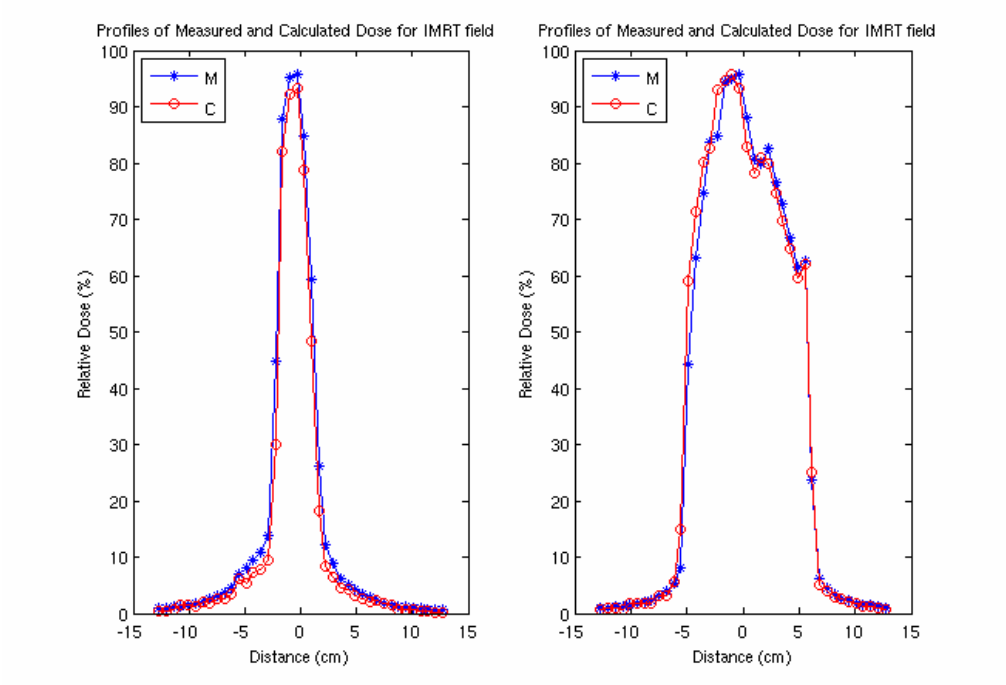


Figure 4-10: The in–plane (left) and cross–plane (right) profiles through the central axis of the measured and directly calculated dose in DOSXYZnrc for IMRT field 1.

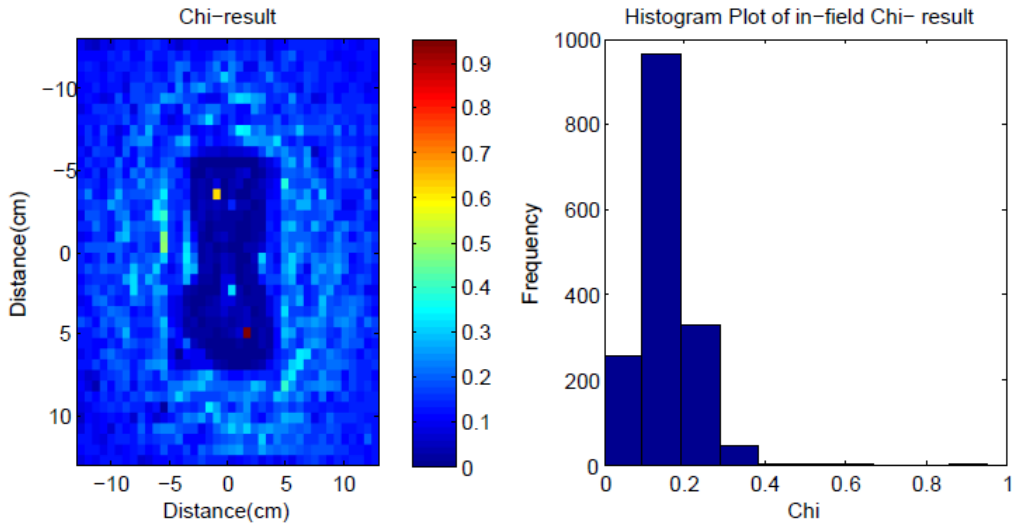


Figure 4-11: Image (left) showing a χ -comparison result between the measured and calculated dose distributions. A histogram plot (right) of in-field χ -comparison result for IMRT field 1.

The results of step 2, i.e., validation of equation 4.3, for IMRT field 1 are given in figure 4.12. The χ comparison results show good agreement between measured and calculated dose for both IMRT fields. We found that 95.1 % and 96.3 % of in-field pixels for field 1 and 2 respectively demonstrate $\chi < 1$ (with average χ of 0.29 for IMRT field 1 and 0.24 for IMRT field 2). However, for the entire detector array (in-field and out-of-field) we observed that 98.6% and 99.0% of pixels have $\chi <1$ for IMRT field 1 and IMRT field 2 respectively. These relatively small disagreements were mostly at the field edges just outside the 10% dose threshold. It is worth mentioning that while the tail region of the dose profiles shown in Figure 4.10 show qualitative agreement, the same region in the

dose profiles shown in figure 4.12 has relatively small disagreement. This observed disagreement may be due to low fluence in the small scoring regions (0.46 mm) used in BEAMDP.

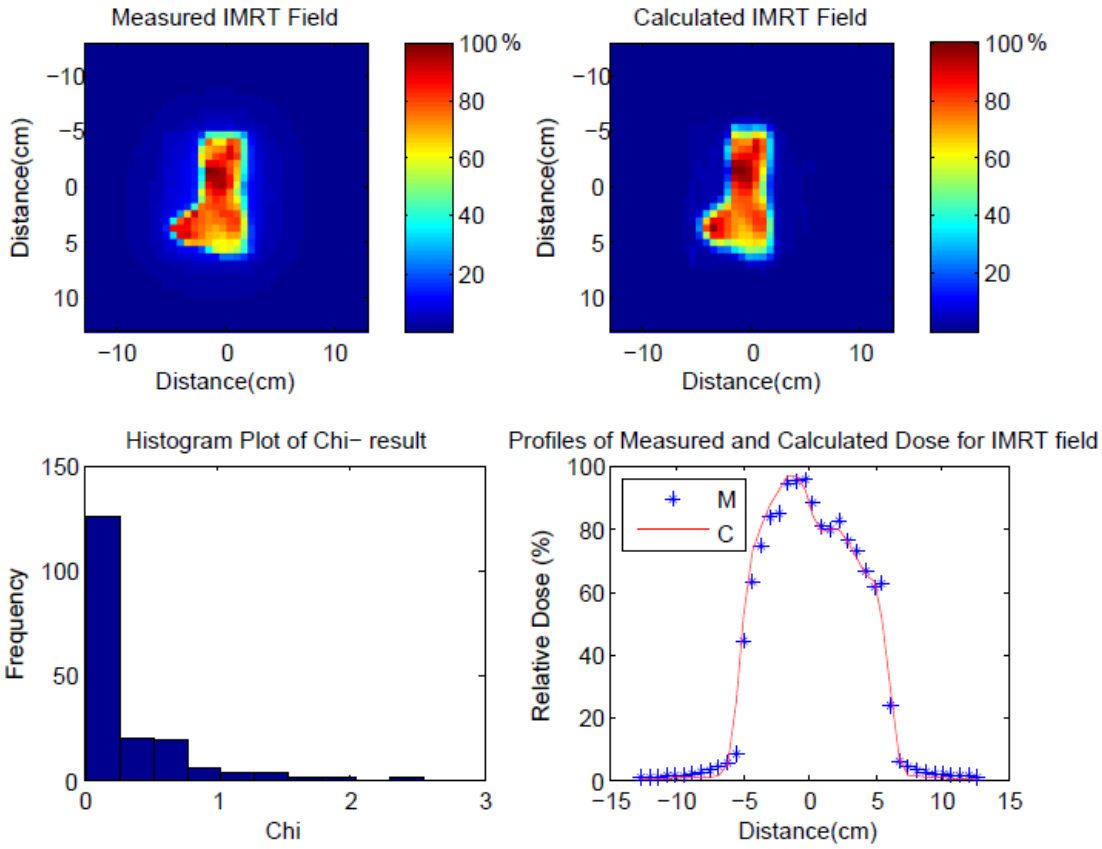


Figure 4-12: Measured (M) and calculated (C) dose for a head and neck, sliding window, IMRT field 1 with 119 control points (top panels). The histogram plot of in-field χ-comparison result (bottom left panel) and the horizontal profiles of measured and calculated dose (bottom right panel).

4.4 Conclusions

The LSF and DRF for a novel online transmission detector (TRD) have been measured for a 6 MV photon beam using a narrow slit collimator. The narrow photon beam exiting the slit collimator was verified using MC calculations and GafChromic EBT2 film. The FWHM of measured and calculated profiles were 0.28 mm and 0.26 mm respectively, which compare well with the slit width of 0.25 mm. The LSF was measured for a single chamber in the TRD and compared to the MC calculated and the ideal response of a perfect cylindrical detector. While the ideal response ignored the effect of secondary electrons, the MC results showed qualitative agreement with the measured LSF with the exception of a small over response at the edges of the chamber, which broadened the FWHM by about 0.5 mm. The resulting DRF showed a region of enhanced sensitivity near the chamber walls. The measured MTF was calculated and the limiting resolution was estimated as 0.25 mm^{-1} from the first zero crossing. The chamber separation gives a sampling frequency of 0.154 mm^{-1} with a Nyquist limit of 0.077 mm^{-1}. Thus the TRD is capable of reproducing the dose distribution of complex IMRT fields but the large sampling distance (6.5 mm) may result in under-sampling of IMRT fields with high frequency contents. The effect of the DRF was validated by comparing the measured dose in the TRD array with the result of the convolution of the DRF and the incident fluence. This was done for two clinical, sliding window, head and neck IMRT fields. The calculated and measured dose for two IMRT fields compared well, with more than 95 % of in-field points satisfying $\chi<1.0$. These results have shown that the DRF of

the TRD was accurately measured and would be useful for independent dose verification of patient treatment plans. In addition, from the comparison of the measured and calculated dose it has been shown that the detector measures IMRT fields accurately within acceptable tolerance. However, future designs require more closely spaced ion chambers.

4.5 Bibliography

1. van Elmpt, W.J., et al., *Treatment verification in the presence of inhomogeneities using EPID-based three-dimensional dose reconstruction.* Med Phys, 2007. 34(7): p. 2816-26.
2. Low, D.A., et al., *Dosimetry tools and techniques for IMRT.* Med Phys, 2011. 38(3): p. 1313-1338.
3. Leunens, G., et al., *Quality assurance in radiotherapy by in vivo dosimetry. 1. Entrance dose measurements, a reliable procedure.* Radiother Oncol, 1990. 17(2): p. 141-51.
4. Low, D.A., et al., *Quantitative dosimetric verification of an IMRT planning and delivery system.* Radiother Oncol, 1998. 49(3): p. 305-16.
5. Quach, K.Y., et al., *Measurement of radiotherapy x-ray skin dose on a chest wall phantom.* Med Phys, 2000. 27(7): p. 1676-80.
6. Jursinic, P.A., *Implementation of an in vivo diode dosimetry program and changes in diode characteristics over a 4-year clinical history.* Med Phys, 2001.

28(8): p. 1718-26.

7. Bucciolini, M., F.B. Buonamici, and M. Casati, *Verification of IMRT fields by film dosimetry.* Med Phys, 2004. 31(1): p. 161-8.

8. Chen, J., et al., *Calibration of an amorphous-silicon flat panel portal imager for exit-beam dosimetry.* Med Phys, 2006. 33(3): p. 584-94.

9. Islam, M.K., et al., *An integral quality monitoring system for real-time verification of intensity modulated radiation therapy.* Med Phys, 2009. 36(12): p. 5420-8.

10. Poppe, B., et al., *Clinical performance of a transmission detector array for the permanent supervision of IMRT deliveries.* Radiother Oncol, 2010. 95(2): p. 158-65.

11. Venkataraman, S., et al., *The influence of a novel transmission detector on 6 MV x-ray beam characteristics.* Phys Med Biol, 2009. 54(10): p. 3173-83.

12. Poppe, B., et al., *Spatial resolution of 2D ionization chamber arrays for IMRT dose verification: single-detector size and sampling step width.* Phys Med Biol, 2007. 52(10): p. 2921-35.

13. Cremers, F., et al., *Performance of electronic portal imaging devices (EPIDs) used in radiotherapy: image quality and dose measurements.* Med Phys, 2004. 31(5): p. 985-96.

14. Falco, T. and B.G. Fallone, *Characteristics of metal-plate/film detectors at therapy energies. I. Modulation transfer function.* Med Phys, 1998. 25(12): p. 2455-62.

15. Herzen, J., et al., *Dosimetric evaluation of a 2D pixel ionization chamber for*

implementation in clinical routine. Phys Med Biol, 2007. 52(4): p. 1197-208.

16. Looe, H.K., et al., *Enhanced accuracy of the permanent surveillance of IMRT deliveries by iterative deconvolution of DAVID chamber signal profiles.* Phys Med Biol, 2010. 55(14): p. 3981-92.
17. *COMPASS User's Guide version P-05-008-510-001 03.* (IBA Dosimetry, Schwarzenbruck, Germany).
18. Rasband, W., *ImageJ. US National Institutes of Health, Bethesda, Maryland*. 1997.
19. Rogers, D.W., et al., *BEAM: a Monte Carlo code to simulate radiotherapy treatment units.* Med Phys, 1995. 22(5): p. 503-24.
20. Asuni, G., J.M. Jensen, and B.M. McCurdy, *A Monte Carlo investigation of contaminant electrons due to a novel in vivo transmission detector.* Phys Med Biol, 2011. 56(4): p. 1207-23.
21. Aldelaijan, S., et al., *Evaluation of EBT-2 model GAFCHROMIC film performance in water.* Med Phys, 2010. 37(7): p. 3687-93.
22. Attix, F.H., *Introduction to radiological physics and radiation dosimetry.* 1986.
23. Garcia-Vicente, F., J.M. Delgado, and C. Peraza, *Experimental determination of the convolution kernel for the study of the spatial response of a detector.* Med Phys, 1998. 25(2): p. 202-7.
24. Das, I.J., G.X. Ding, and A. Ahnesjo, *Small fields: nonequilibrium radiation dosimetry.* Med Phys, 2008. 35(1): p. 206-15.
25. Martens, C., C. De Wagter, and W. De Neve, *The value of the PinPoint ion chamber for characterization of small field segments used in intensity-modulated*

radiotherapy. Phys Med Biol, 2000. 45(9): p. 2519-30.

26. Marchand, E., *Derivation of the point spread function from the line spread function.* JOSA, 1964. 54(7): p. 915-919.

27. Marchand, E., *From line to point spread function: the general case.* JOSA, 1965. 55(4): p. 352-352.

28. Heath, E. and J. Seuntjens, *Development and validation of a BEAMnrc component module for accurate Monte Carlo modelling of the Varian dynamic Millennium multileaf collimator.* Phys Med Biol, 2003. 48(24): p. 4045-63.

29. Bakai, A., M. Alber, and F. Nusslin, *A revision of the gamma-evaluation concept for the comparison of dose distributions.* Phys Med Biol, 2003. 48(21): p. 3543-53.

30. Low, D.A. and J.F. Dempsey, *Evaluation of the gamma dose distribution comparison method.* Med Phys, 2003. 30(9): p. 2455-64.

31. Sawant, A., et al., *Segmented crystalline scintillators: an initial investigation of high quantum efficiency detectors for megavoltage x-ray imaging.* Med Phys, 2005. 32(10): p. 3067-83.

CHAPTER FIVE: A Monte Carlo tool for evaluating VMAT and DIMRT treatment deliveries including planar detectors

This chapter is adapted from a manuscript entitled "A Monte Carlo tool for evaluating VMAT and DIMRT treatment deliveries including planar detectors" by Ganiyu Asuni, Timothy van Beek, Sankar. Venkataraman, Antoniu Popescu, and Boyd McCurdy" published in Physics in Medicine and Biology 58 (2013) 3535 – 3550. The work in this chapter describes and validates a novel Monte Carlo simulation tool that provides both the calculated dose to an arbitrary planar detector and the calculated dose to the patient or phantom data set, for individual gantry angle fluences of VMAT treatment delivery

5.1 Introduction

The clinical use of volumetric modulated arc therapy (VMAT) has increased rapidly since it became commercially available in 2009. A VMAT treatment plan is defined by a series of individual control points (CP), each having an associated dose rate, multi-leaf collimator (MLC) position, and gantry position. Dynamic intensity modulated radiation therapy (DIMRT) is similar, but without the gantry angle rotation aspect. Commissioning and quality assurance (QA) procedures for VMAT that verify the accuracy of leaf positions during delivery, the accuracy of gantry speed and position, as well as dose output of the linear accelerator (i.e. linac) at varying dose rates have been developed [1-4] and are widely used. The procedure for patient specific dose verification

of VMAT treatment plans is still evolving and most current methods are adapted from those used for conventional IMRT [5-9]. However, the time-varying nature of VMAT techniques introduces additional challenges to verification of patient treatment plans. Monitoring the time-dependent (or equivalently, gantry angle dependent) fluence output of the linac offers some advantages over purely composite plan verification (i.e. total plan verification at a fixed gantry angle). For example, planar dose arrays may be utilized to measure the time-dependent fluence delivered by the linac, and these fluences may then be used to reconstruct a three-dimensional dose estimate in a patient representation (i.e. CT simulation data set). Planar dose arrays are widely available from several vendors [10-12]. Electronic portal imaging devices (EPIDs) have also been shown to be useful for this application [13]. Furthermore, time-dependent fluence verification provides more data with which to diagnose any observed treatment verification errors [14] .

The use of a pre-treatment dose verification approach in quality assurance programs for VMAT and DIMRT treatment plans is currently a clinical mainstay. However, there is growing interest in the use of quality assurance methods that are more relevant to the actual patient treatment, that is, performing verification measurements of fluence during treatment delivery with a phantom (i.e. more realistic than an open field delivery) or a patient (i.e. *in vivo* dosimetry) present in the treatment beam. There are several reports in the literature describing the use of a-Si EPIDs for *in vivo* patient dosimetry (see the review paper by [13], and more recently [15, 16]). In addition, commercial systems such as DAVID (PTW-Freiburg, Germany), AIMS (developed by [10]), and the COMPASS transmission detector (IBA Dosimetry, Germany) as entrance

dosimeters are becoming available for this purpose.

Multi-purpose Monte Carlo (MC) codes such as EGSnrc have been used as independent verification tools for IMRT and VMAT deliveries largely because of their high accuracy in radiation transport modeling of the complex linear accelerator collimation systems and also of the patient's anatomical inhomogeneities [17-22]. With the recent introduction of two new sources, ISOURCE 20 and 21, in the DOSXYZnrc/EGSnrc code [23], MC simulation and dose calculation of a continuous beam delivery for VMAT is now possible in a single simulation. In addition, accurate MC simulation of EPID images can be useful for verification of complex treatment techniques [24-26]. Thus, one can employ MC as a tool for validating the accuracy of the individual control points of a VMAT delivery as measured by planar detectors, and for verifying TPS calculated dose. Other previous studies [27, 28] have described a method of combining a CT defined density data set (representing a phantom or patient), and a non-CT defined density data set representing an EPID, validated for single or few conformal fields at arbitrary beam angles. However, a general tool incorporating CT defined patient/phantom data sets together with an arbitrary planar detector positioned as either an entrance or an exit detector has not yet been investigated for VMAT applications. In addition, one of the limitations of the current verification methods using MC is that they only verify the dose calculated by the TPS, without verifying the actual dose delivered to the patient on the linac. These shortcomings are addressed in the research work presented in this chapter.

In this work, we describe and validate a novel Monte Carlo simulation tool that provides both the calculated dose to an arbitrary planar detector and the calculated dose to the patient or phantom data set, for individual gantry angle fluences of VMAT treatments. The approach is also demonstrated for DIMRT treatment delivery, still commonly used in many clinics. Our approach keeps the gantry and the planar detector at a fixed geometry while rotating the phantom/patient scoring geometry as a function of gantry angle, simultaneously tracking dose deposited in both volumes. The software codes are freely available from the first author to interested researchers for non-commercial purposes.

5.2 Materials and Methods

5.2.1 Monte Carlo simulation tool for VMAT

An overview of the different steps in the MC simulation tool for calculating individual control points of a VMAT delivery is shown in figure 5.1. There are three main steps - pre-simulation, simulation, and post-simulation. In the pre-simulation step, treatment verification plans on phantom CT data sets and Monte Carlo input files for the simulation of the individual control points are created and organized. The simulation step manages the simulations based on the input files, and the post-simulation step analyses the 2D planar detector doses as well as the 3D patient/phantom doses (the latter is handled by recombining them into a single patient dataset representing MC calculated dose). Each step is described in more detail in the following sections.

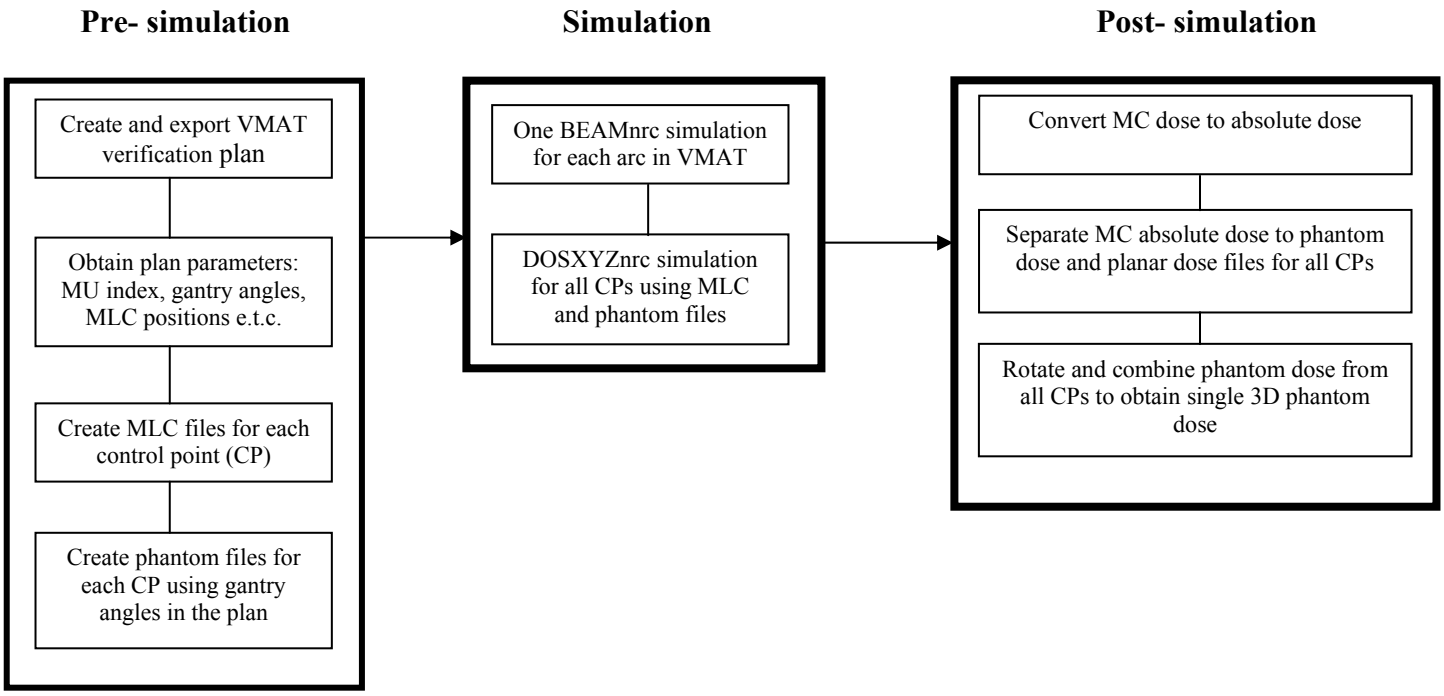


Figure 5-1: An overview of the MC simulation tool for calculating dose simultaneously in the patient/phantom geometry and the planar detector geometry, for individual control points of a VMAT delivery.

5.2.1.1 BEAMnrc simulation of the linac head

The simulation of the linac head of the 6MV photon beam was performed using BEAMnrc Monte Carlo code and has been previously validated to within <2% for depth dose, dose profile, and output factor measurements [29]. We obtained a phase-space file of the linac head simulation for the individual beams in the verification plans. It contains a full description of particles that reached the scoring plane below the secondary collimators (i.e. jaws) and was used as a source in the DOSXYZnrc dose calculation. In

this work, 6 x 10^9 electrons incident on the target were simulated and resulted in scored particle counts of between 1.2 x 10^9 and 1.9 x 10^9 in the scoring plane, depending on the field sizes in the verification plans.

5.2.1.2 Dose calculation of VMAT delivery for each control point

The EGSnrc Monte Carlo package was used for simulation and dose calculation of the treatment plans. For dose calculation purposes, we obtained plan parameters such as MLC leaf positions, cumulative MU index, and gantry angles for each control point from the exported DICOM RT file using the CERR package [30] which contains a DICOM-RT toolbox [31] written in MATLAB (MathWorks, Natick, MA). The *particleDMLC* code [32, 33], compiled as a shared library for the DOSXYZnrc calculation was used to simulate particle transport dynamically through a given aperture to achieve intensity modulation of the verification plan. The new VMAT MC tool performs dose calculations of each control point and scores dose simultaneously in both the phantom defined geometry and the planar detector geometry. To accomplish this, we implement an approach that rotates the CT data defined geometry (representing the phantom or patient) by the corresponding gantry angle for each control point, while keeping the gantry and planar detector geometries fixed during the simulation and dose calculation. The approach is general to any planar detector, which may be located either upstream (i.e. entrance dosimetry) or downstream (i.e. exit dosimetry) of the patient. It allows the detector geometry to be defined at relatively high spatial resolution, thus accurately modeling the thin layers encountered in most planar detectors (e.g. EPID).

However, this approach requires that dose delivered to the rotated phantom geometry be mapped back onto the non-rotated geometry for proper dose accumulation in the phantom as described in Section 5.2.3.

The detailed steps for simulating VMAT delivery in both phantom/patient and planar detector geometries simultaneously are:

1. Align the position of the CT dataset representing the patient or phantom to isocentre. A MATLAB code developed to read CT datasets from the TPS was used to obtain the CT center and planning isocentre positions from the planning data. Correct positioning of the isocentre location in a new CT dataset is ensured by shifting the CT center point relative to the planning isocentre in all dimensions (x, y, and z). This code also removes the CT couch in the CT dataset and replaces it with the treatment couch.
2. For the isocentre-aligned CT datasets, with treatment couch added, we used the *ctcreate* code contained in the EGSnrc package to obtain a Monte Carlo phantom file with extension .egsphant. The phantom file (figure 5.2) contains the physical density and material numbers for the cylindrical phantom or the anthropomorphic phantom derived from the CT data sets, as required.
3. To create the phantom file for each control point, we combine patient/phantom file with planar detector phantom file using a dedicated MATLAB routine to obtain a single MC phantom file (e.g. Phantom+ EPID). For each individual control point, the MATLAB code rotates the phantom only using the gantry angle

obtained from the plan data sequentially and writes phantom files for *all* the control points (figure 5.2). The phantom volume was rotated in the opposite direction to the TPS indicated gantry rotation, and unique phantom files were created for each control point. The code is reasonably efficient (for example, it took about 15 mins to write 177 MC phantom files).

4. The leaf sequence file containing the MLC leaf positions and monitor unit (MU) index for all the control points in the verification plans were divided to generate new leaf sequence files, one for each control point.
5. The Monte Carlo simulation for each control point (figure 5.3) in the verification plan requires a MLC leaf sequence file and a phantom file. Dose calculation of the individual control points in the treatment verification plans described in section 5.2.2 was performed at fixed (zero) gantry angle using the new DOSXYZnrc source, ISOURCE 20.

An illustration of MC modelling as well as the simulation of the particle transport in the patient/phantom and in the detector is shown in figure 5.3. In our approach, the patient/phantom and the detector are part of the same phantom in DOSXYZnrc, in which full MC transport is carried out. Dose was scored in the entire defined simulation geometry including the combined geometries of both the patient/phantom and the planar detector

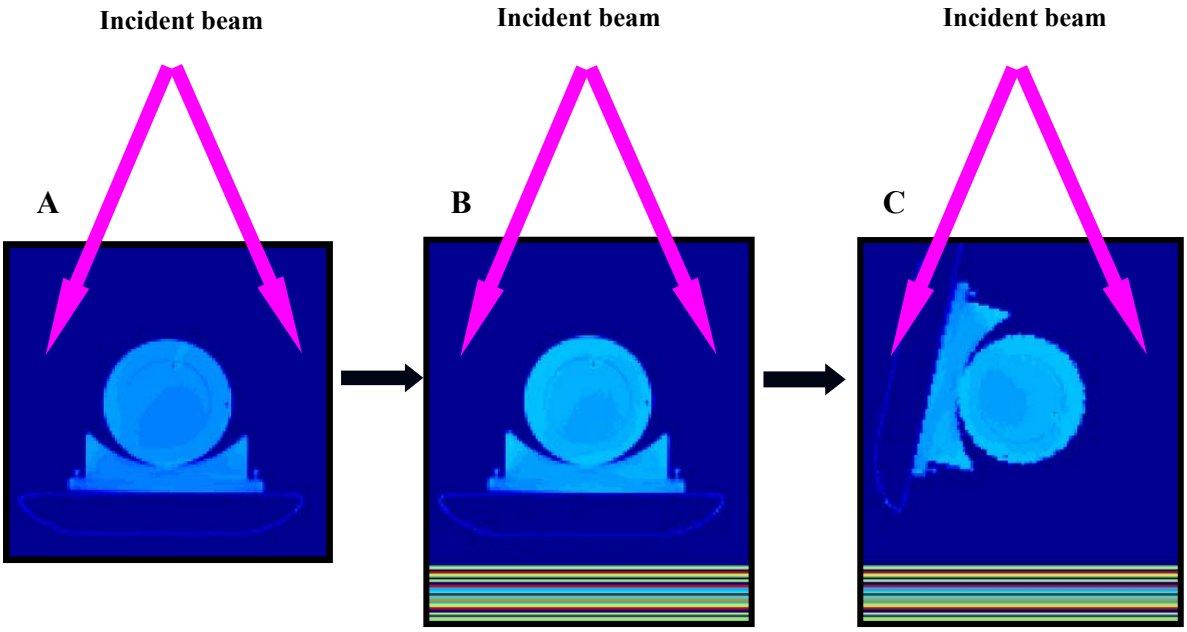


Figure 5-2: Illustration of the process to obtain MC phantom files. In panel A, we have the phantom only, then the planar detector model is added in panel B (an EPID for illustration) and panel C demonstrates how we rotate the phantom only (and in the opposite direction to the TPS indicated gantry rotation) in order to orient it correctly to the linac and planar detector geometry. Note the EPID layer thicknesses are not drawn to scale.

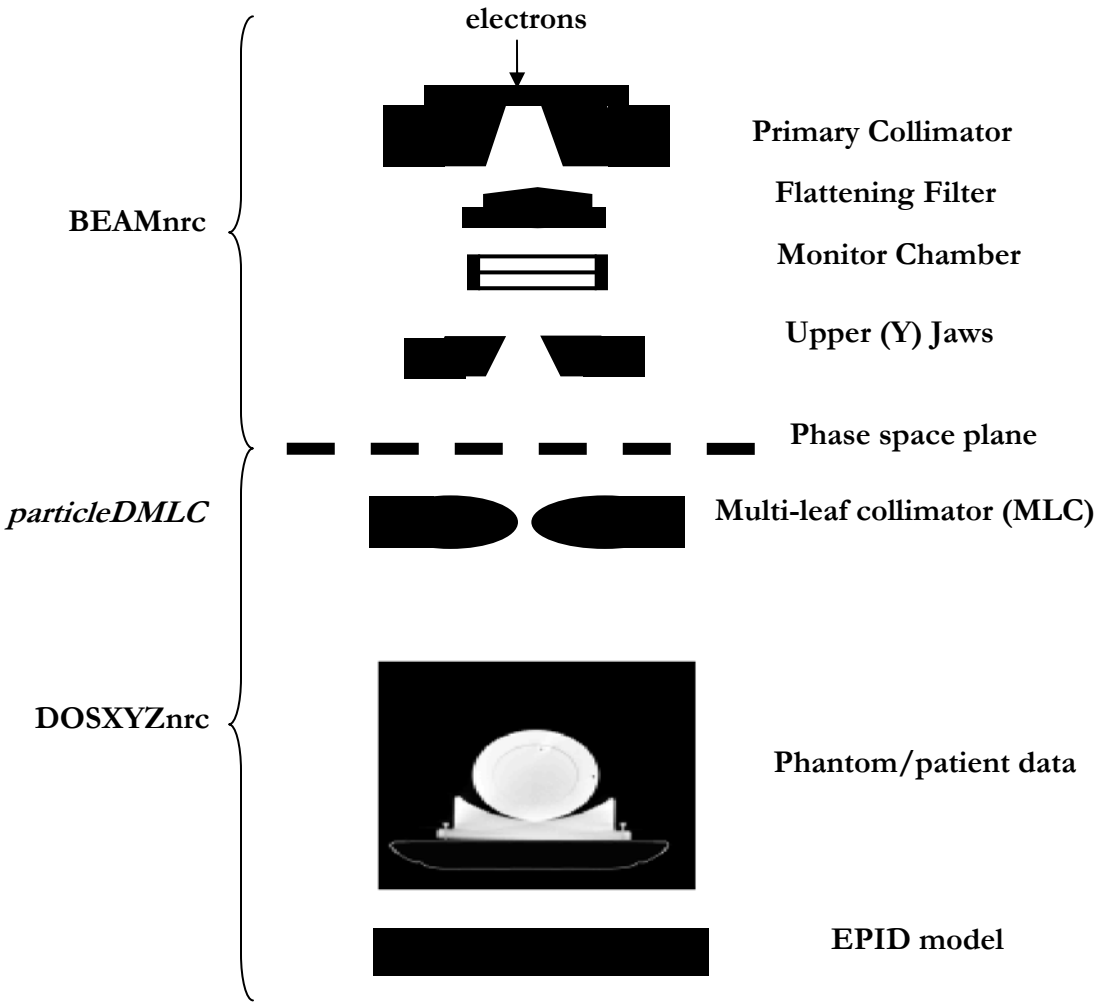


Figure 5-3: Monte Carlo setup used for verification of individual control points of a VMAT delivery measured by EPID. Simulations of MLC leaf positions for individual control points were performed using *particleDMLC* code complied as a shared library in DOSXYZnrc. Lower (X) jaws are not shown here.

5.2.2 Validation of the VMAT Monte Carlo tool with an entrance and an exit detector

All measurements in this work were performed on a Clinac 2100ix equipped with Millennium 120-leaf MLC (Varian Medical Systems, Palo Alto, CA) capable of delivering RapidArc^{TM} treatment plans (Varian's implementation of VMAT). RapidArc plans at our center are created in the Eclipse treatment planning system (TPS; version 10.0.39, Varian Medical Systems, Palo Alto, CA) using the AAA dose calculation algorithm. For the Monte Carlo simulation and analysis purposes, all treatment planning data including patient images (CT dataset), treatment plan, contoured structures, and the calculated dose were exported via DICOM.

At our institute, VMAT treatment plans typically consist of two full or partial arcs with clockwise (CW) and counter-clockwise (CCW) gantry rotations. For this work, we used three clinical treatment plans consisting of one dynamic IMRT head-and-neck plan and two VMAT plans (one prostate and one head-and-neck). Two planar detector systems were used for validation, including an exit detector (aS1000 EPID) and an entrance detector (COMPASS transmission detector or 'TRD', IBA Dosimetry, Swarzenbruck, Germany). The VMAT prostate and head-and-neck plans were re-calculated on CT data sets of a cylindrical and an anthropomorphic phantom (Rando, The Phantom Laboratory, Salem, NY), respectively, in both cases using the exit detector (aS1000 EPID). The homogeneous acrylic cylindrical phantom has a 16 cm diameter and 30 cm length, developed for local commissioning of VMAT treatment at our centre. The dynamic IMRT plan was re-calculated on the patient CT data set and the TRD entrance

detector. The entrance detector functionality of the MC simulation tool is validated with DIMRT fields instead of a VMAT delivery. We used DIMRT plans as a simple extension of the simulation tool because like VMAT plans they are composed of multiple control points separated by avoidance sectors and a useful option for validating our Monte Carlo tool.

For the DOSXYZnrc simulations of the individual control points, between $5x10^7$ and $6x10^7$ particles were simulated and doses were scored in the phantoms using 0.5 x 0.5 x 0.5 cm^3 voxels. The electron energy cutoff (ECUT) and photon energy cutoff (PCUT) were set to 0.7 MeV and 0.010 MeV respectively. The aS1000 EPID used in this work was modeled as twenty-two material slabs with detailed thicknesses and material composition provided by the manufacturer. In addition, the TRD was modeled as three material slabs as described in [29]. The pixel resolution of the MC EPID and TRD models was set to 0.5 x 0.5 cm^2, similar to the voxels that defined the phantom.

5.2.2.1 EPID and portal image acquisition of VMAT delivery

The verification plans for prostate and partial-arc head-and-neck were delivered at the linac to the cylindrical and anthropomorphic phantom respectively while portal images were collected using an aS1000 amorphous-silicon EPID fixed to the linac. The EPID has an active area of 40 cm x 30 cm at isocentre and contains 1024 x 768 pixels. For this work, the EPID was placed at a source-detector distance of 140 cm. The EPID acquisition software (IAS3) was used in continuous acquisition mode (i.e. cine mode) for

image acquisition with three frame averaging, resulting in an effective frame-rate of approximately 2.5 images per second. In the cine mode, a sequence of images is acquired continuously and saved as a function of time, representing dose delivered over a specific small but discrete gantry angle arc during the irradiation. Gantry rotational speed for the tested VMAT plans is constant and about 4.8 degrees/second; therefore the gantry moves about 1.9 degrees per EPID image. After image acquisition, the images were transferred via DICOM format and in-house software coded in MATLAB was used to interpolate images for each control point. In this way, we mapped the measured EPID images, where individual images represented a small range of gantry angles, to the single value of gantry angle valid for each control point in the VMAT plan. Furthermore, the EPID images for each control point were corrected for flood field images, backscatter from the EPID support arm and optical glare effect [34, 35] . For additional accuracy in the dosimetry, the effect of image shift due to EPID mechanical sag during gantry rotation was corrected for using a method described in the literature [36]. The measured EPID images, in arbitrary grayscale units, were converted to absolute dose through normalization by a calibration factor obtained using a unique formalism developed and described in the Appendix. The resultant absolute dose distributions were re-sampled to 0.5 x 0.5 cm^2 size for comparison to Monte Carlo calculated EPID dose described in section 5.2.1.2.

5.2.2.2 Entrance fluence measurement of DIMRT delivery

The COMPASS transmission detector previously studied by our group was used in this work [12]. This entrance measurement device consists of a 2D array of 1600

vented plane parallel ionization chambers arranged in a uniform 40 x 40 grid. Each chamber is 3.8 mm in diameter and 2 mm in height, giving a sensitive volume of 0.02 cm^3. The center-to-center chamber distance is 6.5 mm. The detector design includes a top layer of 3 mm water-equivalent RW3 material (density 1.045 g/cm^3). The verification plan for DIMRT head-and-neck was delivered at the linac and entrance fluences were collected via TRD. The detector was operated in movie mode, which allows the user to specify a frame sampling period and the system acquires measurements continuously while the beam is on (with no dead-time)**.** For this work, the sampling period was set to 40 ms. After data acquisition, in-house software coded in MATLAB was used to interpolate the TRD measured planar dose for each control point, allowing a direct comparison to calculated TRD dose for all control points. The measured TRD data were linearly interpolated to match the MC resolution of 5 mm before performing the gamma evaluation test. To compare with MC 3D dose, the TPS calculated 3D dose was corrected for the attenuation of the transmission detector by using a transmission factor of 0.967 as found by [12].

5.2.3 Evaluation of simulated 2D planar doses and simulated 3D doses

The method outlined above results in a .3ddose output file for each control point with the gantry and planar detector at fixed positions with gantry at zero degrees. Since the gantry-detector rotation is simulated by a counter rotation of the patient/phantom geometry some post-simulation processing is required to recover the total dose delivered to the non-rotated patient/phantom geometry. The MC dose (Gy/incident particle) for

each control point was converted to absolute dose to the medium (Gy) using the formalism described by Popescu *et al* [37]. The variable dose rate for the individual control points obtained from the planning data was included in this conversion. For each control point, the absolute dose was then separated into 3D patient/phantom dose and 2D planar detector dose.

For the phantom/patient dose, the 3D absolute dose distributions for all control points in an arc were rotated using the gantry angles to match the unrotated detector geometry. Then the correctly-oriented phantom doses for all control points are summed to obtain the dose for a single arc; the phantom doses for both arcs are then summed to obtain the total phantom dose simulated for the validation plan. Note that the patient/phantom dose for each individual control point is still available, if desired by the research application.

The Monte Carlo total phantom dose, calculated using 0.5 x 0.5 x 0.5 cm^3 voxels, was extracted and re-sampled to match the TPS dose calculation grid obtained using 0.25 x 0.25 x 0.25 cm^3 pixels. Monte Carlo and TPS 3D phantom absolute dose distributions were compared using the gamma evaluation test [38] with 3% and 3 mm criteria. For dose to the planar detector, a 2D MC dose distribution for all control points was obtained at the plane of the sensitive layer in the model of the transmission detector or EPID. The Monte Carlo planar 2D dose distribution for each control point was compared to those measured by the transmission detector or EPID using the gamma evaluation test with 3% and 3 mm criteria. For gamma evaluation test, we used the MC calculations as the 'test'

dose distribution and measured doses as reference dose distribution. The phantom dose distributions, measured and calculated, were normalized to their respective maximum doses for gamma test. While the planar dose distributions (measured and calculated) for each control point were normalized to their respective maximum doses.

5.3 Results

5.3.1 Validation of phantom or patient dose

The statistical uncertainty of the Monte Carlo (MC) calculated dose for all the verification plans were normalized to the maximum dose (not local dose) in the patient and was found to be less than 1% . The validation of the Monte Carlo simulation tool for calculating the 3D phantom/patient dose was accomplished by comparing simulation results to the TPS calculated dose. In figure 5.4, Monte Carlo 3D absolute dose distributions for the VMAT prostate plan calculated on the homogeneous, cylindrical phantom are illustrated in transverse, sagittal, and coronal planes. The figure also contains the gamma map result of the quantitative evaluation of the TPS and MC calculated doses and the dose profiles for the three planes, demonstrating very good qualitative agreement between them in both the central, high-dose region and in the tail regions of the profiles. Although not shown here, we observed similar agreement for the head-and-neck VMAT and DIMRT verification plans. Quantitative comparison of MC and TPS dose distributions for all verification plans was performed using the gamma evaluation test with acceptance criteria of 3% of maximum dose and 3 mm. The results of

the percentage of voxels ($\mathbf{PP_{\gamma<1}}$) within tolerance (i.e. with gamma values less than one) and average gamma ($\boldsymbol{\gamma_{AVG}}$) are shown in Table 5.1. We found excellent agreement between MC and TPS calculated doses for the treatment verification plans, with 96.7%, 95.3 % and 94.6 % of voxels having $\gamma<1$ for the VMAT prostate case, VMAT head-and-neck case, and DIMRT head-and-neck case respectively. The level of agreement observed here is similar to other reports in the literature that investigate Monte Carlo patient dose calculation of VMAT delivery [20, 23]

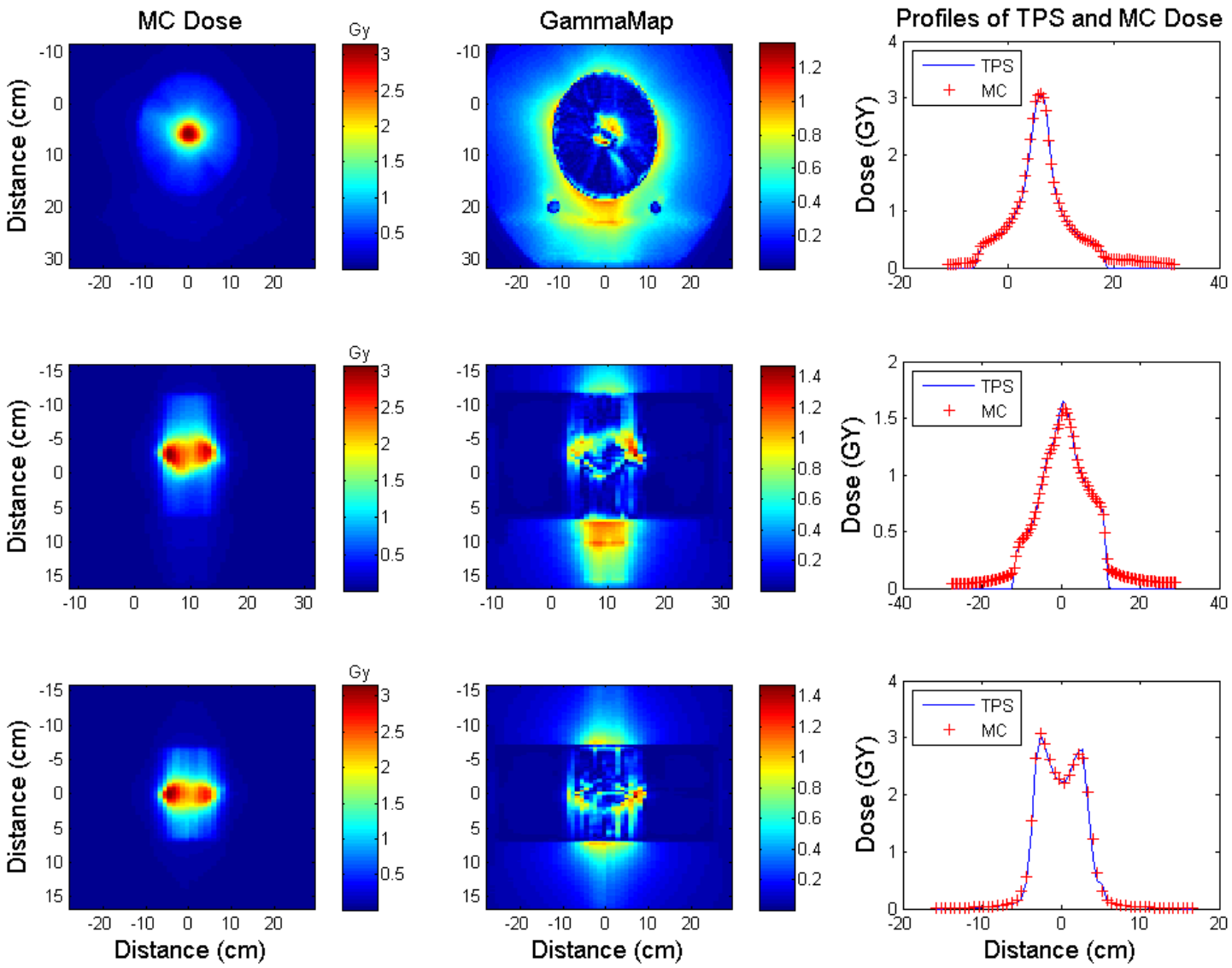


Figure 5-4: Monte Carlo calculated absolute dose for a VMAT prostate plan illustrated in transverse (top panel), sagittal (middle panel), and coronal (bottom panel) planes. Their respective Gamma maps (i.e. quantitative evaluation between MC and TPS dose distributions) and dose profiles are also shown here.

Table 5-1: Percentage of voxels with $\gamma<1$ ($PP_{\gamma<1}$) and average gamma (γ_{AVG}) using 3% DD and 3 mm DTA for the verification plans.

Number	Type	$PP_{\gamma<1}$	γ_{AVG}
Plan 1	**VMAT Prostate**	**96.7%**	**0.25**
Plan 2	**VMAT H&N**	**95.3%**	**0.45**
Plan 3	**DIMRT H&N**	**94.6%**	**0.48**

5.3.2 Validation of planar dose

Figure 5.5 shows examples of the MC calculated dose to the EPID and the measured EPID dose for several control points in the prostate verification plan. The figure illustrates that the simulation tool is able to accurately predict the beam shape and dose magnitude of the individual control points of a VMAT treatment delivery. The planar doses (measured and calculated) for the each control point were normalized to their respective maximum doses. We performed quantitative analysis by comparing the MC dose to the measured EPID dose for all the control points in the verification plans using the gamma evaluation test with 3% of maximum dose as dose difference (DD) and 3 mm as distance to agreement (DTA) acceptance criteria. To evaluate performance in the high-dose image region representing the treatment beam of the individual control points, the gamma test was performed after applying a 10% dose threshold (i.e. 10% of maximum dose). Results of the percentage of pixels with **$\gamma<1$** (**$PP_{\gamma<1}$**) for the prostate and

the head-and-neck verification plans are shown in figure 5.6. The figure contains the histogram plots of the percentage of pixels and the average gamma for all control points in arc 1 – prostate (top row) and head-and-neck (middle row). The average gamma (γ_{AVG}) summarizes the gamma results of the planar dose distributions and it is widely used in the literature for this purpose [39-41]. When performing the gamma test with 3% DD and 3 mm DTA criteria, it is typically expected that at least 90% of the comparison points lie within this tolerance [42]. In this work, we observed that while most control points satisfy this criteria, there are few control points with $\mathbf{PP}_{\gamma<1}$ below 90% (table 5.2), and we investigated the cause of this discrepancy. Figure 5.7 shows the MC calculated and measured EPID dose for one of the control point. As shown in the measured EPID dose in the figure, the beam shape was predicted properly but on the corresponding measured EPID image, the level of intensity within the open field is not uniform. This banding is a real dosimetric effect caused by beam hold-offs (i.e. dose pulse dropping) occurring during the VMAT delivery, which show up in the image as low intensity banding due to this 'missing' dose [43]. This is a known limitation of the current EPID image acquisition software (IAS3) but the effect is significantly reduced with frame averaging where a dropped pulse becomes a smaller portion of the delivered image intensity for a given image. However, the MC predicted doses could be further refined by using inputs derived from the dynalog files (which record the beam hold-offs) together with the TPS-generated DICOM RP inputs.

We obtained MC calculated doses for all control points in the DIMRT head-and-neck verification plan, scored in the sensitive layer of the transmission detector. Then we

performed quantitative analysis by comparing MC calculated dose to measured dose for all the control points using the gamma test with 3 % DD and 3 mm DTA. Results of the percentage of pixels with gamma less than one ($\mathbf{PP_{\gamma<1}}$) are shown in figure 5.6 (bottom row), which contains the histogram plots of $\mathbf{PP_{\gamma<1}}$ and $\mathbf{\gamma_{AVG}}$ for all control points in the first field of the DIMRT verification plan. Similar to the VMAT MC calculated dose, the results for the TRD show that the verification tool is able to accurately predict individual entrance detector doses for the DIMRT plan.

Table 5-2: Range of percentage of pixels ($PP_{\gamma<1}$) with $\gamma<1$, range of average gamma (γ_{AVG}) and range of maximum gamma (γ_{MAX}) using 3% DD and 3 mm DTA for all the control points in both the clockwise (CW) and counterclockwise (CCW) arcs. Number of control point images with less than 90% of voxels with $\gamma<1$ (last column)

Number	Type	$PP_{\gamma<1}$	γ_{AVG}	γ_{MAX}	CPs
Plan 1	Prostate VMAT	73.74 – 99.00 %	0.16 -0.73	1.28-11.78	7/177
		83.27 – 100 %	0.17 – 0.61	0.97-9.58	8/177
Plan 2	H&N VMAT	78.39 – 99.49 %	0.19 – 0.79	1.06-10.17	15/114
		73.04 – 98.94 %	0.16 – 0.96	1.30-11.33	29/114
Plan 3	H&N DIMRT	84.38 – 100 %	0.13 – 0.55	0.89-11.05	12/122
		83.33 – 100 %	0.15 – 0.99	0.79-13.34	23/137

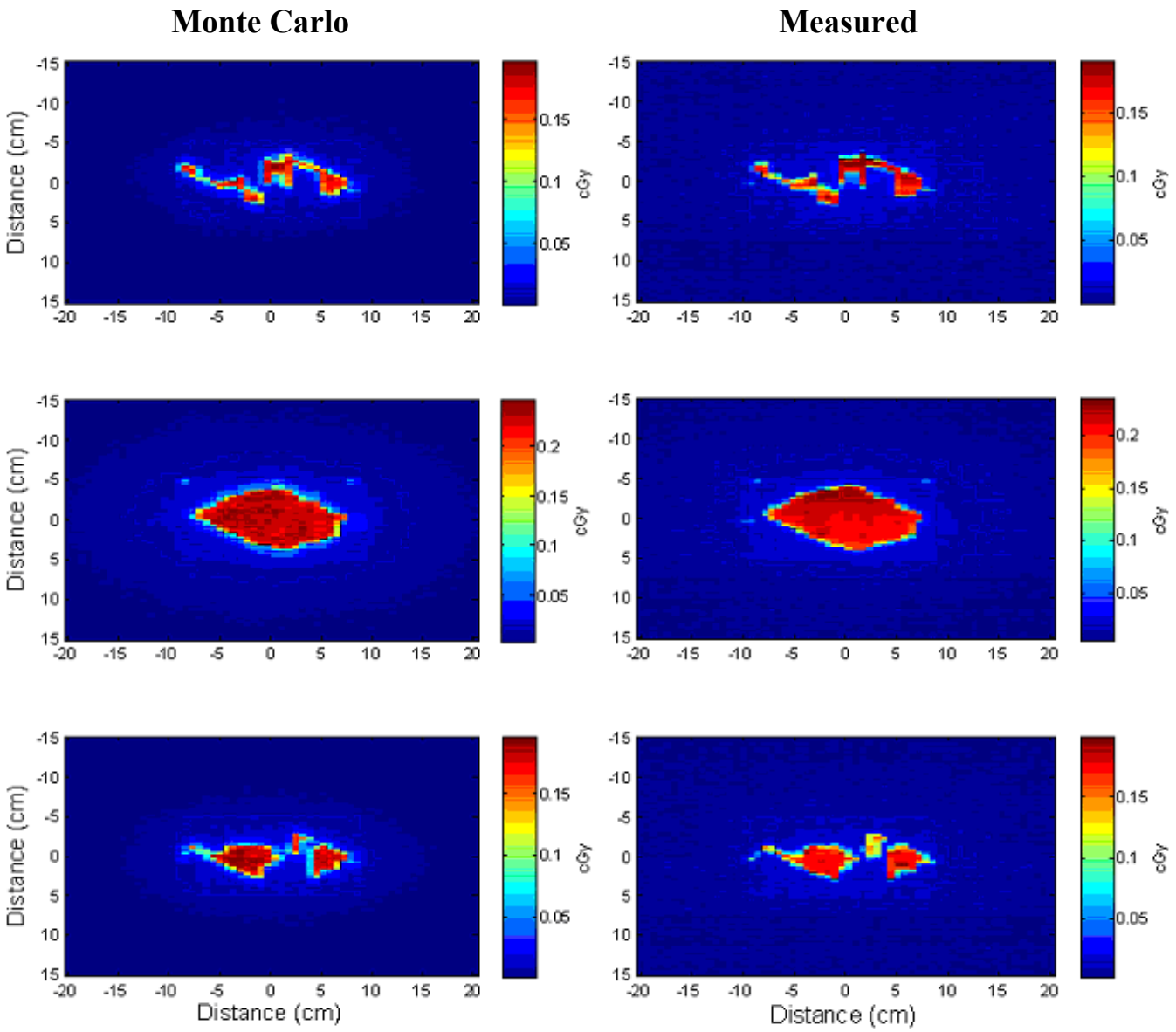


Figure 5-5: Monte Carlo calculated EPID dose (left panel) and measured EPID dose (right panel) for three randomly selected different control points 68, 93, and 28 in the VMAT prostate plan.

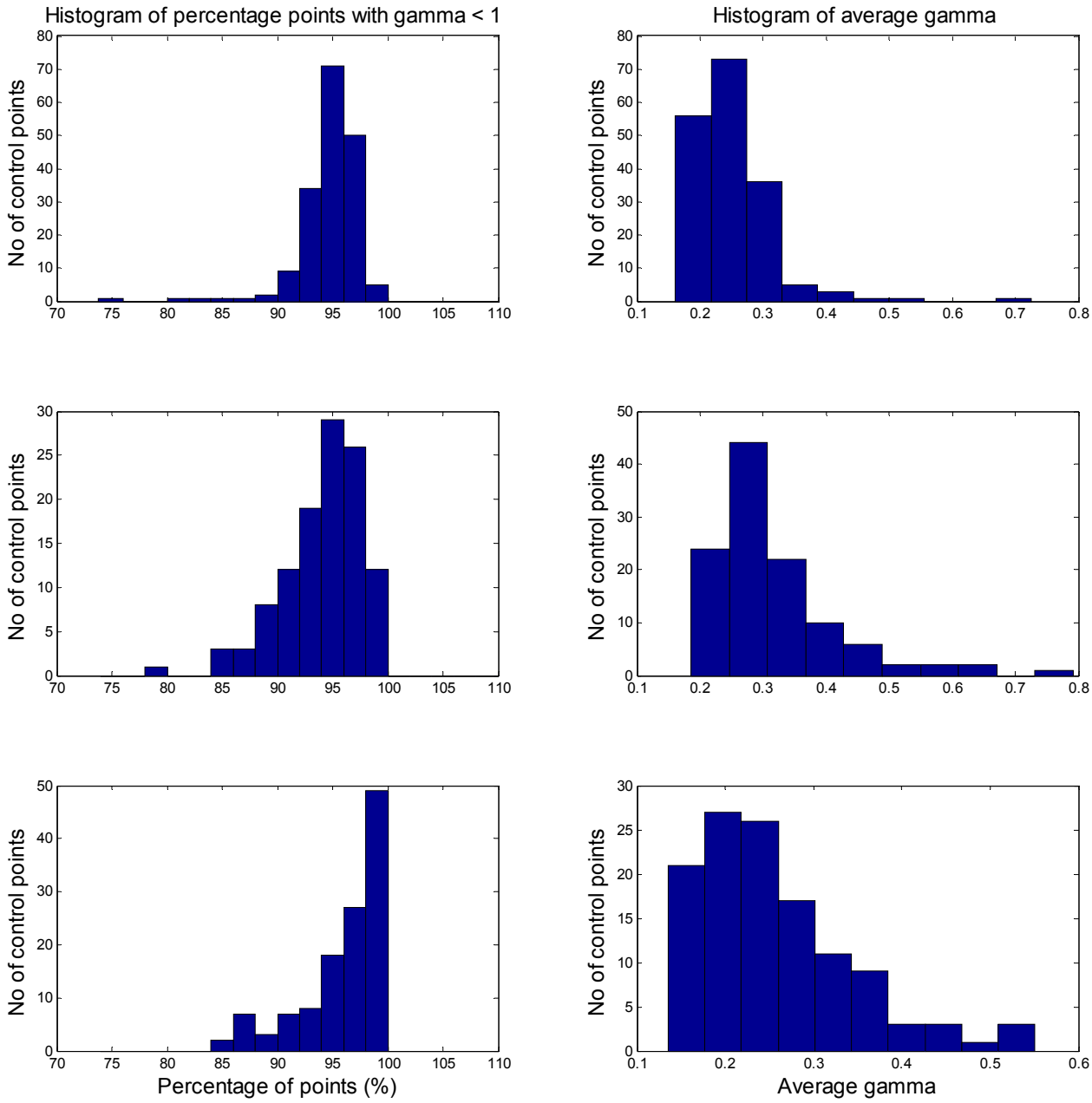


Figure 5-6: Histogram of $PP_{\gamma<1}$ and γ_{AVG} as a function of control points for arc 1 – VMAT prostate plan (top row), arc 1 - VMAT head-and-neck (middle row), and beam 1 DIMRT head-and-neck (bottom row).

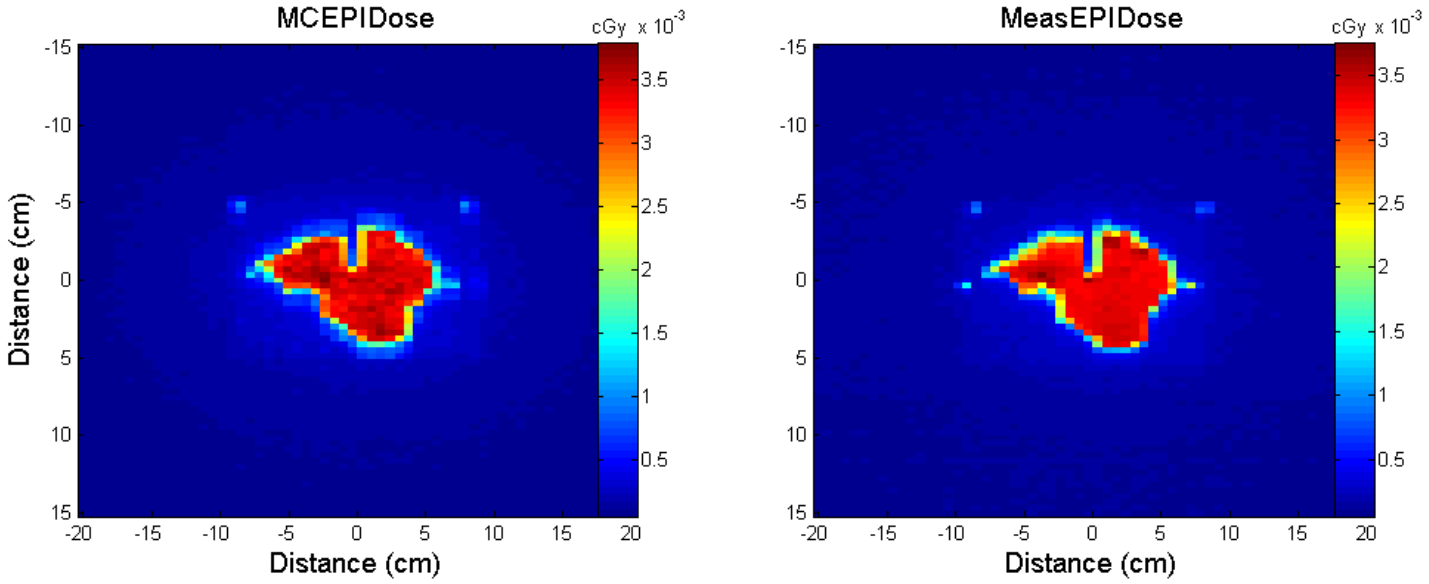


Figure 5-7: Monte Carlo calculated and measured EPID doses for one of the control points in the VMAT prostate plan showing the banding artifact in measured data.

5.4 Discussion and Conclusions

The increased complexity of VMAT techniques justifies more stringent patient-specific verification, with many arguing for *in vivo* dose verification approaches [15, 16, 44] . Both commercial and experimental systems utilizing planar dose detectors continue to be developed for this application [10-12].Verification mechanisms that check performance through measurement of fluence for individual control points of a VMAT delivery are appropriate since the temporal dependence of the dose delivery directly affects the total dose delivered to the patient.

In this work, we present a novel research tool that will assist these development

efforts. We develop and validate a Monte Carlo simulation tool that simultaneously obtains the phantom/patient dose and the dose scored in an arbitrary planar detector. This approach allows one to evaluate the accuracy of fluence (i.e. indirectly through dose) measured by any planar detector for the individual control points of a VMAT delivery, while also calculating the corresponding patient dose for the control point. The tool is validated for three clinical treatment plans in controlled phantom situations with results showing the MC dose calculation for both phantom/patient and planar detector are accurate. The Monte Carlo total dose to the phantom agrees very well with TPS calculated dose for all verification plans and our results are similar in accuracy to those in the literature for VMAT Monte Carlo dose calculation within patients/phantoms [20, 23]. For planar dosimetry, we mainly validated the tool with an exit detector (EPID) and found that more than 95% of control points passed the 3% DD and 3 mm DTA gamma evaluation tests, with a pass defined as having more than 90% of voxels with gamma less than one. However, we observed a few control points in the verification plans have $\mathbf{PP}_{\gamma<1}$ less than 90%, and we attribute these to a subtle dosimetric effect in the corresponding measured EPID dose images occurring when linac dose pulses are dropped. The presence of this effect is not a significant concern for the validation work here, since it is understood and occurs reasonably infrequently. In general, our results indicate that the simulation tool is suitable for accurately calculating both patient/phantom doses and planar doses for VMAT dose delivery.

The tool will be useful for investigating the performance of and assisting in the design of *in vivo* planar detectors for measurement-based VMAT dose verification. In

addition, it can be a useful independent research tool for VMAT commissioning of the TPS and delivery system. Currently, however, one notable limitation of this Monte Carlo research tool is the long calculation times, which make it unsuitable for routine clinical patient-specific dose verification of VMAT. For example, it took 336 hours of simulation time on a 48-core machine for the 354 control points of the most complex verification plan tested here. However, this situation could change dramatically by using the fast MC code VMC++ [45-47], where simulation speeds ten times faster than EGSnrc have been reported [46], and this will be the subject of an upcoming study. Despite this inconvenience, the simulation tool described in this paper will contribute to the improvement of current quality assurance techniques for VMAT treatment delivery.

APPENDIX. Dose calibration formalism for measured signal

Using MC absolute dose calibration method described by [37] we derived the absolute dose (D_{abs}^{MC}) scored in the sensitive layer of the EPID and TRD as follows:

$$D_{abs}^{MC} = D_{xyz} \frac{D_{ch}(10\times 10)}{D_{ch}} \frac{D_{xyz,abs}^{cal}}{D_{xyz}^{cal}} U \quad \text{(Gy/MU)} \tag{5.1}$$

where parameters are the same as those in [37] . D_{xyz} is the normalized dose (in Gy per incident particle) deposited in a voxel of a water or patient CT phantom (from a DOSXYZnrc simulation). $D_{xyz,abs}^{cal}$ is the absolute dose (in Gy) deposited in the voxel where D_{xyz}^{cal} was scored. D_{ch} is the normalized dose (in Gy per incident particle) accumulated in the monitor chamber of the virtual linac (from a BEAMnrc simulation).

For the EPID at 140 cm SID for 100 MU dose, the MC absolute dose in the central axis is given as:

$$D_{abs,100MU}^{MC} = 100MU \times D_{abs}^{MC}(Gy/MU) \quad \text{(Gy)} \tag{5.2}$$

The measured EPID signal at 140 cm SID for 10 x10 cm^2 using 100 MU is given as:

$$D_{100MU}^{Measured} = D_{mean}^{Measured} \times N_{frames} \quad \text{(AU)} \tag{5.3}$$

where is $D_{mean}^{Measured}$ the average measured signal in arbitrary units for number of frames N_{frames}

The calibration factor (CF) is then given as:

$$CF = \frac{D_{abs,100MU}^{MC}}{D_{100MU}^{Measured}} \text{ (Gy/AU)} \tag{5.4}$$

Using the calibration factor we obtain measured absolute dose as follows:

$$D_{abs}^{Measured} = D_{xy}^{Measured}(AU) \times CF(Gy/AU) \text{ (Gy)} \tag{5.5}$$

5.5 Bibliography

1. Ling, C.C., et al., *Commissioning and quality assurance of RapidArc radiotherapy delivery system.* Int J Radiat Oncol Biol Phys, 2008. **72**(2): p. 575-81.
2. Bedford, J.L. and A.P. Warrington, *Commissioning of volumetric modulated arc therapy (VMAT).* Int J Radiat Oncol Biol Phys, 2009. **73**(2): p. 537-45.
3. Dobler, B., et al., *Commissioning of volumetric modulated arc therapy (VMAT) in a dual-vendor environment.* Radiother Oncol, 2011. **99**(1): p. 86-9.
4. Manikandan, A., et al., *Quality assurance of dynamic parameters in volumetric modulated arc therapy.* Br J Radiol, 2012. **85**(1015): p. 1002-10.
5. Korreman, S., J. Medin, and F. Kjaer-Kristoffersen, *Dosimetric verification of RapidArc treatment delivery.* Acta Oncol, 2009. **48**(2): p. 185-91.
6. Schreibmann, E., et al., *Patient-specific quality assurance method for VMAT treatment delivery.* Med Phys, 2009. **36**(10): p. 4530-5.
7. Bakhtiari, M., et al., *Using an EPID for patient-specific VMAT quality assurance.* Med Phys, 2011. **38**(3): p. 1366-73.
8. Boggula, R., et al., *Evaluation of a 2D detector array for patient-specific VMAT QA with different setups.* Phys Med Biol, 2011. **56**(22): p. 7163-77.
9. Masi, L., et al., *Quality assurance of volumetric modulated arc therapy: evaluation and comparison of different dosimetric systems.* Med Phys, 2011. **38**(2): p. 612-21.
10. Islam, M.K., et al., *An integral quality monitoring system for real-time*

verification of intensity modulated radiation therapy. Med Phys, 2009. **36**(12): p. 5420-8.

11. Poppe, B., et al., *Clinical performance of a transmission detector array for the permanent supervision of IMRT deliveries.* Radiother Oncol, 2010. **95**(2): p. 158-65.
12. Venkataraman, S., et al., *The influence of a novel transmission detector on 6 MV x-ray beam characteristics.* Phys Med Biol, 2009. **54**(10): p. 3173-83.
13. van Elmpt, W., et al., *A literature review of electronic portal imaging for radiotherapy dosimetry.* Radiother Oncol, 2008. **88**(3): p. 289-309.
14. McCurdy, B.M. and P.B. Greer, *Dosimetric properties of an amorphous-silicon EPID used in continuous acquisition mode for application to dynamic and arc IMRT.* Med Phys, 2009. **36**(7): p. 3028-39.
15. Mans, A., et al., *3D Dosimetric verification of volumetric-modulated arc therapy by portal dosimetry.* Radiother Oncol, 2010. **94**(2): p. 181-187.
16. Wendling, M., et al., *In aqua vivo EPID dosimetry.* Med Phys, 2012. **39**(1): p. 367.
17. Ma, C.M., et al., *Monte Carlo verification of IMRT dose distributions from a commercial treatment planning optimization system.* Phys Med Biol, 2000. **45**(9): p. 2483-95.
18. Wang, L., E. Yorke, and C.S. Chui, *Monte Carlo evaluation of tissue inhomogeneity effects in the treatment of the head and neck.* Int J Radiat Oncol Biol Phys, 2001. **50**(5): p. 1339-49.
19. Francescon, P., S. Cora, and P. Chiovati, *Dose verification of an IMRT treatment*

planning system with the BEAM EGS4-based Monte Carlo code. Med Phys, 2003. **30**(2): p. 144-57.

20. Bush, K., R. Townson, and S. Zavgorodni, *Monte Carlo simulation of RapidArc radiotherapy delivery.* Phys Med Biol, 2008. **53**(19): p. N359-70.
21. Gagne, I.M., et al., *A Monte Carlo evaluation of RapidArc dose calculations for oropharynx radiotherapy.* Phys Med Biol, 2008. **53**(24): p. 7167-85.
22. Teke, T., et al., *Monte Carlo based, patient-specific RapidArc QA using Linac log files.* Med Phys, 2010. **37**(1): p. 116-23.
23. Lobo, J. and I.A. Popescu, *Two new DOSXYZnrc sources for 4D Monte Carlo simulations of continuously variable beam configurations, with applications to RapidArc, VMAT, TomoTherapy and CyberKnife.* Phys Med Biol, 2010. **55**(16): p. 4431-43.
24. Spezi, E. and D.G. Lewis, *Full forward Monte Carlo calculation of portal dose from MLC collimated treatment beams.* Phys Med Biol, 2002. **47**(3): p. 377-90.
25. Siebers, J.V., et al., *Monte Carlo computation of dosimetric amorphous silicon electronic portal images.* Med Phys, 2004. **31**(7): p. 2135-46.
26. Cufflin, R.S., et al., *An investigation of the accuracy of Monte Carlo portal dosimetry for verification of IMRT with extended fields.* Phys Med Biol, 2010. **55**(16): p. 4589-600.
27. Chin, P., E. Spezi, and D. Lewis, *Monte Carlo simulation of portal dosimetry on a rectilinear voxel geometry: a variable gantry angle solution.* Phys Med Biol, 2003. **48**(16): p. N231.
28. Kairn, T., et al., *Accurately simulating the production of radiotherapy portal*

images using non-zero beam angles. Radiat Meas, 2011. **46**(12): p. 1967-1970.

29. Asuni, G., J.M. Jensen, and B.M. McCurdy, *A Monte Carlo investigation of contaminant electrons due to a novel in vivo transmission detector.* Phys Med Biol, 2011. **56**(4): p. 1207-23.
30. Deasy, J.O., A.I. Blanco, and V.H. Clark, *CERR: a computational environment for radiotherapy research.* Med Phys, 2003. **30**(5): p. 979-85.
31. Spezi, E., D.G. Lewis, and C.W. Smith, *A DICOM-RT-based toolbox for the evaluation and verification of radiotherapy plans.* Phys Med Biol, 2002. **47**(23): p. 4223-32.
32. Keall, P.J., et al., *Monte Carlo dose calculations for dynamic IMRT treatments.* Phys Med Biol, 2001. **46**(4): p. 929-41.
33. Siebers, J.V., et al., *A method for photon beam Monte Carlo multileaf collimator particle transport.* Phys Med Biol, 2002. **47**(17): p. 3225-49.
34. Chytyk-Praznik, K., et al., *Model-based prediction of portal dose images during patient treatment* 2013: p. *(in press)*.
35. Greer, P.B., *Correction of pixel sensitivity variation and off-axis response for amorphous silicon EPID dosimetry.* Med Phys, 2005. **32**(12): p. 3558-68.
36. Rowshanfarzad, P., et al., *Detection and correction for EPID and gantry sag during arc delivery using cine EPID imaging.* Med Phys, 2012. **39**(2): p. 623-35.
37. Popescu, I.A., et al., *Absolute dose calculations for Monte Carlo simulations of radiotherapy beams.* Phys Med Biol, 2005. **50**(14): p. 3375-92.
38. Low, D.A., et al., *A technique for the quantitative evaluation of dose distributions.* Med Phys, 1998. **25**(5): p. 656-61.

39. Childress, N.L., et al., *Detection of IMRT delivery errors using a quantitative 2D dosimetric verification system.* Med Phys, 2005. **32**(1): p. 153-62.

40. McDermott, L.N., et al., *Clinical experience with EPID dosimetry for prostate IMRT pre-treatment dose verification.* Med Phys, 2006. **33**(10): p. 3921-30.

41. Stock, M., B. Kroupa, and D. Georg, *Interpretation and evaluation of the gamma index and the gamma index angle for the verification of IMRT hybrid plans.* Phys Med Biol, 2005. **50**(3): p. 399-411.

42. Ezzell, G.A., et al., *IMRT commissioning: multiple institution planning and dosimetry comparisons, a report from AAPM Task Group 119.* Med Phys, 2009. **36**(11): p. 5359-73.

43. King, B., E. Seymour, and K. Nitschke, *SU-ET-171: Missing Dose in Integrated EPID Images.* Medical Physics, 2012. **39**(6): p. 3742.

44. Mans, A., et al., *Catching errors with in vivo EPID dosimetry.* Med Phys, 2010. **37**: p. 2638.

45. Kawrakow, I. *VMC++, electron and photon Monte Carlo calculations optimized for radiation treatment planning*. in *Advanced Monte Carlo for Radiation Physics, Particle Transport Simulation and Applications: Proc. Monte Carlo 2000 Meeting*. 2001: Berlin: Springer.

46. Gardner, J., J. Siebers, and I. Kawrakow, *Dose calculation validation of Vmc++ for photon beams.* Med Phys, 2007. **34**(5): p. 1809-18.

47. Hasenbalg, F., et al., *VMC++ versus BEAMnrc: a comparison of simulated linear accelerator heads for photon beams.* Med Phys, 2008. **35**(4): p. 1521-31.

CHAPTER SIX: SUMMARY

6.1 Conclusions

Radiation therapy has been the choice treatment modality for thousands of cancer patients all around the world [1]. Accurate delivery of radiation to cancerous cells is crucial to positive treatment outcomes. Recent advancements in radiation therapy including the introduction of complex treatment techniques such as intensity modulated radiation therapy (IMRT) and Volumetric modulated radiation therapy (VMAT) have improved conformity of radiation dose distributions to cancerous cells with improved sparing of normal tissue structures compared to previous treatment techniques. These procedures result in adequate or improved tumour control with reduced normal tissue complications as described in chapter 1 of this thesis. However, they also introduced great challenges in ensuring that the delivered dose distributions correspond closely to those planned (i.e. within acceptable tolerances).

Measurement-based, pre-treatment dose verification of the customized treatment plan is commonly performed before patient treatment begins, without the patient present, to verify the ability of the planning system to calculate dose accurately and the ability of the radiotherapy treatment machine to deliver dose accurately. In addition to measurement-based dose verification, an independent dose calculation of the treatment plan may be performed, or a combination of both methods is used. The standard procedure for measurement-based verification includes a point dose check using an

ionization chamber placed in a phantom and/or a planar dose measurement with one or several sheets of radiographic or radiochromic film inserted in the phantom. Because the use of films is very time consuming and labour intensive, other devices such as arrays of diodes or ionization chambers either placed on the treatment couch or attached to the head of the gantry are being used. EPIDs may also be used in this application as well. However, pre-treatment dose verification has the disadvantage of being performed without the patient present. Therefore, *in vivo* dose verification that verifies the dose that is actually delivered to the patient at the time of treatment would be appropriate to reduce treatment delivery errors. This dose verification technique is recommended by several organizations [2-5] and may be performed as an entrance or exit dosimetry procedure.

As discussed in chapter 2 of this thesis*, in vivo* entrance dosimetry through 2D detector arrays has been a focus of increasing research interest for checking beam characteristics and performance of the linac during patient treatment. This corresponds to the introduction of two-dimensional (2D) dosimeters which include DAVID (PTW-Frieburg, Germany), AIMS (developed by Islam et al [6]), and COMPASS transmission detector (IBA Dosimetry, Germany). Major concerns for using these devices include: influence on the photon beam characteristics, effect on patient surface dose, contamination of the beam with secondary electrons, and effect of large pixel sizes on measured IMRT and VMATfluence. Studies investigating the effects of these devices on photon beam characteristics and patient surface dose have been performed [6-8]. Note that reference 8 is included as appendix A of this thesis, since the author is one of the contributors to the publication. The main objective of this thesis is to investigate the TRD

designed for *in vivo* patient treatment quality assurance. In this thesis, the effect of contaminant electrons due to the TRD and the effect of size of the individual single detectors on measured complex fluences during patient treatment are addressed in chapters 3 and 4 of this thesis. In chapter 5, a general research tool was developed that that performs Monte Carlo simulations for VMATtreatments allowing simultaneous tracking of dose deposition in both the patient CT data set and an arbitrary planar detector system. The tool is capable of simulating dose to an entrance or an exit detector and was validated using both the TRD and an EPID.

Chapter 3 presented a comprehensive study of contaminant electrons originating from the TRD in a clinical photon beam, published in *Physics in Medicine and Biology*. Monte Carlo simulation was used to study the influence of the TRD on photon beam characteristics, surface dose and dose in the build-up region, and on contaminant electron model parameters in two commercial dose calculation algorithms (i.e. Eclipse AAA and Pinnacle^3), as required prior to clinical implementation. Contaminant electron fluence, energy spectra, and angular distributions at different source to surface distances (SSDs) were evaluated for open and non-open (i.e. TRD and block tray) fields. Additional contaminant electrons were observed when using TRD compared to the open field. The device absorbs most of the incident contaminant electrons generated in the linac but then itself becomes the major source of contaminant electrons incident on the patient. These electrons were less energetic and have larger angular distributions compared to contaminant electrons in an open field at shorter SSDs. Without the TRD in the beam path, the air (i.e. within the linac head and between the linac head and the phantom

surface) was observed to be the major source of contaminant electrons. This study demonstrated that the contribution of contaminant electrons to surface dose and dose in the build-up region for a standard block tray and the TRD device increases with increasing field size. In addition, it was found that using the TRD significantly impacted on the contamination electron model parameters of the two commercial dose calculation algorithms. This study showed that the TRD may be used for *in vivo* dosimetry but the contaminant electron model parameters in the treatment planning system need to be modified as described in chapter 3 of this thesis for accurate dose calculation when using the device.

Chapter 4 investigated the spatial resolution of the TRD and its effect on measured IMRT fields, published in *Medical Physics*. The spatial resolution of a multi-element detector system is limited by two main factors, the size of and distance between the individual detector elements in the system. A large detector element will result in poor resolution and a large spacing between detector elements may result in missed information. As discussed in chapter 2 of this thesis, IMRT fluence is characterized by sharp dose gradients between normal structures and target volumes to achieve dose conformity. Therefore, for accurate dose verification of IMRT fluence, the spatial resolution of detector systems to be utilized needs to be investigated. Using a narrow slit collimator formed by two machined lead blocks to define a 0.25x10 mm^2 slit, the line spread function (LSF) of a single ion chamber in the TRD was measured. The LSF measurement was validated with Monte Carlo simulation using BEAMnrc and DOSXYZnrc Monte Carlo codes. The measured modulation transfer function (MTF) for

the detector system was determined and compared to calculated MTFs obtained via both Monte Carlo and analytical methods. To demonstrate that the detector can be used to verify dose during treatment, two clinical head-and-neck IMRT fields were measured using the device and were used to validate the LSF measurement. The validation approach used in this study involves the convolution of the detector response function (DRF), derived from the measured LSF of the detector (as described in chapter 4), with the IMRT fields calculated using BEAMnrc. The results were then compared with entrance dose measured by the detector. The limiting resolution for a single chamber in the TRD was estimated as 0.25 lp/mm from the first zero crossing. This result showed that the TRD is capable of reproducing the dose distributions of complex IMRT fields accurately (i.e. within acceptable tolerance) but might be subjected to aliasing artifacts if fluence complexity increased further. Therefore, future designs of the TRD should pack the ion chambers more closely together. These results have been communicated to the manufacturer and they are currently developing a new prototype version of the detector based in part on this feedback.

Chapter 5 introduced a new general research tool, which uses EGSnrc Monte Carlo package (i.e. BEAMnrc and DOSXYZnrc codes) to simulate VMAT treatment plans and permits simultaneous tracking of dose deposition in both the patient CT data set and a planar detector system. The tool has been developed to model any type of planar detector system, positioned as either an entrance or exit detector, and provides the simulated dose for the individual control-points of VMAT delivery. Planar dose measurement (via an entrance or exit detector) of the individual control-points of VMAT delivery will provide

additional information with which to detect any observed treatment verification errors. The Monte Carlo technique can be used as a tool for validating the accuracy of the planar dose measurements and for verifying phantom or patient dose calculated by the TPS. The Monte Carlo tool keeps the gantry and the planar detector at a fixed geometry while isolating and rotating the phantom/patient scoring geometry as a function of gantry angle, simultaneously tracking dose deposited in both phantom/patient and planar detector volumes. For this work, the TRD and electronic portal imaging device (EPID) were modeled as planar detectors, using geometry and material composition provided by their manufacturers. After the simulations of individual control points of a treatment plan, the tool adds the calculated dose for all the control points to obtain the 3D phantom/patient dose and then compares the result to TPS calculated dose. Also, the 2D planar dose for the individual control-points in VMAT plans deposited in the sensitive layer of the TRD and EPID were obtained and compared to measured doses. The tool was validated for three clinical treatment plans in controlled phantom situations. The results presented in this chapter show that the Monte Carlo dose calculation for both phantom/patient and planar detector are accurate. In general, the validation indicates that the research tool is suitable for accurately calculating both patient/phantom doses and planar doses for VMAT dose delivery.

In conclusion, this thesis presents three primary investigations (contained in chapters three, four, and five) which have helped to significantly improve our understanding of a novel *in vivo* entrance detector developed for patent quality assurance.

6.2 Future work

In this thesis, techniques that use the EGSnrc Monte Carlo package have been successfully implemented for investigating the effect of contaminant electrons due to the TRD on radiation photon beam and for investigating the spatial resolution of the device for verification of IMRT and VMAT fields. A new prototype transmission detector is currently being developed by IBA Dosimetry and will be delivered to CancerCare Manitoba (CCMB) as part of a research agreement with the manufacturer. The new model of the device has 1513 ion chambers with 3.2 mm diameter. To improve the spatial resolution of the new prototype of the device, as recommended in Chapter 4 of this thesis, the ion chambers are more closely packed in the central region defined by 10 x 10 cm^2 area with center-to center distance of 5mm (reduced from 6.5 mm). With a different dimension and new arrangement of the ion chambers, the work in Chapter 3 and 4 of this thesis will need to be repeated.

The general research tool that performs Monte Carlo simulation of the individual control points of complex delivery techniques and allows scoring dose in both phantom and planar detector in a single simulation was successfully validated against measured dose via two planar detectors (i.e. TRD and EPID). Future research work could include additional validation of the tool with the new TRD prototype. Further validation of the tool with newer flattening-filter-free (FFF) linear accelerators (such as the TrueBeam system from Varian Medical Systems), would be useful.

The general research tool consists of multiple codes (functions and scripts) written in the MATLAB programming language and uses the EGSnrc Monte Carlo package for simulation of radiation transport. As described in chapter 5 of this thesis, the tool has three main steps. In the first step, the tool obtains treatment plan parameters such as MU index, gantry angles, MLC positions e.t.c. from DICOM RT then uses this information to create simulation input and phantom files for all control points in VMAT treatment plans. After the individual simulation, the tool performs a post-simulation analysis of the patient/phantom dose and planar dose for all control points. The tool would benefit from a full automation of all the processes, which would include interfacing the MATLAB codes with the EGSnrc package to provide an automated pre-simulation procedure, submission of simulation jobs and post-simulation analysis with little or no manual involvement.

6.3 Bibliography

1. *World Health Organization*. Cancer Mortality and Morbidity.
2. *Procedures in external radiation therapy dosimetry with electron and photon beams with maximum energies between 1 and 50 MeV. Recommendations by the Nordic Association of Clinical Physics (NACP).* Acta Radiol Oncol, 1980. **19**(1): p. 55-79.
3. *Radiotherapy: Hidden dangers. In: 2006 Annual Report of the Chief Medical Officer* 2007, Department of Health: London.
4. ICRU, *Determination of absorbed dose in a patient irradiated by beams of X or gamma rays in radiotherapy procedures*. ICRU Report 24. 1976, Bethesda, Maryland.
5. Kutcher, G.J., et al., *Comprehensive QA for radiation oncology: Report of AAPM Radiation Therapy Committee Task Group 40.* Med Phys, 1994. **21**(4): p. 581-618.
6. Islam, M.K., et al., *An integral quality monitoring system for real-time verification of intensity modulated radiation therapy.* Med Phys, 2009. **36**(12): p. 5420-8.
7. Poppe, B., et al., *Clinical performance of a transmission detector array for the permanent supervision of IMRT deliveries.* Radiother Oncol, 2010. **95**(2): p. 158-65.
8. Venkataraman, S., et al., *The influence of a novel transmission detector on 6 MV x-ray beam characteristics.* Phys Med Biol, 2009. **54**(10): p. 3173-83.

9. Walters, B., I. Kawrakow, and D. Rogers, *DOSXYZnrc users manual.* NRC Report PIRS, 2005. **794**.

10. Mathworks, L., *Matlab the language of numerical computing*. 2006, Mathworks.

APPENDIX A: THE INFLUENCE OF A NOVEL TRANSMISSION DETECTOR ON 6 MV X-RAY BEAM CHARACTERISTICS

This appendix is adapted from a manuscript entitled "The influence of a novel transmission detector on 6 MV x-ray beam characteristics" by Sankar Venkataraman, Kyle Malkoske, Martin Jensen, Keith Nakonechny, **Ganiyu Asuni**, and Boyd McCurdy published in Physics in Medicine and Biology 54(2009) 3173-83. This work investigates the influence of the transmission detector on a 6MV photon beam characteristics. This author's contribution to this paper was performing the Monte Carlo validation of dose measurements in the build up region.

A.1. Introduction

Two-dimensional dosimeter arrays are used in modern radiotherapy to measure the complex dose distributions produced by dynamic fields, such as dynamic wedges or intensity-modulated radiation therapy (IMRT). These 2D arrays provide an efficient means of measuring the dose at multiple locations in the field. Several arrays are available that use ion chambers [1-4], diode detectors [5, 6], electronic portal imaging device [7] or active matrix flat-panel dosimeter [8, 9]. A new 2D ionization chamber array manufactured by IBA Dosimetry (Germany) is under evaluation at our center. The device is positioned in the upper wedge slot of the linear accelerator, providing the capability to perform real-time dose measurements during treatment delivery.

Since it is a new transmission device, its use for in-field measurements with a patient present necessitates a detailed study of its influence on the beam characteristics. Skin dose especially can be one of the limiting factors in treatment plans with high target doses and is a focus in this work, together with general transmission and patient dosimetry effects. Similar studies in the past have been completed for beam modifiers such as wedges, multi-leaf collimators (MLCs) and block trays [10-14]. In this paper, we present the transmission characteristics of this chamber array as well as its influence on the dose in the build-up region and beyond.

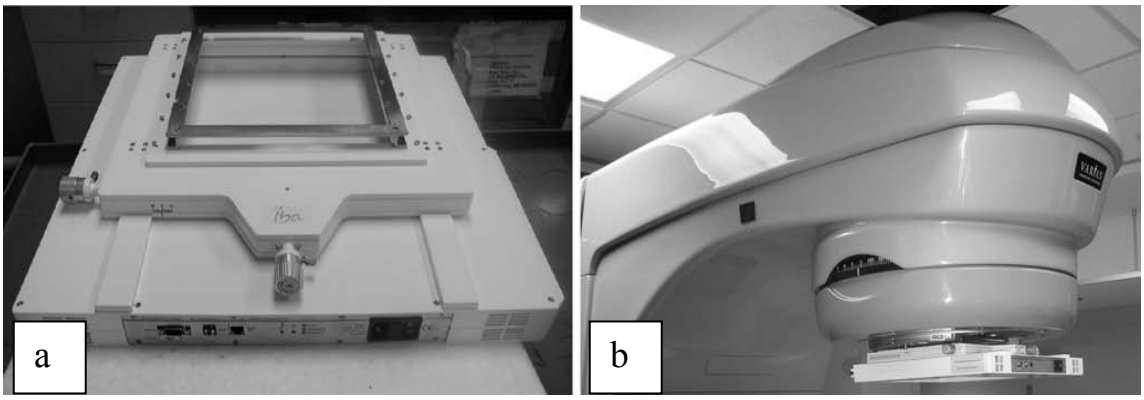


Figure A-1: (a) COMPASS detector (b) COMPASS mounted on the gantry of a linear accelerator

A.2. Methods and materials

Description of a COMPASS detector

COMPASS is a pixel-segmented ionization chamber. This dosimetry device is a

2D array of 1600 air-vented plane parallel chambers with an active area of 40 x 40 cm^2 projected at the isocenter and shown in figure A-1. The external dimensions of this transmission device are 52 cm (W), 49 cm (L) and 11 cm (H) and weighs 15 kg. Each chamber is 3.8 mm in diameter and 2 mm in height. The chambers are spaced 6.5 mm apart, which projects to 1 cm at the isocenter. In our measurements, the detector assembly was mounted directly onto the gantry in the wedge slot of a Varian Clinac 2100iX linear accelerator with a source-to-detector distance of 65 cm.

All measurements were performed at 6 MV on a Varian 2100iX linear accelerator (linac) with Millennium 120-leaf MLC. The measurements covered a range of field sizes, source– surface distances (SSDs) and depths as necessary. In this work, 'COMPASS field' refers to a radiation field with the COMPASS detector in the beam path.

A.2.1. Measurement techniques

Extrapolation chambers have long been recognized as capable of accurate measurements of dose at the surface and in the build-up region of megavoltage x-ray beams [15, 16]. However, extrapolation chambers are not commonly available in therapy centers due to their specialized application. Mellenberg (1990) compared the response of the Markus Model 329 parallel plate chamber (PTW-Freiburg, Germany) to that of an extrapolation chamber in the buildup region of megavoltage x-ray beams and generated tables of correction factors to account for the 'over-response' of the Markus chamber. The over-response is due to the small guard ring width in the Markus Model 329 design

[17]. In this study, we used the Markus Model 329 chamber for measurements in the build-up region and corrected the raw measurement by a simple subtraction of the over-response factor based on Mellenberg's data.

To validate our Markus chamber measurements, we compared the doses at the surface and in the build-up region to those measured with GafChromic EBT film (International Specialty Products, Wayne, NJ) and calculated with Monte Carlo simulation. Recently, several authors have shown radiochromic film to also be a suitable dosimeter for dose measurements in the buildup region [18, 19]. The film measurements were performed in solid water slabs for a 10 x 10 cm^2 field size and a source-to-surface distance (SSD) of 90 cm with the film positioned perpendicular to the beam direction. The films were scanned in a Vidar Dosimetry Advantage Pro^{TM} digitizer (Vidar Systems Corporation, Herndon, VA). Film analysis was performed with RIT 113 software (Radiological Imaging Technology, Colorado Springs, CO) using a calibration curve based on 24 exposures ranging from 11 to 613 cGy to convert the optical density to dose [20]. Evaluation of the surface dose requires the extrapolation of film measurements since the effective measurement point is located at mid-thickness of the film, resulting in a minimum measurement depth of about 153 μm for EBT films.

For the Monte Carlo simulation, the treatment head of the linear accelerator was modeled using BEAMnrc/EGSnrc software [21] based on the specifications provided by the manufacturer. The beam model was validated by comparison of Monte Carlo simulation to measurements using a water phantom at 90 cm SSD and 20 x 20 cm^2 field

size. The percentage depth doses and profiles at d_{max}, 5 cm, 10 cm and 20 cm were compared and the differences were within 2%. Phase-space files were generated for field sizes of 20 x 20 cm^2. The generated phase-space files contain position, energy, charge and weight of scored particles and were used as input in the DOSXYZnrc/EGSnrc for calculating dose in a water phantom. Electron kinetic energy transport cut-off and photon transport cut-off energy used for the beam simulation and dose calculations are 0.700 MeV and 0.010 MeV, respectively. An exact boundary crossing algorithm was run for accurate electron transport and the PRESTA-II electron step algorithm was used. The photon forcing and Rayleigh scattering options were turned off, but Russian roulette and uniform bremsstrahlung splitting, a variance reduction technique producing 40 bremsstrahlung photons for each bremsstrahlung event, were turned on to increase the efficiency of treatment head simulation. All the Monte Carlo simulations were performed with a maximum uncertainty of ±0.3% by increasing the number of particles.

To check the reproducibility of the Markus chamber and GafChromic film, the surface dose was independently measured five times under the same geometric conditions. The measurement uncertainty associated with the chamber and film were ±0.4% and ±0.7% (1 s.d.), respectively. The short-term reproducibility check with a reference chamber was performed to ascertain the linac output uncertainty and was found to be ±0.05%.

A.2.2. The influence of the transmission detector on the surface dose and in the build-up region

Surface doses, *S*, are reported as a percentage of the dose at a depth of 1.4 cm, which corresponds to the average depth of maximum dose (d_{max}) in an open field for the range of field sizes and SSDs studied. The surface dose on the central axis was measured for field sizes ranging from 3 x 3 to 20 x 20 cm^2 and SSDs from 70 to 90 cm for open and COMPASS fields. Central axis percentage depth doses (PDDs) from the surface to a depth of 1.6 cm were measured using the Markus chamber in solid water, at a resolution of 2 mm. Measurements were performed in both open and COMPASS fields to evaluate how the presence of the detector affected the dose at shallow depths. A range of SSDs (70–90 cm) and field sizes (3 x 3cm^2 to 20 x 20 cm^2) were evaluated.

To evaluate the influence of the transmission detector on the surface dose across the field, off-axis measurements (profiles) were performed using the Markus chamber in solid water for open and COMPASS fields. The chamber was positioned with the effective point of measurement at the surface and the profiles were acquired for a 20 x 20 cm^2 field at SSDs of 70, 80 and 90 cm. The profiles were measured to a distance of 20 cm from the central axis for all SSDs, at a resolution of 2–20 mm depending on the dose gradient.

It has been shown from previous studies that IMRT itself does not contribute to increased surface doses [22, 23]. In addition, the authors have observed that the increased

surface dose due to beam obliquity in IMRT was similar to the increase in the dose with the use of open beams. Therefore, our detailed evaluations in this paper have been limited to open fields. However, a picket fence pattern representing the IMRT plan was irradiated with and without the COMPASS detector in field and the analysis was performed. The results showed that the increase in surface dose for picket fence with COMPASS compared to open field was similar to the increase observed for normal jaw settings. In other words, the COMPASS detector itself does not contribute to any increase in surface dose for IMRT plans.

A.2.3. The influence of the transmission detector on dose beyond dmax

Since the transmission detector is intended to be positioned in the beam during patient treatments, it is important to assess how the device influences the dose beyond d_{max} so that modifications to the treatment planning data may be incorporated if necessary (i.e. possibly adjusting the beam model). The following relative dose parameters were compared with and without the transmission detector in the path of the beam: central axis PDD; profiles at 1.4 and 10 cm depths; transmission factor at 10 cm. PDDs and profiles were measured in a water phantom using a Markus chamber and diode (PFD Scanditronix), respectively, for field sizes ranging from 3 x 3cm^2 to 20 x 20 cm^2 and SSDs of 80 and 90 cm (the geometry of the water phantom did not allow measurements at a 70 cm SSD in COMPASS fields). The transmission factors were measured in solid water at 10 cm depth using a Markus chamber for field sizes ranging from 3 x 3 to 20 x 20 cm^2 and SSDs from 70 to 90 cm.

A.2.4. Comparison of the transmission detector to a block tray

A comparison of the transmission detector to a standard acrylic block tray was made to assess its influence on the beam relative to a common treatment accessory. A subset of the above measurements was repeated at a single SSD of 90 cm with the 5.8 mm thick acrylic Varian block tray in the accessory mount. These measurements included PDDs from the surface to a depth of 20 cm, and transmission factor measurements.

A.3. Results

A.3.1. The influence of the transmission detector on the surface dose and dose within the buildup region

There was good agreement between the doses measured with the Markus chamber, EBT film and Monte Carlo simulation in the build-up region (figure A-2). The surface doses, S (90 cm, 10 x 10 cm^2), were 14.8% and 14.6% for the Markus chamber and EBT film, respectively, while the Monte Carlo calculated surface dose (at 50 μm) was 16.3%.

The surface dose and dose in the buildup region increased when the transmission detector was in the beam as shown in figure A-3 and table A-1 The error bars for all the measurements are within the size of data points and hence not explicitly shown. For

moderately narrow beam geometric conditions (smaller fields, larger SSDs), the increase in surface dose was small. However, as the field size increased or in particular, the SSD was reduced, the increase in surface dose became quite large. For example, at an SSD of 70 cm the surface dose with the transmission detector in the beam was more than double that of the open field. For the 20 x 20 cm^2 field at a 70 cm SSD, the depth of d_{max} was shifted from 14 mm to 5 mm when the transmission detector was in the beam.

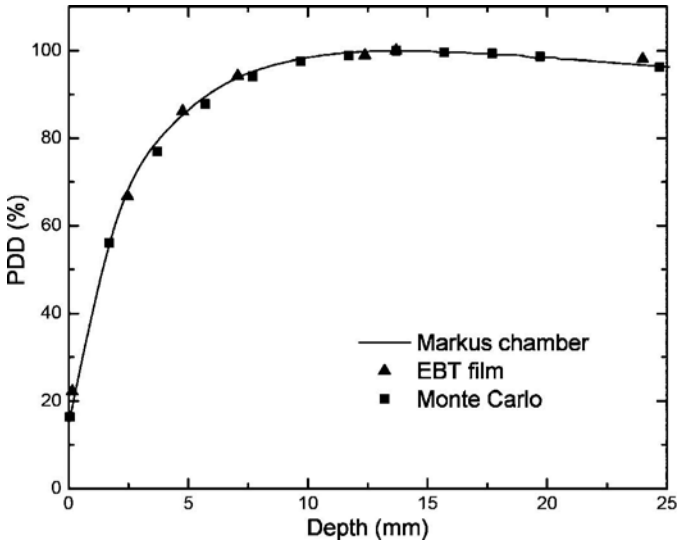


Figure A-2: Comparison of the dose in the buildup region measured in solid water with a Markus chamber and EBT film, and the calculated dose from Monte Carlo simulation for an open field of 10 × 10 cm^2 and an SSD of 90 cm

Table A-1: The difference between the surface doses in open and COMPASS field.

Differences are expressed as a percentage of the dose at 1.4 cm depth, i.e. *S* (COMPASS field) − *S* (open field). The measured surface doses in the open fields (percentage of the dose at 1.4 cm depth) are shown in parentheses for reference

S(COMPASS) − *S*(open) (%)

Field size (cm2)	SSD = 90 cm	SSD = 80 cm	SSD = 70 cm
3 × 3	0.7 (6.4)	1.4 (6.5)	8.7 (7.1)
5 × 5	1.3 (8.6)	3.0 (8.7)	18.2 (9.7)
10 × 10	3.0 (14.8)	8.1 (15.3)	36.3 (17.4)
20 × 20	8.1 (26.8)	18.2 (28.5)	44.8 (32.6)

In broader terms, the surface dose profiles showed expected behavior within the field, i.e. increased doses for COMPASS compared to open fields. Results of surface dose profiles for SSDs 70 cm and 90 cm are presented in figure A-4. Open-field central axis dose was used for normalization for both open and COMPASS fields. Off-axis doses for the COMPASS field were much larger and less uniform than the open field for an SSD of 70 cm. As the SSD increased from 70 cm to 90 cm, the dose differences decreased and the COMPASS profiles showed more uniformity. Figure A-4(c) illustrates the surface dose difference as a percentage of the open field central axis dose for all three SSDs. It was interesting to note that COMPASS doses beyond the field edge for an SSD of 70 cm were lower than that of the open field while they were consistently higher than that of open fields for SSDs 80 cm and 90 cm. For example, at 6 cm beyond the field

edge, the COMPASS dose for an SSD of 70 cm was 3% lower than that of the open field whereas it was 7.3% higher than that of the open field for both SSDs 80 cm and 90 cm, respectively.

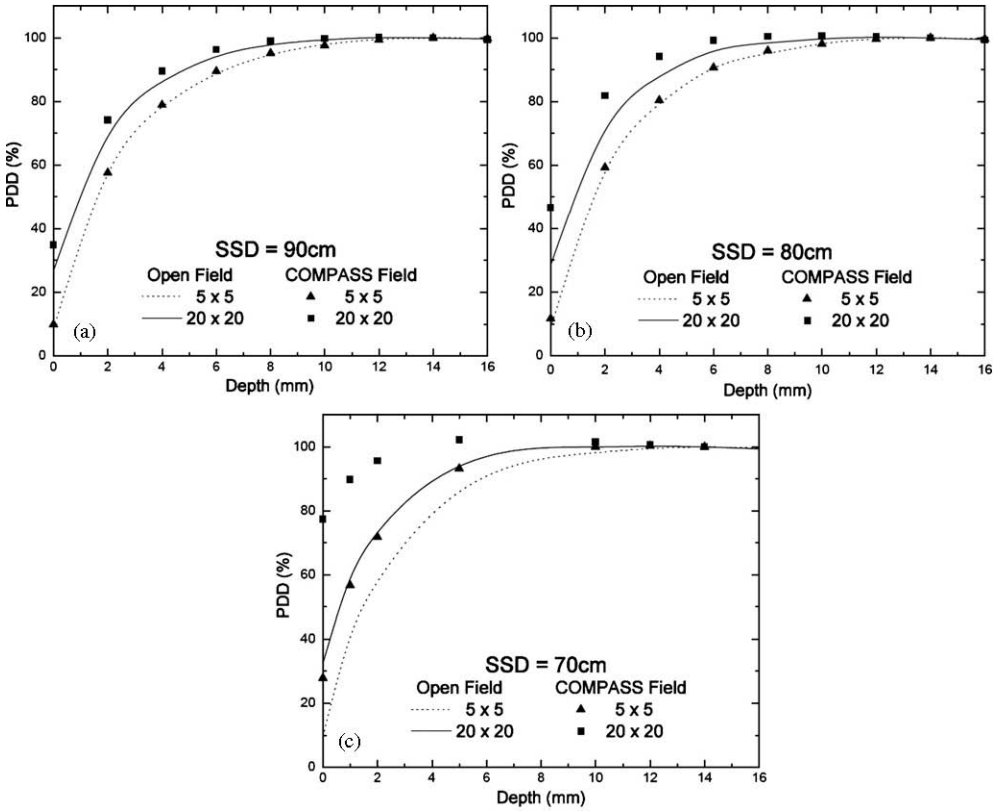


Figure A-3: The dose in the buildup region at SSDs of (a) 90 cm, (b) 80 cm and (c) 70 cm. The lines indicate measured doses in the open field, whereas the symbols represent doses measured with the transmission detector in the beam. All the measurements were performed with the Markus chamber in solid water.

A.3.2. The influence of the transmission detector on dose beyond d_{max}

Beyond d_{max}, the differences between the PDDs and profiles were negligible, as shown in figures A-5 and A-6. The maximum difference between open and COMPASS fields was less than 0.3% of dose at d_{max}. The transmission factors were very consistent throughout the range of field sizes, off-axis distances and SSDs investigated (the same range as in table A-1). The mean value was 0.967 with a standard deviation of 0.002.

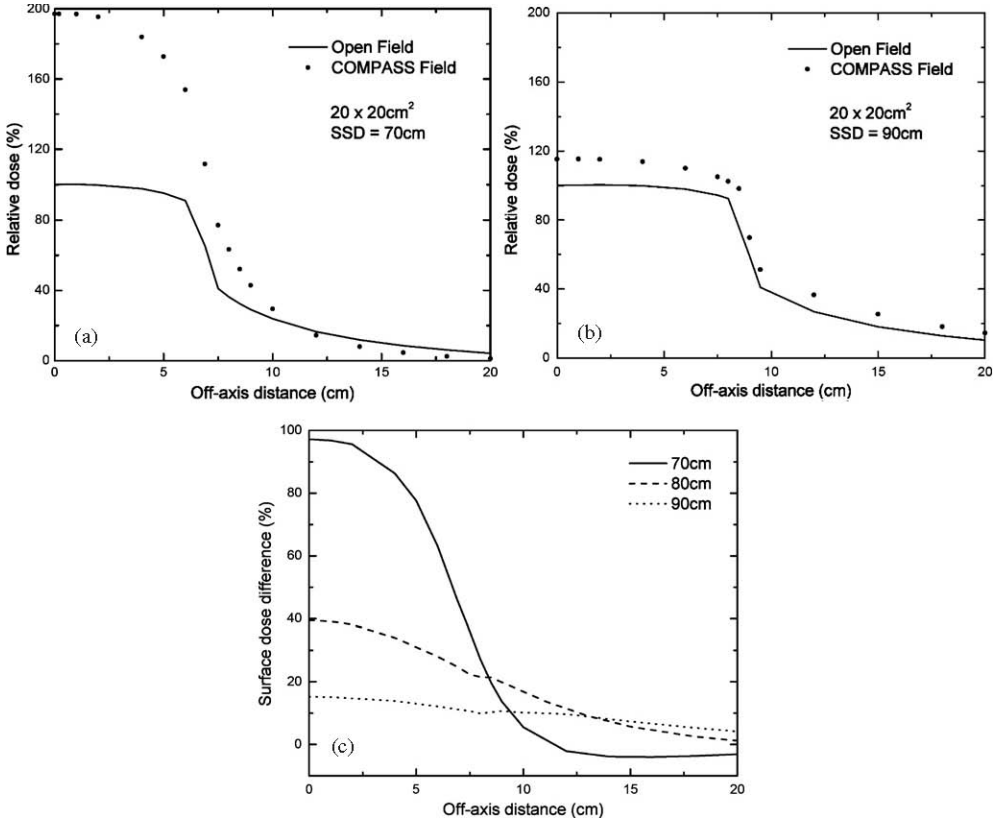


Figure A-4: The surface dose profile at SSDs of (a) 70 cm and (b) 90 cm for 20 × 20 cm^2 field size. The lines indicate measured doses in the open field, whereas the symbols represent doses measured with the transmission detector in the beam. Measurements were taken with the Markus chamber in solid water; (c) shows the difference between the surface dose profile with and without the transmission

detector in the beam expressed as a percentage of the open field dose on the central axis. Data for the three SSDs show the reduction in surface dose in-field and increase in surface dose out-of-field as the SSD increases, due to the lateral divergence of the electrons produced in the transmission detector

A.3.3. Comparison of the transmission detector to a block tray

When comparing the transmission detector to a standard acrylic block tray, it was found that the two accessories had a similar effect on the beam properties. The transmission factor for the COMPASS detector was found to be 0.4% lower than that for the block tray. The surface doses with the transmission detector were consistently lower than those with the block tray. The maximum difference in surface dose was at the 20 x 20 cm^2 field, where the transmission detector had a surface dose 3.8% lower than that of the block tray. Figure A-5 demonstrates the similarity in PDD between the two accessories.

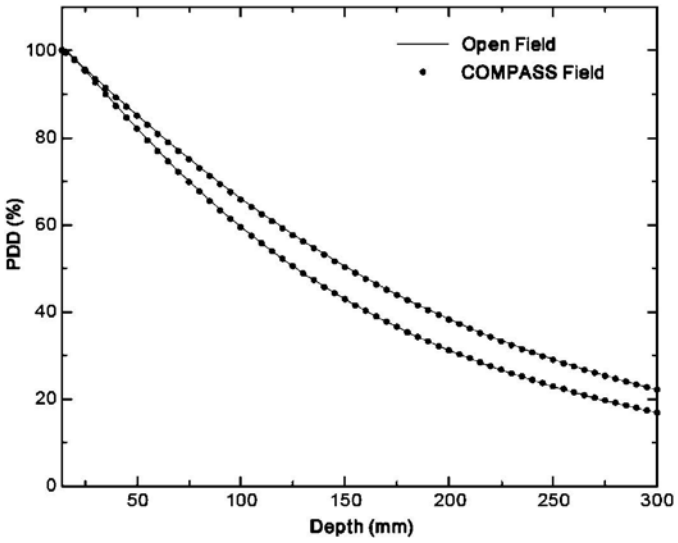


Figure A-5: PDDs beyond d_{max} for 5 × 5cm^2 (lower curve) and 20 × 20 cm^2 fields at an SSD of 80 cm. The first measurement point is at d_{max} in the figure. Measurements were taken with the Markus chamber in the water phantom. Similar results were obtained at 70 cm and 90 cm SSDs.

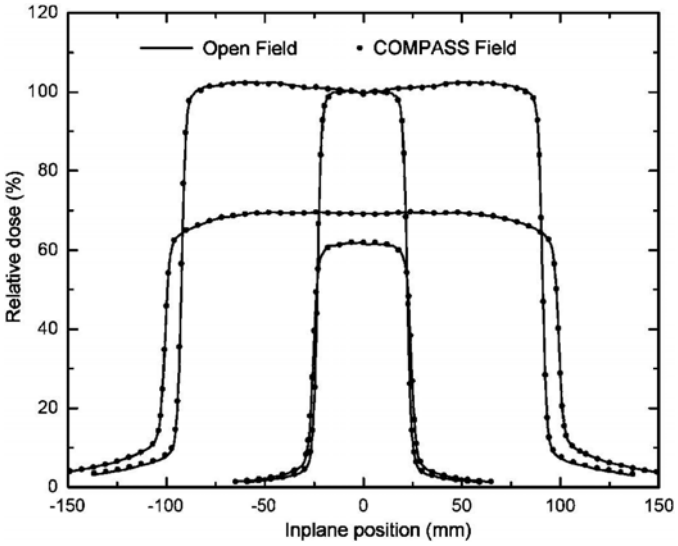


Figure A-6: Profiles at 1.4 cm and 10 cm depths for 5 × 5cm^2 and 20 × 20 cm^2 fields at an SSD of 90 cm. Measurements were taken with the diode in the water phantom.

A.4. Discussions

The dose in the buildup region of a 6 MV beam was affected by the presence of the COMPASS transmission detector. Butson *et al* (1996) studied in detail the causes for the surface dose and dose in the build-up region and concluded that the surface dose at 6 MV is mostly due to electron contamination. At a short distance between the transmission detector and the phantom surface (SSD 70 cm), the surface dose on the central axis

measured in this study increased by approximately a factor of 2 for all field sizes as compared to that measured at a 90 cm SSD. As the SSD increased, the elevation of surface dose with the detector inserted was less pronounced. For the largest field size investigated at a 90 cm SSD, the surface dose with the detector inserted was 34.9% versus 26.8% in the open field. With the transmission detector serving as an extra source of electron contamination to the beam, this behavior was expected. In fact, the increases in surface dose with the detector in beam (table A-1) exhibited roughly an inverse-square law dependence with respect to a position 65 cm from the x-ray target for the 3 x 3 and 5 x 5cm^2 field sizes. This corresponded to approximately the center of the transmission detector. At a given SSD, the influence of the transmission detector on surface dose was more pronounced as the field size increased.

In general, the observed increase in surface dose with COMPASS can be attributed to increased electron contamination with the detector acting as an extended electron source. At an SSD of 70 cm, there was less than 5 cm air gap between the exit surface of the transmission detector and the phantom surface. Due to the short distance between the site of electron liberation in the transmission detector and the surface of the phantom, there was little angular spread and hence the majority of the added contaminant electrons intercepted the phantom within the geometric boundary of the photon field. As the SSD increased, the change in surface doses with off-axis position diminished and became more evenly distributed between the in-and out-of-field regions at the phantom surface (figure A-4(c)).

The PDDs in the buildup region of open and COMPASS fields gradually merged with depth as the influence of photon phantom scatter started to dominate the electron contamination component of dose. The PDD and profiles beyond the average d_{max} depth of 14 mm were not significantly affected by the presence of the transmission detector. Based on our observations, no changes to the treatment planning system's open field model would be required for treatment delivery with COMPASS in the beam, other than a scaling of the monitor units by the detector transmission factor.

The transmission factor showed very little variation with field size and SSD (standard deviation <0.2%). It is suggested that a single value of transmission factor (in our case 0.967) be applied to all field geometries for the linac and energy studied here. When this information is factored into the treatment plans, the actual dose distribution can be obtained with the detector in the beam path. Comparison to measurements with an acrylic block tray has shown that the insertion of the transmission detector has a similar effect on the radiation beam as a standard block tray.

A.5. Conclusions

This work describes the influence of a new transmission detector consisting of a 2D ionization chamber array on 6 MV photon beam dosimetry. An increase in the surface dose was observed with the detector in the beam path for large field sizes and small SSDs. Due to the increased surface dose for shorter SSDs (e.g. 70 cm), it may be prudent to either remove the detector for obese patient treatments or to modify the treatment plan

to redistribute the doses to minimize the local surface dose. Our measurements show that the differences between open and COMPASS fields were found to be insignificant beyond d_{max}. A single transmission factor of 0.967 could be entered in the beam data of the treatment planning system, as this factor was nearly constant over a large range of SSDs and field sizes. The similarity in the effect of the block tray and transmission detector on the beam parameters is reassuring. With the exception of the transmission factor, the only influence of the transmission detector on a 6 MV beam is an increase in dose in the buildup region. Beyond d_{max}, the beam parameters of COMPASS and open fields were in good agreement.

A.6. Bibliography

1. Amerio, S., et al., *Dosimetric characterization of a large area pixel-segmented ionization chamber.* Med Phys, 2004. **31**: p. 414.
2. Herzen, J., et al., *Dosimetric evaluation of a 2D pixel ionization chamber for implementation in clinical routine.* Phys Med Biol, 2007. **52**(4): p. 1197-208.
3. Spezi, E., et al., *Characterization of a 2D ion chamber array for the verification*

of radiotherapy treatments. Phys Med Biol, 2005. **50**(14): p. 3361.

4. Stasi, M., et al., *D-IMRT verification with a 2D pixel ionization chamber: dosimetric and clinical results in head and neck cancer.* Phys Med Biol, 2005. **50**(19): p. 4681-94.
5. Jursinic, P.A. and B.E. Nelms, *A 2-D diode array and analysis software for verification of intensity modulated radiation therapy delivery.* Med Phys, 2003. **30**(5): p. 870-9.
6. Letourneau, D., et al., *Evaluation of a 2D diode array for IMRT quality assurance.* Radiother Oncol, 2004. **70**(2): p. 199-206.
7. Greer, P.B., et al., *Experimental investigation of the response of an amorphous silicon EPID to intensity modulated radiotherapy beams.* Med Phys, 2007. **34**: p. 4389.
8. El-Mohri, Y., et al., *Relative dosimetry using active matrix flat-panel imager (AMFPI) technology.* Med Phys, 1999. **26**: p. 1530.
9. Moran, J.M., et al., *An active matrix flat panel dosimeter (AMFPD) for in-phantom dosimetric measurements.* Med Phys, 2005. **32**: p. 466.
10. Butson, M.J., K. Peter, and P.E. Metcalfe, *Measurement of off-axis and peripheral skin dose using radiochromic film.* Phys Med Biol, 1999. **43**(9): p. 2647.
11. Kim, S., et al., *Photon beam skin dose analyses for different clinical setups.* Med Phys, 1998. **25**(6): p. 860-6.
12. Lamb, A. and S. Blake, *Investigation and modelling of the surface dose from linear accelerator produced 6 and 10 MV photon beams.* Phys Med Biol, 1999. **43**(5): p. 1133.

13. Li, Z. and E.E. Klein, *Surface and peripheral doses of dynamic and physical wedges.* International Journal of Radiation Oncology Biology Physics, 1997. **37**: p. 921-926.

14. McParland, B.J., *The effects of a universal wedge and beam obliquity upon the central axis dose buildup for 6-MV x rays.* Medical Physics, 1991. **18**: p. 740.

15. Manson, D.J., et al., *Measurements of surface dose using build-up curves obtained with an extrapolation chamber.* Radiology, 1975. **115**(2): p. 473-474.

16. Yu, P.K.N., T. Cheung, and M. Butson, *Variations in skin dose using 6MV or 18MV x-ray beams.* Australasian Physical & Engineering Science in Medicine, 2003. **26**(2): p. 78-80.

17. Gerbi, B.J. and F.M. Khan, *Measurement of dose in the buildup region using fixed-separation plane-parallel ionization chambers.* Med. Phys, 1990. **17**(1): p. 17-26.

18. Devic, S., et al., *Accurate skin dose measurements using radiochromic film in clinical applications.* Med Phys, 2006. **33**: p. 1116.

19. Quach, K.Y., et al., *Measurement of radiotherapy x-ray skin dose on a chest wall phantom.* Med Phys, 2000. **27**(7): p. 1676-80.

20. Childress, N.L., L. Dong, and I.I. Rosen, *Rapid radiographic film calibration for IMRT verification using automated MLC fields.* Med Phys, 2002. **29**: p. 2384.

21. Rogers, D.W., et al., *BEAM: a Monte Carlo code to simulate radiotherapy treatment units.* Med Phys, 1995. **22**(5): p. 503-24.

22. Dogan, N. and G.P. Glasgow, *Surface and build-up region dosimetry for obliquely incident intensity modulated radiotherapy 6 MV x rays.* Med Phys,

2003. **30**(12): p. 3091-6.

23. Price, S., et al., *Comparison of skin dose between conventional radiotherapy and IMRT.* Australasian Physical & Engineering Science in Medicine, 2006. **29**(3): p. 272-277.

APPENDIX B: INSTRUCTIONS ON HOW TO USE THE MONTE CARLO RESEARCH TOOL FOR EVALUATING VMAT TREATMENT DELIVERY INCLUDING PLANAR DETECTORS

This appendix summarizes the steps needed to prepare and execute a simulation with the Monte Carlo research tool. As described in chapter six, the steps are broken into three main stages.

B.1. Pre-simulation stage

The following tasks are performed in the pre-simulation stage:

1. Create and export verification plan data via DICOM consisting of RT plan, RT structures, and CT datasets from the TPS.
2. Obtain treatment plan parameters such as MU index, gantry angles, MLC positions, jaw positions, collimator angle, and couch angle using MATLAB code *eCERRImportDCM4CHE.m*
3. Create BEAMnrc input files for both arcs in the VMAT verification plan. Phase-space files are scored at 45 cm SSD behind the jaws in the next stage (Simulation stage).
4. Use MATLAB code *getmlc.m* to create MLC sequence files for each control point (CP) in the verification plan (e.g. for a plan with 177 CPs per arc, the code will create 354 MLC sequence files).
5. Use MATLAB code *wrt_vcuinput.m* to create VCU input files required for MLC simulation in the *particleDMLC* code combined as a shared library in DOSXYZnrc.
6. Use MATLAB codes *CT2linacIsocenter.m* and *InserKCouch_ctpad.m* developed to read CT datasets from the TPS to obtain the CT center and planning isocenter positions from the planning data. Then the correct isocenter location in a new 'corrected' CT dataset is ensured by shifting the CT center point relative to the planning isocenter in all dimensions (x, y, and z). These codes also remove the CT couch in the original CT dataset and replace it with the treatment couch.

7. For the correctly positioned CT dataset, with treatment couch, use *ctcreate* code contained in the EGSnrc package to obtain a Monte Carlo phantom file with extension .egsphant. The phantom file contains the physical density and material numbers as derived from the CT data sets, as required.
8. Combine the phantom/patient .egsphant files with either an entrance detector or an exit detector, to obtain a single Monte Carlo phantom file using MATLAB code *cmbegsphant.m*. The MC phantom file contains the phantom/patient volume, and the detector (either entrance or exit) geometry, as well as an air gap representing the space between the phantom/patient and detector.
9. After obtaining the Monte Carlo phantom file, use MATLAB code *readegsphant.m* to rotate only the phantom volume for the individual control point simulations, using the gantry angle information obtained from the RT plan. The phantom volume is rotated in the opposite direction to the gantry rotation indicated in the treatment plan, and unique phantom files will be created for each control point.
10. Use MATLAB code *wrt_dosxyznrc.m* to create DOSXYZnrc input files (ISOURCE 20 is used for VMAT simulation at fixed (zero) gantry angle) for each control point in the VMAT verification plan.

B.2. Simulation stage

In this stage the following tasks are performed

1. Run shell script *rapidarc_BEAMnrc.sh* to submit BEAMnrc simulation jobs on multi-core computer system. After simulation, it combines all resulting phase-

space files into a single phase-space file using *addphsp* user code in EGSnrc Monte Carlo package.

2. Run shell script *rapidarc_DOSXYZnrc.sh* to submit DOSXYZnrc simulation jobs on multi-core computer system. After simulation of each control point, the .3ddose and .egslog file are stored in a separate folder while the remaining unwanted files are deleted to free space in dosxyznrc folder.

B.3. Post Simulation stage

After the DOSXYZnrc simulation of all the control points in the verification plan, then use MATLAB code *phantEpidDose.m* to perform the following tasks:

1. Convert the Monte Carlo dose to absolute dose using the formalism described by Popescu *et al* (2005)
2. Separate MC absolute dose to phantom dose and 2D planar dose, then rotate and combine phantom dose for all CP to obtain single 3D phantom dose
3. Obtain 2D planar dose scored in sensitive player of planar detector for all control points.
4. Perform comparison of 3D phantom dose, MC vs. TPS and 2D planar dose :MC vs. measured

APPENDIX C: GLOSSARY OF TERMS[‡]

3D-CRT – three-dimensional conformal radiation therapy; It is a form of external beam radiation therapy that uses computer software to create a three-dimensional (3-D) image of the tumour so that multiple radiation beams from different directions can be shaped to closely match the projected outline of the treatment volume (i.e. 'conformal').

arc-IMRT (or VMAT) – The most complex form of IMRT (intensity modulated

radiation therapy) currently commercially available. It involves delivery of radiation to the patient while the gantry rotates about the patient, with simultaneous motion of the MLC's and collimator, and variation of dose rate. The delivery method is known commercially as RapidArc^{TM} (Varian Medical Systems, Palo Alto, CA) or VMAT (Elekta AB, Stockholm, Sweden).

CAX – Central axis; In the coordinate system of the linear accelerator, the line joining the linac focal spot and the isocentre. It can also be described as the axis about which the collimator of the linear accelerator rotates and is considered the nominal direction of the beam of radiation.

Commissioning – Commissioning refers to the validation of any radiation therapy devices or equipment for use in the clinic (e.g. ionization chambers, CT simulators, linac accelerator) ahead of it's clinical use. For example, a newly installed medical linear accelerator would require a full determination of dosimetric quantities and mechanical properties before clinical operations commence. An example of the quantities measured is the output of the linac through a series of dose profiles in water and percentage depth dose (PDD), for a range of field sizes. The entire range of activities employed by a linac need to be tested, including the calibration of the physical quantities of a linac to the fluence model of a TPS.

Cross-plane direction – As an observer faces towards the gantry of the linac, the cross-plane direction is the left/right direction, parallel to the floor. It is coincident with the x-axis as defined by the IEC treatment beam coordinate system.

CT – Computed Tomography; A diagnostic imaging technique which uses projections of low-energy x-rays delivered to a patient over a 360^0 rotation to reconstruct a three-

dimensional x-ray image of patient called CT dataset.

Dark-field – Two dimensional EPID image collected prior to irradiation to correct for background electronic signals (i.e. not related to irradiation) of the individual EPID pixels.

DICOM – Digital Imaging and Communications in Medicine; It is a standard for handling, storing, printing, and transmitting information in medical imaging. It includes a file format definition and a network communications protocol. DICOM files can be exchanged between two entities that are capable of receiving image and patient data in DICOM format.

DTA – Distance-to-Agreement; A term used in analysis for comparing two presumed similar datasets, to describe the physical proximity (in units of length) that is acceptable between two corresponding data points.

DVH – Dose Volume Histogram; It is used in radiation therapy to summarize 3D dose distributions in a graphical 2D format. The "volume" referred to in DVH analysis can be a target of radiation treatment, a healthy organ nearby a target, or any arbitrary structure. DVHs can be visualized in two ways: differential DVHs or cumulative DVHs.

Dynamic delivery – An IMRT delivery method that achieves fluence modulation by the continuous motion of the MLC leaves in one direction across the field, with each leaf possibly exhibiting a different velocity trajectory. The beam is delivered during MLC movement.

ECUT – Electron cut off energy; This is the kinetic energy below which electron histories are terminated (i.e. all remaining kinetic energy is deposited locally and the particle is removed from the simulation) in the EGS/BEAM Monte Carlo radiation

transport software.

EPID – Electronic Portal Imaging Devices; A megavoltage x-ray imaging device that can be used for patient set-up verification with the megavoltage beam prior to a radiation therapy treatment. The current clinical standard for EPID design is the two-dimensional aSi photodiode array.

Flood-field – A two-dimensional image collected during irradiation of the entire EPID area. The image corrects the acquired raw image by creating a uniform field by removing dosimetric information inherent in the beam.

Fractionation – The daily dose of radiation based on the total dose divided into a particular number of daily treatments. For example, a standard treatment regimen delivers 1.8 to 2.0 Gy to the tumour per fraction, once a day, over a period of 5 to 7 weeks.

FWHM – Full Width at Half Maximum; the width of a distribution or function at 50% of the maximum value.

Gantry – The part of the linac which houses the treatment head where the x-ray radiation is created and collimated into a therapeutic beam for radiation treatment. The gantry rotates 360^0 around the patient.

Gantry angle – Angular direction of the linac gantry's central axis, relative to a reference angle. Typically at 0^0 the linac's beam central axis is pointed at the ground (perpendicular to the floor surface), while at 180^0 the gantry is below the patient with the beam pointing upwards.

IEC coordinate system – Coordinate system defined by the IEC (International Electrotechnical Commission). It defines the spatial coordinate system of the linear accelerator, which has the positive 'x' to the right and parallel to the ground for a

standing observer facing the gantry of the treatment beam, the positive 'y' is from the isocenter towards the gantry and the positive z directed upwards from the isocenter towards the ceiling.

IMRT – Intensity Modulated Radiation Therapy; A radiation therapy technique that uses a multi-leaf collimation to deliver complex fluence patterns to the patient at multiple static gantry angles.

In-plane direction – This is the direction along the electron gun/target axis of the linac. It is coincident with the y-axis as defined by the IEC treatment beam coordinate system.

Isocenter – This is the point in space through which the central beam of radiation passes and it is usually set at 100 cm from radiation source.

Linac – (Medical) Linear accelerator; A machine delivering high-energy radiation to patients for the purposes of disease treatment.

MLC – multi-leaf collimator; developed to collimate the treatment beam to the shape of the tumour in the patient. It consists of a large number of collimating leaves (typically 80 to 160), each under individual motorized computer control. The leaves are made of tungsten alloy and individual leaf widths are typically 0.5 to 1.0 cm, as projected to isocenter.

MTF – Modulation Transfer Function; A measure of spatial resolution of imaging systems. It depends on pixel size and spacing between pixels.

MU – Monitor Unit; A measure of beam on-time for a linac. The linac is calibrated in the TPS to a dose value that is measured with an ion chamber using a standard calibration field delivered to a water tank, at a specific depth for a known amount of monitor units. For example, a typical calibration value is 1cGy of dose delivered by a 10x10 cm^2 field

on the central axis at 10 cm depth in water for 1 MU of beam on-time i.e. 1cGy/MU is the calibration used in the TPS and calibrates beam on-time to dose calculated using the TPS.

MV – megavoltage; used to describe the nominal energy of a polyenergetic photon radiation beam, with the energy based on the maximum energy particle contained in the beam. The term describes the effective electric potential that would need to be created in order to generate a beam of photons with that maximum energy (i.e. analogous to the use of kV or kilovoltage to describe the energy of diagnostic photon beams, since they are generated via accelerating electrons through an applied voltage). For example, a 6 MV photon beam consists of photons that range in energy from 0 to 6 MeV. Monoenergetic beams (for example, beams of electrons) are described in units of MeV.

Non-transit image (or open-field image) – Image acquired with neither a patient nor a phantom in the beam. The radiation is delivered directly to the EPID.

OAR – Organ At Risk; Normal tissue as typically delineated on CT scans in treatment planning software. These organs are to be spared from radiation damage as much as possible.

PCUT – Photon cut off energy; This is the kinetic energy below which photon histories are terminated (i.e. all remaining kinetic energy is deposited locally and the particle is removed from the simulation), in the EGS/BEAM Monte Carlo radiation transport software.

PDD – Percentage Depth Dose; The measurement of dose in a material (usually water) as a function of depth.

Phantom – Attenuating material placed into the beam that is dosimetrically equivalent

(or close) to a patient. A phantom can be a simple tank of water or a water-equivalent plastic slab, or made of multiple materials to create an anthropomorphic object that more closely mimics a patient.

PSM – Pixel Sensitivity Matrix; A two-dimensional array that corrects for the individual pixel response of the aSi EPID. The PSM is required when reintroducing the flood-field into a measured EPID image as the flood-field inherently corrects the pixel sensitivity, but also removes important dosimetric information when correcting the image to create a uniform field.

SDD – Source-to-Detector Distance.

SNR – Signal-to-Noise Ratio; A measure of the noise (i.e. spurious, unwanted signal) in an imaging system.

SSD – Source-to-Surface Distance.

Step-and-shoot delivery – IMRT delivery method that achieves fluence modulation by dividing the delivery into multiple small fields, or "segments". The beam is delivered only when the MLC is stationary. Each static gantry angle employs many segments (typically 7 – 20).

TERMA – Total energy released per unit mass in an irradiated volume, specifically by primary x-ray interactions.

TPS – Treatment Planning System; Software employed to customize the radiation treatment for a patient, allowing the creation of a three-dimensional map of the intended radiation dose for the individual patient. TPS software requires CT datasets of the patient and beam information specific to the linac the patient is to be treated on.

TRD – A novel transmission detector developed by IBA Dosimetry (Swarzenbruck,

Germany) for entrance dose verification of complex treatment delivery.

γ-evaluation – Analysis method to quantitatively compare two datasets. If the value of the γ-evaluation is less than one, then the datasets agree within the specified criteria of dose difference and distance to agreement.

χ-evaluation – This is a method to analyze two datasets. If the value of the χ-evaluation is less than one, then the datasets agree within the specified criteria of dose difference and distance to agreement. The χ-evaluation is similar to the popular γ-evaluation, but is more computationally efficient.

‡ Definition of some glossary terms were adapted from PhD thesis submitted to Faculty of Graduate Studies, University of Manitoba titled "Dosimetric verification of radiation therapy including intensity modulated treatments, using an amorphous-silicon electronic portal imaging device" 2012 by Chytyk-Praznik, K